Granularity and Disordered Superconductors

Shachaf Poran

Department of Physics

Ph.D. Thesis

Submitted to the Senate of Bar-Ilan University

Ramat-Gan, Israel February 2015

This work was carried out under the supervision of
Professor Aviad Frydman
Department of Physics, Bar-Ilan University

Acknowledgements

Mieux vaut ne pas pouvoir avoir dit merci mais vraiment le penser que le dire sans aucune émotion.

It is worth better not to say thank you but to really think it, than to say it without any emotion.

עדיף לא לומר תודה אך לחשוב אותה באמת, מאשר לומר תודה ללא כל רגש.

It is somewhat difficult for me not to feel a lump in my throat, at the end of this period. A wonderful chapter is coming to an end, and these pages are the only place where I can express my appreciation for a good many people who helped me along the way.

First and foremost, I could not have come half of the way to where I am now without the complete trust my advisor, Prof. Aviad Frydman, has given in me. Every idea I suggested along the way was given deep thought in his feverish mind, and the worthy ones received his full support. Even at times of hardship and in times of doubt - he kept believing, and for this I thank him profoundly.

My French host Olivier Bourgeois, with his French hospitality and his French confiture de myrtilles, has accommodated me in his laboratory for more than a year. During this time I was given an opportunity to grow and develop not only as a researcher but also as a man of the world, and to soak myself in another culture with its language and its customs. This once-in-a-lifetime experience does not go unappreciated.

The academic staff in Bar-Ilan University was more than willing to help me in guidance and long conversation about scientific and technical issues alike. Efrat Shimshoni, Richard Berkovits, Amos Sharoni, Dimitri Gutman, Beena Kalisky, and Boris Shapiro are but a few of those that come to mind.

A lot of graduate students shared the lab with me, including Ora Simcha Bitton, Noa Kurzweil, Natanel Ossi, Tal Havdala, Ariel Eisenbach and lately Oriya Eisenberg. To them a new lab manager, Irina Volotsenko, was added. Each of them was, or still is, essential in the scientific and social fabrics that span our laboratory. I thank you all for the great time we spent together.

Above these students a person stands out, with whom I shared a room for nearly six years: from the beginning of our Master's degree up until recent months, when we both finish our Ph.D studies. Daniel Sherman - you are a dear friend of mine. Thank you.

I cannot end this section without thanking the people in my life that are outside of the academic world. My friends and family, though the chances of you reading these lines are slim, I thank you for the patience you showed in listening to the stories that you may or may not understand about superconductors and other cool stuff I made up.

Last but not least - Sivan. Love of my life, the girl I married and then ignored during the writing of this dissertation. There is a part of you in this work ♡

Contents

List of Figures

List of Abbreviations

a-InO ..... Amorphous Indium Oxide

AFM ..... Atomic Force Microscope

BCS ..... Bardeen-Cooper-Schrieffer

BKT ..... Berezinskii-Kosterlitz-Thouless

CC ..... Calorimetry Cell

dFF ..... Force derivative Feature

EFM ..... Electrostatic Force Microscope

GL ..... Ginzburg-Landau

MFM ..... Magnetic Force Microscope

NbN ..... Niobium nitride

QC ..... Quench Condensation

QCR ..... Quantum Critical Regime

QPT ..... Quantum Phase Transition

RIE ..... Reactive Ion Etching

SiN ..... Silicon nitride

SIT ..... Superconductor-Insulator Transition

STM ..... Scanning Tunnelling Microscope

Abstract

"How does disorder affect superconductivity" is a question that persists in the field of solid state physics, as it has for several decades. Despite a rich world of theoretical and experimental endeavours, a clear answer has yet been given.

It has been well-established by a variety of experiments that when one induces a high enough level of disorder on an otherwise superconducting matrix, global superconductivity ceases to exist and the disordered system forms an electrical insulator. This crossover from a superconductor to the localized insulator is a manifestation of a quantum phase transition, a transition at zero temperature between two quantum ground states that is driven by a non-thermodynamic parameter. By being a quantum phase transition, the so-called "superconductor-insulator transition" (SIT) attracts much attention in the world of condensed matter physics.

This dissertation aims to investigate the world of disordered superconductors and the superconductor-to-insulator transition in several unique manners. We hope to add crucial information to contribute to the development of a complete theory of disordered superconductors.

The most widely used method of characterizing disordered superconductors is by transport measurements. This method is sensitive to inhomogeneities and the specifics of percolation paths through the sample, and in fact might ignore the greater part of the system, if the percolation path is dilute. In order to overcome this limitation, two of the three measurements are strictly not sensitive to percolation.

The first experiment we perform overcomes this problem by measuring a global quantity. i.e. the heat capacity. We perform this thermodynamic measurement on granular Pb and Sn films, both model systems that undergo the SIT. From our results we are able to determine that even in very disordered systems, for which transport measurements are impossible as the film resistance exceeds several GΩs, superconductivity persists. This is the first time

such a rigorous confirmation for superconductivity in an insulator is seen, and settles the debate about whether the localized charges in the insulator side of the in the SIT in granular systems are Cooper pairs or electrons.

In addition, the jump of the heat capacitance, used to quantify the second-order phase transition between the normal and the superconducting states, shows a peak at the critical thickness. We show that it is due to the vicinity to the quantum phase transition. We calculate the critical exponent of the heat capacitance as a function of distance from the quantum phase transition.

This experiment is a first-of-its-kind, with a set-up that enables the measurement of samples with extremely small mass. The heat capacity has never before been measured for a system as it undergoes the SIT, and we believe that our results will be crucial in the understanding of the SIT and other QPTs.

Another experiment we report in this work is local magnetic measurements, performed with a magnetic force microscope. We perform this experiment on amorphous indium oxide films. These films are fabricated so that they are structurally homogeneous. However, several indications were given in the past that the superconducting state is broken into separate islands, in what was named an "emergent granularity". By using the local magnetic measurement we are able to measure remnants of superconductivity at temperatures up to twice the critical temperature that is determined by transport measurements. This evidence joins other experiments performed in the past that suggested the existence of superconductivity above T_c.

Our results support the hypothesis that signs of superconductivity above T_c emerge from inhomogeneity and from the fact that some parts of the film are superconducting, despite the absence of global superconductivity.

We are also able to probe the emergent granular structure. We show that the penetration depth of the superconductor state is extremely large in most of the sample, meaning that superconductivity is weak. However in specific regions of the film, the penetration depth is much smaller. This clearly demonstrates the inhomogeneity of superconductivity in the film.

Furthermore, our results point at an interplay between electron localization and the emergent granularity. We are able to show that superconducting

grains emerge where electronic localization sites form due to Anderson localization.

The third reported experiment is based on the proximity effect, performed as a new variant for transport measurements. We add a thin metallic layer on top of a disordered a-InO film. We find that the metallic layer acts to either increase the critical temperature of superconducting a-InO film by means of the proximity effect, or to decrease it via the inverse proximity effect depending on the sample disorder. Higher disorder films always show an increase in T_c, and films with lower disorder always show a decrease in T_c.

We also show two insulating cases. Insulators with a high level of disorder are indifferent to the addition of the proximity layer. Insulating samples that are close to the transition are pushed into the superconducting side.

We are able to qualitatively explain all these phenomena by considering the proximity effect and the inverse proximity effect, and the way they both affect superconductivity of the electrically granular superconductor.

While disordered superconductors have been studied in solid state physics research for several decades, they are still far from being thoroughly understood. We believe that this work will help take one step closer to a complete theory that describes the mechanisms at work, and to a deeper understanding of superconductivity at large.

Chapter 1

Introduction

1.1 Superconductivity

Superconductivity is one of the twentieth century's greatest serendipities. Its discovery in 1911 was a by-product of the international race to liquefy all elemental gases, a race which was won by a Dutch scientist, Heike Kamerlingh Onnes [1]. By having access to the lowest temperatures available in his time with helium liquefaction technology, he was also able to test the behaviour of metals in this regime, and therefore was the first to measure the zero-resistance aspect of superconducting mercury [2]. Ever since, superconductivity was in the utmost front of condensed matter research.

Three notable milestones in the history of superconductivity are the Ginzburg-Landau (GL) theory (1950) [3] which is a phenomenologically sound theory that explains the superconducting phase transition and several aspects in its existence, such as the characteristic lengths and the difference between Type-I and Type-II superconductors; the BCS theory (1957) [4] which envelopes the microscopic explanation of superconductivity with the formation of bosonic electron pairs, the appearance of a gap around the Fermi level and more; and the discovery of high-temperature superconductors (1986)[5], which broke the limit set by the BCS that implied that no superconductivity can exist above $30K$.

1.1.1 Vortices

In the framework of the GL theory the superconducting order parameter which appears below a critical temperature T_c is described as a complex number:

$$\Psi(r) = \Delta(r)e^{i\phi(r)} \tag{1.1}$$

Δ being the superconducting gap and ϕ being a phase. When fed into the GL Hamiltonian [3], two characteristic lengths arise. One is the London penetration depth λ_L, named after the London brothers who introduced it before GL. This length sets the exponential decay of fields when penetrating the superconductor. The second is the coherence length ξ_{LG} which sets a spatial scale for perturbations of the order parameter.

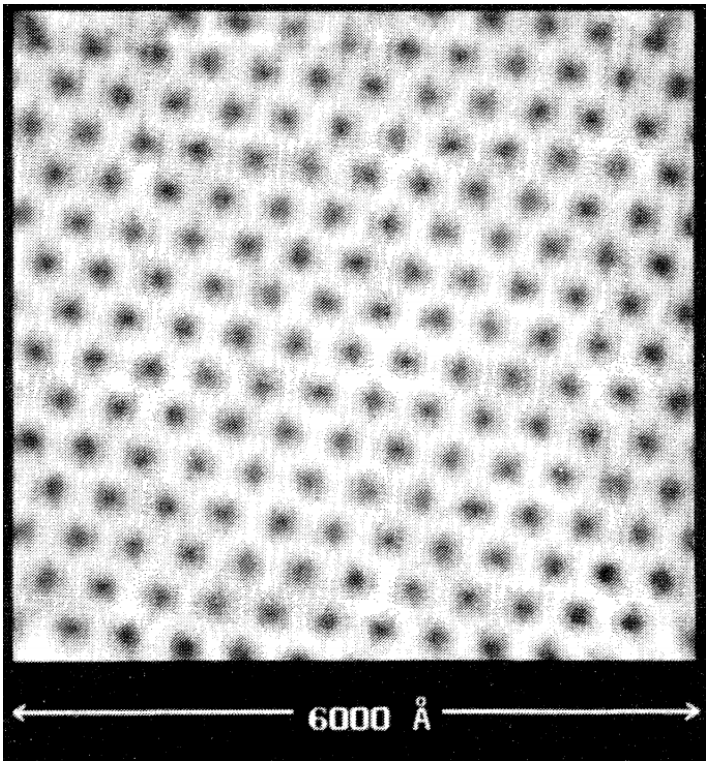

Figure 1.1: An Abrikosov lattice. The white background is a superconducting niobium selenide films. The black dots are the places where superconductivity is suppressed and a flux line is allowed to pass. Taken from [6].

The response of superconductors to magnetic field depends on the ratio between the two scale lengths, reduced to the GL parameter $\kappa = \frac{\lambda_L}{\xi_{LG}}$. An energy is associated with the interface between the normal and superconducting regions. When $\kappa < \frac{1}{\sqrt{2}}$ this energy is positive and the superconducting regions arrange themselves in a way to minimize the interface' area. Such superconductors are known as Type-I. In the ideal case of an infinite clean superconductor the Meissner effect is observed, where no magnetic flux penetrates the entire superconducting sample up to a critical magnetic field H_c, and no superconductivity is observed above this field. If $\kappa > \frac{1}{\sqrt{2}}$ the interface energy is negative and the system allows magnetic flux to penetrate the superconducting regions, and arranges itself in a way to maximize this surface area. These superconductors are classified as Type-II. This arrangement was calculated by Abrikosov [7] who showed that the magnetic flux penetrates the superconductor in singular regions arranged in a triangular lattice. Figure 1.1 shows an example for an Abrikosov lattice.

These regions are created when a magnetic flux penetrates the film and thus destroys superconductivity in a cylinder of diameter ξ_{LG}. Around this cylinder, superconducting currents prevent the magnetic flux from further destroying the superconductor. As a consequence, when circumventing around any such point the phase of the order parameter changes. Due to the continuity of the order parameter this change must be of $2\pi n$ with $n \in \mathbb{Z}$. The magnetic flux penetrating the normal-state cylinder, along with its tangential currents, is thus quantized:

$$\Phi_0 = \frac{h}{2e} \tag{1.2}$$

and is known as a "vortex", due to the tangential currents around it.

In a thin superconductor with thickness $t < \lambda_L$ the penetration depth becomes effectively larger by the relation $\lambda_{L_{eff}} = \frac{2\lambda^2}{d}$. Therefore a thin enough superconducting film is always Type-II.

1.1.2 The XY model

The GL theory inspires a model for the study of superconductors with an emphasis on the importance of the superconducting phase. The model con-

sists of an array of planar rotors, each site i characterized by its phase ϕ_i. The simplest ground state of a superconductor with no additional perturbations and disregarding quantum fluctuations will occur when its phase is the same for all sites. This is because currents induced by gradients in the phase contribute a kinetic energy to the system. Therefore in this discrete model the energy is

$$E_{XY} = -J \sum_{\langle i,j \rangle} cos\left(\phi_i - \phi_j\right) \tag{1.3}$$

where $\langle i, j \rangle$ stands for nearest neighbours summation and J is the interaction energy.

The continuous analogue of Equation 1.3 is introduced by making the phase a function of space

$$E_{XY} = \frac{J}{2} \int sd^2r \left(\nabla\phi(r)\right)^2 . \tag{1.4}$$

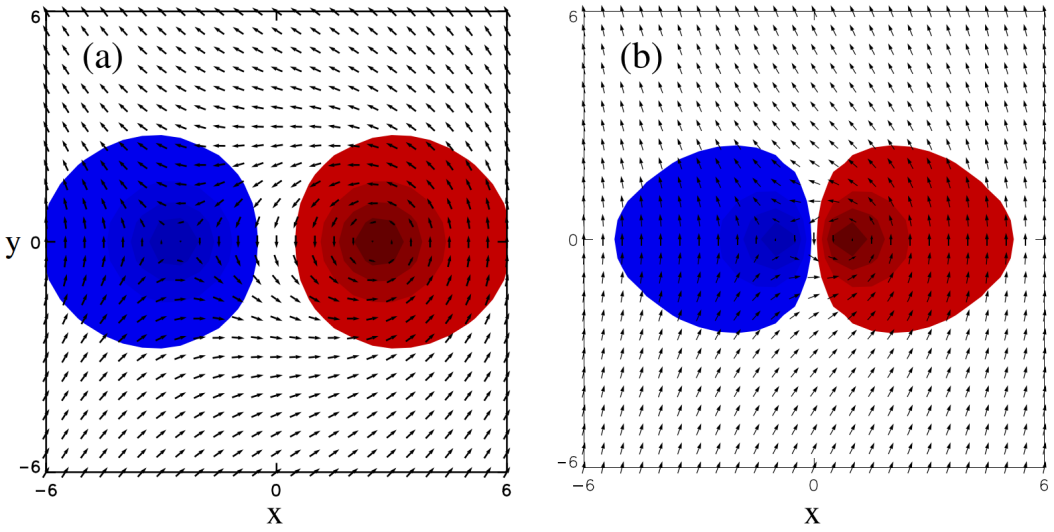

Figure 1.2: **left** A pair of vortex and antivortex as seen in the XY model The red one has vorticity of +1 and the blue −1. **right** the same pair brought closer together. Taken from [8].

A vortex in this model is a point with non-zero total phase change when circumventing it. Once again, continuity considerations means that the

change in phase when traversing a closed loop must be an integer multiple of 2π. A visual example for such vortices with 2π and an anti-vortex with -2π phase around them is shown in Figure 1.2.

The distortion of the ground state phase due to these vortices decays with distance r from the vortex as $|\nabla\phi| \propto \frac{1}{r}$, which leads to a logarithmic divergence with system size L of the energetic cost of adding a vortex to the system

$$E_{vortex} \propto Jln\left(\frac{L}{a}\right) \tag{1.5}$$

with a the vortex core radius.

However, if a vortex-antivortex pair is added to the system, this distortion decays much faster with distance and the energetic cost for the pair is limited by the pair separation R

$$E_{VA} \propto ln\left(\frac{R}{a}\right). \tag{1.6}$$

The XY model is an important model for disordered superconductors where the phase rigidity is reduced, as will be discussed in section 1.3.

1.1.3 The BKT transition

Although a net magnetic flux is required to create a vortex, for two-dimensional superconductors in a temperature region just below T_c pairs of vortices with opposite polarities (vortices and anti-vortices) are constantly created and annihilated due to fluctuations in the superconducting order parameter. The attractive interaction (repulsive between two vortices) between vortices is

$$E_v = E_0 log\left(\frac{L^2}{\xi_{LG}}\right) \tag{1.7}$$

where L^2 is the area of the superconductor, while the entropy of the pair is given by

$$S_v = 2k_B log\left(\frac{L}{\xi_{LG}}\right) \tag{1.8}$$

since there are approximately $\left(\frac{L}{\xi_{LG}}\right)^2$ different places a vortex may reside in the film. The Helmholz free energy is thus

$$F = (E_0 - 2k_B T) log \left(\frac{S}{\xi_{LG}}\right) \tag{1.9}$$

and a phase transition, known as the Berezinskii-Kosterlitz-Thouless (BKT) transition, occurs at $T_{BKT} = \frac{E_0}{2k_B} \leq T_c$. Below this temperature vortex-antivortex pairs are bound, while above it the pairs are not bound. Unbound vortices cause dissipation and destroy the zero-resistance of the superconducting phase.

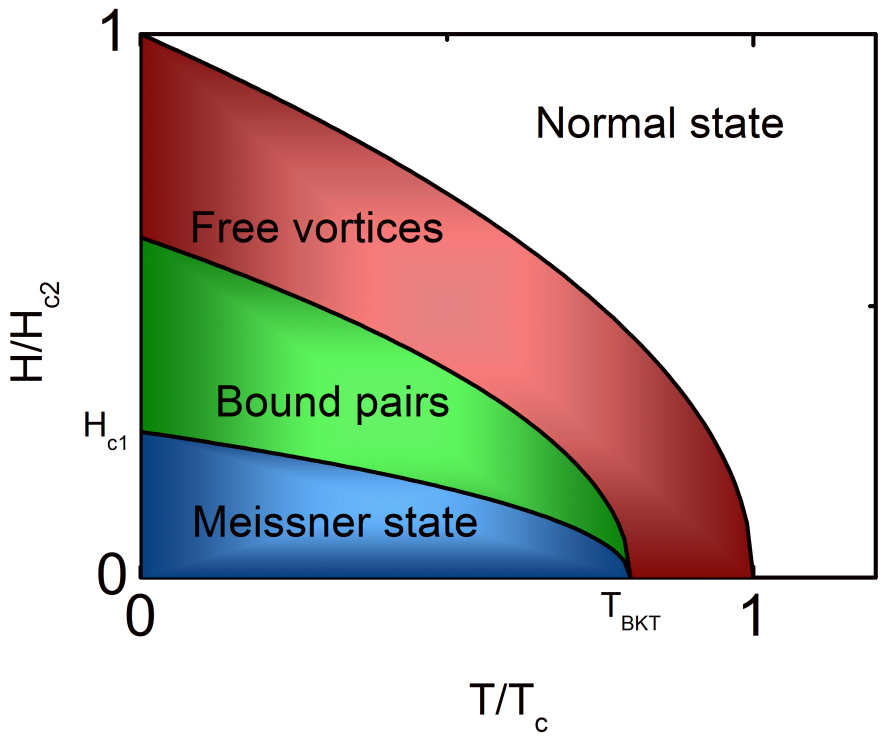

Figure 1.3: Phase diagram of a Type-II superconducting thin film. Adapted from [9].

A phase diagram for a superconducting film including the BKT phases is shown in Figure 1.3. Note that the free vortex state is seen also at $T = 0$.

This state exists as quantum fluctuations continue to contribute to the vortex mobility even in the absence of thermal fluctuations.

1.2 Disorder

Though thoroughly and comprehensively studied, perfectly ordered crystalline systems are the exception rather than the rule in nature. Every crystalline sample has at the least several imperfections in its crystalline structure, be it dislocations, breaks or alien atoms, this disorder is inevitable.

While low degree of disorder was handled in the past with a perturbed Bloch function leading to corrections to the ordered conductivity[10], these calculations eventually do not hold when increasing the disorder.

In 1958 Anderson showed [11] that when sufficiently disordered a conducting system will become insulating due to quantum effects. Destructive interference of propagation paths causes the Bloch function to break down, and leads to localization of the electronic wave functions. The wave function then becomes exponentially confined to small sites with characteristic size ξ, the localization length

$$|\Psi(r)| = \Psi_0 e^{\frac{-|r-r_0|}{\xi}} \tag{1.10}$$

Mott [12] showed that in any disordered systems there is a sharp energy separating localized states from extended states. The localized states reside below a threshold energy, E_c, called the mobility edge. Above this energy all states are extended.

It is possible for an electron to move from one localization site to another by a tunnelling process. If there is no matching energetic state for the electron to occupy in the target site, it may absorb or emit a phonon. This phonon-assisted tunnelling process is known as "hopping". In such a hopping process the probability of an electron to move to the next localization site decays exponentially both with the distance between the two sites, and with the energetic difference between the occupied level in the source site and the free level in the target site, which is effectively reduced by the chance to absorb

or release a phonon:

$$p \propto e^{-\frac{\epsilon_{ij}}{k_B T} - \frac{r_{ij}}{\xi}} \tag{1.11}$$

with ϵ_{ij} the energy difference between the two sites and r_{ij} the distance between them.

Mott asserted an *a-priori* assumption that the density of states is constant in the vicinity of the Fermi energy and showed the hopping resistance follows a stretched Arrhenius law with temperature

$$R\left(T\right) = R_0 e^{\left(\frac{-T_0}{T}\right)^{\nu}} \tag{1.12}$$

with $T_0 \propto \frac{1}{N(E_F)\xi^d}$, $N(E_F)$ is the density of states at the Fermi level.

This form has in fact become a hallmark of conduction in disordered systems, with ν the characteristic exponent. The value of ν depends on the transport mechanism. For Mott hopping this exponent changes according to the dimensionality D of the system as $\nu = \frac{1}{D+1}$, i.e.

$$R\left(T\right) \propto \begin{cases} e^{\left(\frac{-T_0}{T}\right)^{\frac{1}{3}}} & 2D \\ e^{\left(\frac{-T_0}{T}\right)^{\frac{1}{4}}} & 3D \end{cases} \tag{1.13}$$

Efros and Shklovskii [13] showed that when Coulomb interactions are taken into account the density of states near the Fermi level is suppressed. Their argument is as follows. For a system with ground state where all states below the Fermi energy, E_F, are full and all states above it are vacant, the excitation of a single electron from energy E_i below E_F to an energy E_j above it should increase the total energy of the system:

$$\Delta E = E_j - E_i - e_{ij} > 0 \tag{1.14}$$

where e_{ij} is the Coulomb interaction between the excited electron and the hole it left behind. However, if the density of states is constant, there will always be an excitation close enough to E_F where the Coulomb interaction is greater than the excitation energy. This breaks the inequality above, meaning that there is a state of the system with energy lower than the ground state,

which is a contradiction. The density of states is therefore non-constant in this region, and in their paper the authors continue to show that it vanishes altogether at E_F. Near the Fermi energy the density of states is dependent on dimension, and follows

$$N_{2D}(E) \propto |E - E_F| \tag{1.15}$$

$$N_{3D}(E) \propto (E - E_F)^2 . \tag{1.16}$$

Efros and Shklovskii's argument affects Mott's calculation for ν, and changes it to a dimensionality-independent constant $\nu = \frac{1}{2}$. i.e.,

$$R \propto e^{\left(\frac{T_0}{T}\right)^{\frac{1}{2}}}, \tag{1.17}$$

irrespective of the dimension.

In addition, since the density of states vanishes at the Fermi level one must recalculate the nature of T_0. In their model they show that $T_0 \propto \frac{e^2}{\xi}$, proportionate to the Coulomb interaction in a localization site.

1.3 The superconductor-insulator transition

The notions of disorder and localization in solids, have given rise to many questions regarding their effect on superconductors.

Anderson showed [14],in parallel though separately from Abrikosov and Gor'kov[15], that superconductivity should persist in the presence of non-magnetic impurities and weak disorder. However, experiments on quasi-two-dimensional systems showed [16] that for strong enough disorder superconductivity is destroyed and the system becomes insulating.

Nowadays the experimental world of the superconductor-to-insulator transition (SIT) is rich with a vast variety of examples controlled by various tuning parameters. These include film thickness[16], [17], binary material composition [17], magnetic field [18], [19], electric field [20] and more.

All of the measured systems that show the SIT are on the two-dimensional limit. This is due to the fact that no localization is strictly expected in three-

dimensional systems.

Several theories have been raised to explain the microscopic nature of the SIT. In this section we focus on three of them.

1.3.1 The fermionic models

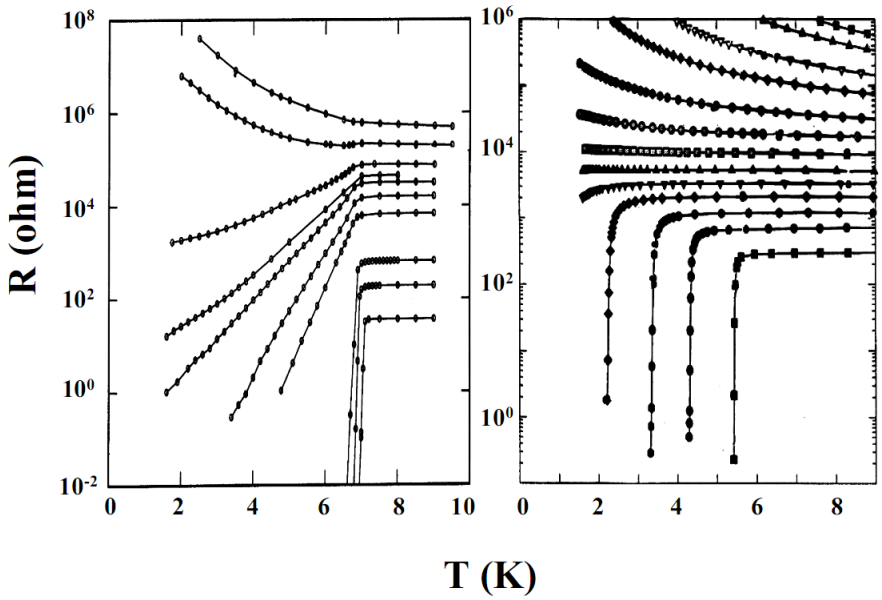

Figure 1.4: $R(T)$ curves taken for thin Pb films of different thickness. The higher the normal-state resistance the higher the disorder and thinner the film. The left panel is of a granular film and the right one is of a uniform-thickness film. Taken from [21].

One theory, first proposed by Maekawa [22], further developed by Takagi *et al.* [23] and later by Finkel'stein [24] is based on the electron-electron interaction. In an ordered material the electrons' Coulomb interaction is screened by a balance between the background's positive charge and the electron negative charge. However, when electron motion is limited to localization sites Coulomb interaction is not screened, and therefore plays a role in restricting the pairing of electrons into Cooper pairs. This causes a decrease in the superconducting gap.

A model system that shows a manifestation of this theory is an ultra-

thin metallic superconductor. In a thin film the effective charge density is decreased. This leads to a weaker screening of the Coulomb interaction. The right panel of Figure 1.4 shows a set of $R(T)$ curves for Pb films with varying thickness. The thickest film, seen at the bottom of the plot, shows a rather sharp transition to the superconducting state at some critical temperature. The following several curves, for thinner films, show a gradually decreasing critical temperature until, for some critical thickness, T_c vanishes and the resistance seems to diverge when approaching zero temperature.

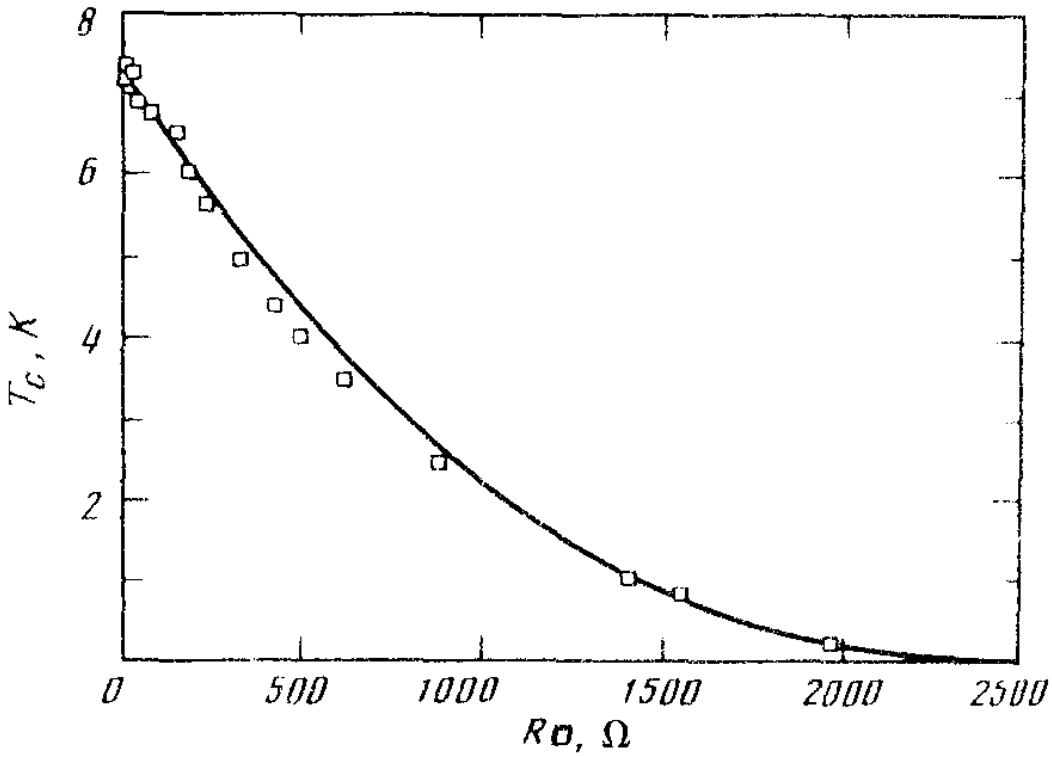

Figure 1.5: Superconducting transition temperature T_c plotted versus sheet resistance $R_\square$ of amorphous MoGe sheets of different compositions and thickness. Taken from [24].

Figure 1.5 shows a summary of a similar experiment, with the normal-state sheet resistance, $R_\square$, of the films on the horizontal axis and the critical

temperature in the vertical axis. A fit to Finkel'stein's expression

$$ln\left(\frac{T_c}{T_{c_0}}\right) = \gamma + \frac{1}{\sqrt{2r}} \ln\left(\frac{\frac{1}{\gamma} + \frac{r}{4} - \sqrt{\frac{r}{2}}}{\frac{1}{\gamma} + \frac{r}{4} + \sqrt{\frac{r}{2}}}\right) \tag{1.18}$$

is shown, which seems to agree with the data. In the expression $\gamma = ln\left(\frac{\hbar}{k_B \tau T_{c_0}}\right)$, $r = R_\square \frac{e^2}{2\pi^2\hbar}$ with τ the scattering rate.

1.3.2 The bosonic model

Another scenario may take place when the disorder is introduced in the form of discontinuity in the superconducting film, or in the form of a highly inhomogeneous matrix. In such films in order to traverse the system Cooper pairs must hop from one grain to another. While such motion is allowed by a Josephson tunneling mechanism, in the case where the grains are extremely small there will also be a considerable charging energy $E_C = \frac{2e^2}{C}$ (C here is the capacitance of one grain) that Cooper pairs must overcome in order to enter. The ratio between the charging and the Josephson energies $p = \frac{E_C}{E_J}$ determines whether the system is superconducting or insulating.

The left panel of Figure 1.4 shows a set of $R(T)$ curves for a discontinuous Pb films that are gradually taken from a highly disordered state to an ordered state. This change of disorder takes the system from being an insulator to being a superconductor, but in a different manner than that seen in the right panel. Intermediate states having long exponential tail are seen between the superconductor and the insulator.

It is possible to explain the granular Pb experiment by means of the bosonic model, with the normal-state resistance being indicative of p. For high p, i.e. the highest normal-state $R_\square$ curves, with the Josephson coupling negligible compared to the charging energy, Cooper pairs are localized on the grains and cannot tunnel from one to the other. In this case the sample is a bosonic insulator.

When gradually lowering p, transport is allowed between grains, and slightly below T_c a decrease of resistance occurs, however this trend reverses with further reducing the temperature and resistance once again diverges

when approaching zero resistance. At an even lower p, a monotonous reduction of resistance with temperature is seen below T_c, characterized by long exponential tails. Eventually, when the Josephson coupling overshadows the charging energy, a sharp transition occurs at the bulk T_c.

Note that throughout the SIT a change in behaviour is seen at the bulk $T_c = 7.2$K, whether it is the superconducting transition in the low-disorder films, the decrease in resistance before the re-entrance in the intermediate disorder films, or a kink before the rise in resistance for high disorder.

The number of electrons in a grain, n_s, and the superconducting phase are quantum conjugates, giving $\Delta n_s \Delta\phi \geq 2e$. Therefore when the small superconducting grains have a highly determinable number of Cooper pairs their phase will fluctuate strongly. This fluctuations give rise to a voltage drop between any two neighbouring grains via the ac Josephson relation:

$$V(t) = \frac{\Phi_0}{2\pi}\frac{\partial\phi}{\partial t}. \tag{1.19}$$

This mechanism contributes to the resistance measured in all stages of the granular SIT.

In the granular system we can therefore define two important critical temperatures. One is the temperature where Cooper pairs are formed T_ρ, and the other is the temperature where the superconducting phase is locked across the sample T_ϕ, which may be equal to T_c (like in a bulk superconductor) or much less, down to zero for the granular insulators. T_c is determined by the minimum of these two temperatures.

A question that arises regarding the granular SIT is at what point do the separate grains become superconducting. Is it indeed possible that the charge in the insulating state is already paired into Cooper pairs?

An indication for superconductivity in the insulator can be already seen in the transport measurements in Figure 1.4, where in the granular case the uppermost curve changes its behaviour abruptly at the critical temperature of the bulk material $T_c = 7.2$ Kelvin. Another example can be seen in Figure 1.6, which shows the $I(V)$ curve of a tunnelling junction with a metal on one side and an insulating granular Pb film on the other. The superconducting

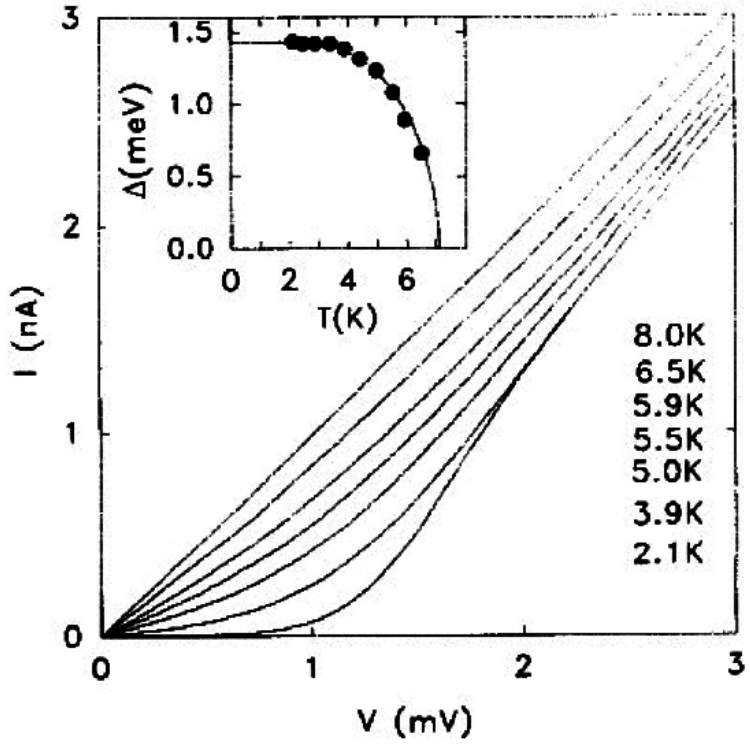

Figure 1.6: I(V) curves taken for a planar tunnelling junction with a granular Pb film on the insulating side of the SIT. Different curves were taken at varying temperatures which are indicated in the figure. The inset shows the extracted Δ value for each temperature. The solid line is a fit to the BCS term. The inset shows the temperature evolution of the gap. Taken from [25].

gap can be extracted from these curves by fitting to the BCS theory. The existence of a superconducting gap in an insulator is shown. Furthermore, the inset which shows the extracted gap versus temperature shows that the gap behaves as one would expect for a BCS superconductor.

1.3.3 Disorder-induced granularity

There is a third SIT class, that includes materials like amorphous indium oxide (a-InO), niobium nitride, titanium nitride and more. While these films are fabricated as homogeneous films, many experiments show unexpected results, which may indicate that these materials are electrically granular.

Apparently, within the seemingly homogeneous matrix separate regions of superconducting and normal-state electrons coexist.

Given below are several examples of such experiments, along with theories that try to explain these phenomena.

$R(T)$ measurements

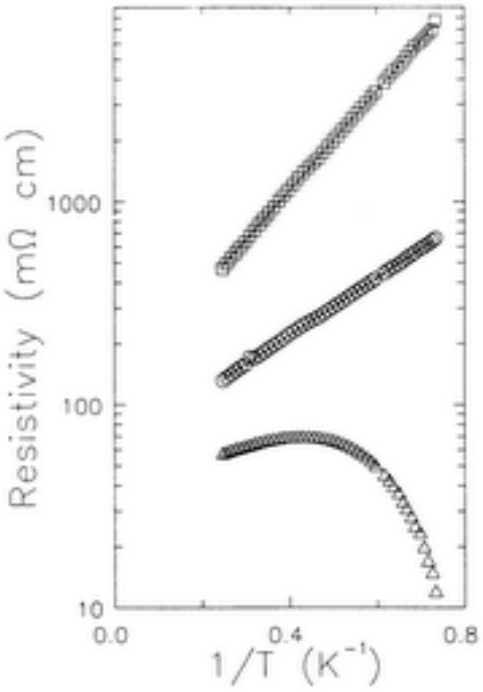

Figure 1.7: (**a**) Resistivity versus inverse temperature curves taken for an a-InO. The as-deposited film is the upper curve. The second and third curves are for the same film after thermal annealing. Taken from [26].

Figure 1.7 shows the $R(T)$ curves for an a-InO film with three different degrees of disorder. The disorder is progressively reduced by thermal annealing at $\approx 50°C$. The two first curves are insulating. The third curve shows a decrease in resistance below some T_c. This decrease is broad, which is not typical for an homogeneous system. It rather resembles the curves seen always in granular superconductors, e.g. those in Figure 1.4.

Scale-dependence

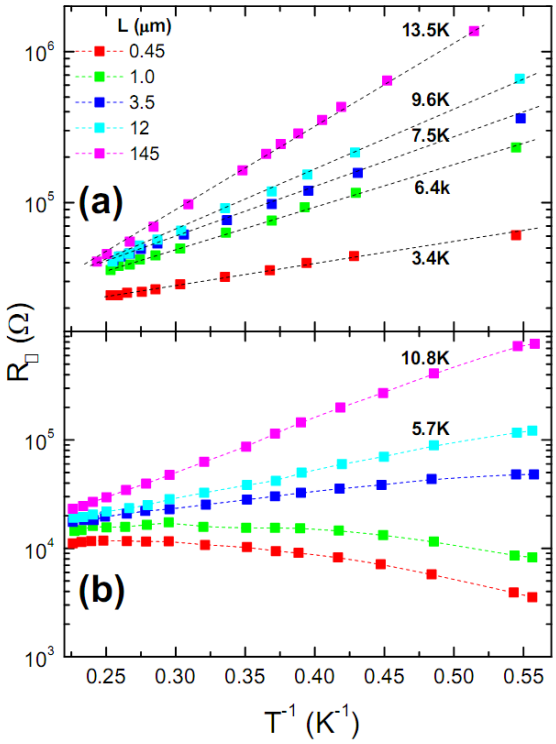

Figure 1.8: (**a**) Transport measurement through several a-InO slabs. All samples were deposited at the same time. The numbers are the calculated T_0 for each graph. (**b**) The same batch of samples measured after thermal annealing. Taken from [27].

When transport measurements were conducted on wide slabs of a-InO, a difference was observed between samples with different lengths [27]. Figure 1.8**a** shows a set of transport measurements conducted on several a-InO slabs that were deposited at the same time, which means that their level of disorder is similar. The difference between the slabs is their length, ranging from 450nm to 145μm.

All slabs show insulating behaviour with simple activation $R(T) \propto R_0 e^{-\frac{T_0}{T}}$. The activation temperature T_0 is higher for the longer ones. After annealing (Figure 1.8**b**) the longer slabs' T_0 is reduced, and the shorter samples turn superconducting. This can only be explained if inhomogeneity is present in

the the a-InO sample on a length scale of several microns. The superconducting puddles that are of the order of the slab's length short-circuiting the shorter ones. According to this set of measurements this characteristic length of the inhomogeneity is of a few microns.

STM measurements

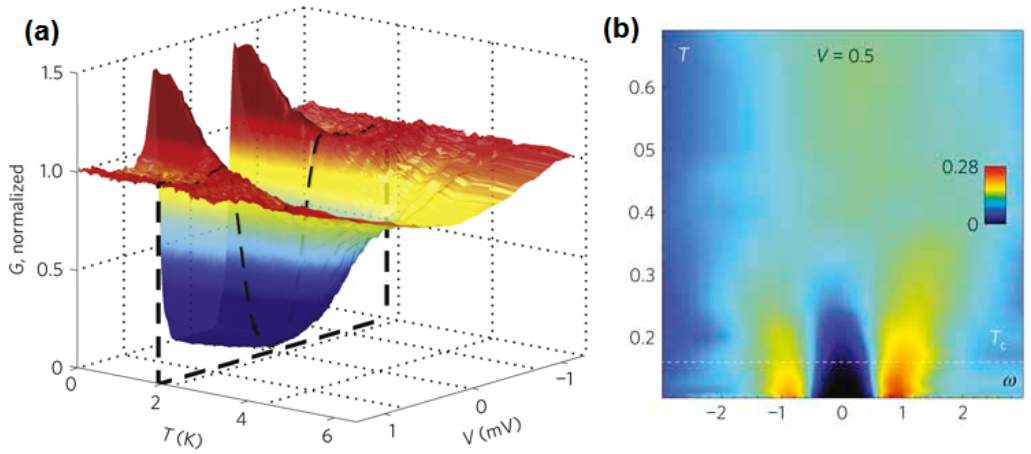

Figure 1.9: (**a**) Tunneling conductance (proportional to density of states, see Equation 3.8) as a function of temperature and voltage bias between the tip and the a-InO film. The dashed line is T_c of the sample as measured via transport through the film. Taken from [28]. (**b**) Density of states as predicted with quantum Monte Carlo calculations. Taken from [29].

Sacepe *et al.* performed local tunneling measurements on disordered a-InO using an STM in a cryogenic system [28]. The results, shown in Figure 1.9, show a depletion of the density of states around the Fermi level at temperatures above the sample's T_c. With lowering the temperature it evolves to the well-known BCS gap form.

This pseudo-gap state is reminiscent of high T_c superconducting cuprates, where a pseudo-gap was measured at temperatures up to 3 times T_c. It may be attributed to a scenario of pre-formed electron pairs which exist above T_c, where large fluctuations prevent these pairs from being coherent [30].

In addition, Figure 1.10 shows a histogram of the gap in an a-InO film. The $G(V)$ curves were measured in a multitude of places across the film, for

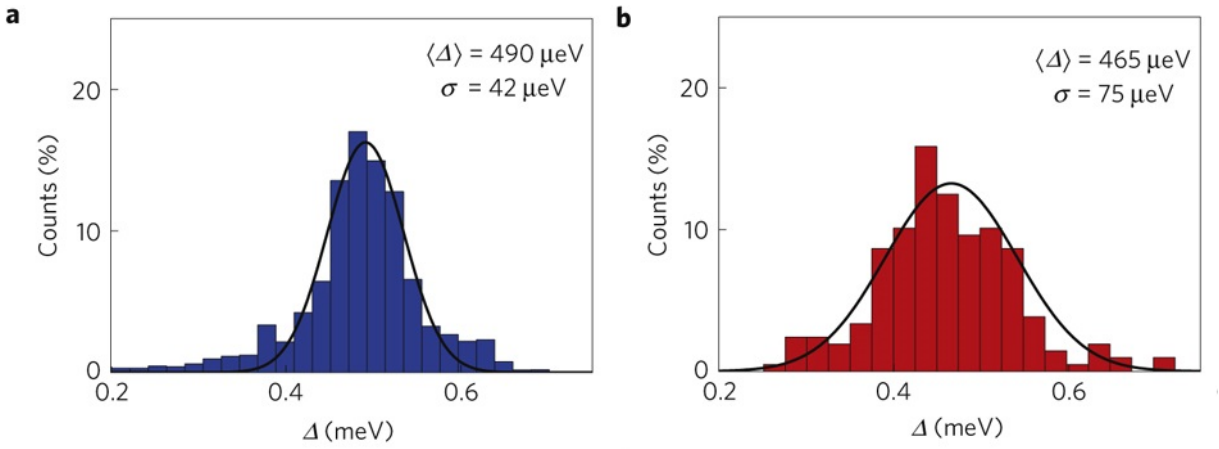

Figure 1.10: Local BCS gap Δ distribution in an a-InO field, measured by STM. The two panels are for **a** low disorder and **b** high disorder. Taken from [28].

each curve the Δ was calculated and the results binned as shown. The mean value of Δ, as well as the standard deviation, show the inhomogeneity of the superconducting state which is increased with increasing disorder.

Magneto-resistance

Figure 1.11 shows magneto-resistance curves of a superconducting a-InO sample at different temperatures. The left panel, which focuses on the small field regime, shows a critical change of behavior at some applied field B_c. Below that field the film is a superconductor while above it the film is an insulator. This signals yet another kind of SIT that occurs in this a-InO sample, that is controlled by the external magnetic field rather than by disorder. Further increasing of the external field to about 8 Tesla the resistance of the film increases by 5 orders of magnitude. At higher fields the trend is reversed and the resistance is decreased, thus forming a very large peak in the magneto-resistance.

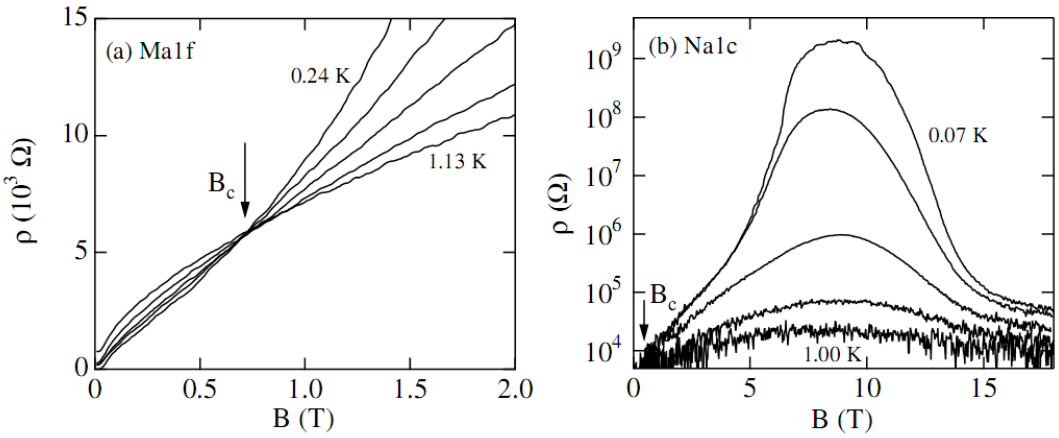

Figure 1.11: Transport measurement as a function of magnetic field through an a-InO thin film. The different curves correspond to different temperatures. The **left** panel is for small magnetic fields, while the **right** shows the full range of the measurement. Taken from [31].

Theoretical model - emergent granularity

Ghosal *et al.* used numerical methods employing an attractive Hubbard model with random potential on each site, to show that a superconducting system which is highly disordered may evolve into a locally correlated system. That is to say, the disorder itself drives the Cooper pairs into "superconducting islands".

Bouadim *et al.* predicted the existence of a peudo-gap, such as the behavior seen in Figure 1.9**a**, by using quantum Monte Carlo methods. Their results are showed in Figure 1.9**b** to show the striking resemblance between experiment and theory.

Disorder-induced granularity also allows an intuitive explanation for the magneto-resistance peak[32], employing electrical granularity, as a crossover between two transport mechanisms: one being tunneling between superconducting puddles, and the other is through the normal regions. At low magnetic fields the superconducting islands are large, making transport through them favorable over the normal regions. As magnetic field is increased the islands become smaller, increasing their charging energy and the distance be-

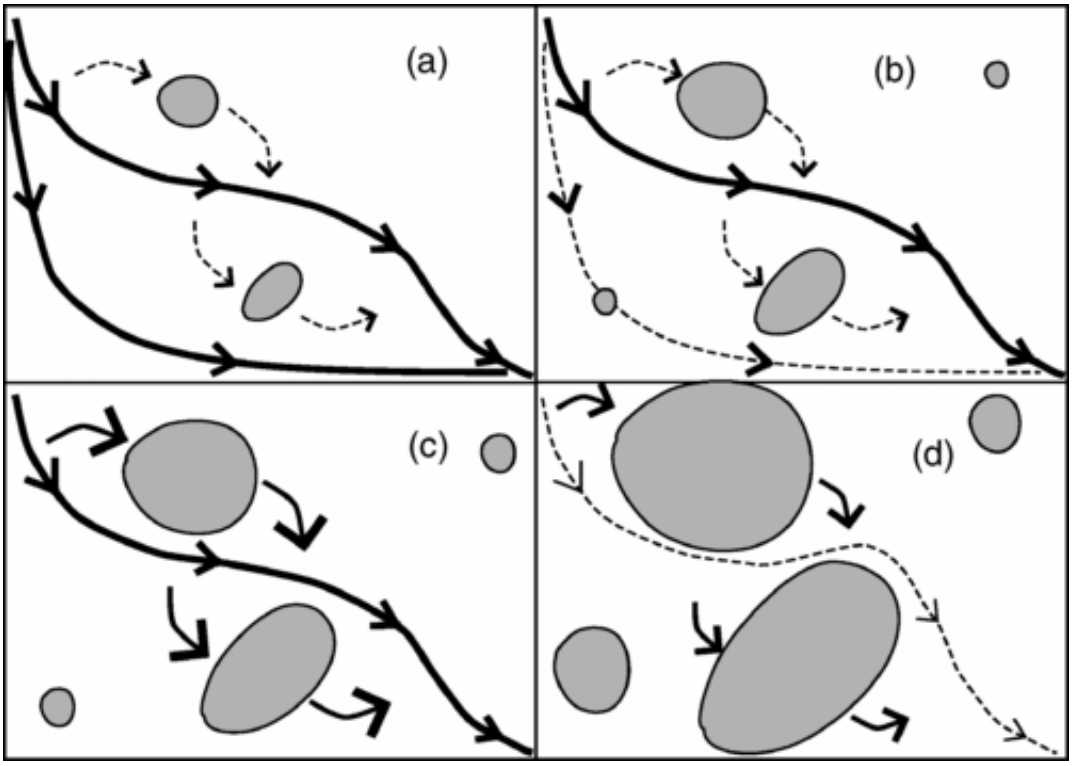

Figure 1.12: A phenomenological explanation for the magneto-resistance peaks observed in a-InO. (**a**) at high magnetic fields the grains grains are small and have a large E_C. Therefore the current "prefers" to traverse the normal-state material around them. (**b**) the islands become larger with decreasing the magnetic field, making the transport of electron pairs between grains increasingly preferable until in (**c**) the two transport mechanisms are comparable. At last with very large grains in (**d**) the transport is mainly through the superconducting grains. Taken from [32].

tween them - making tunneling less likely and widening the normal regions. The peak resistance is where the two mechanisms are equal in resistance, after which the normal regions become wider and eventually they are all that remain. The entire process is sketched in Figure 1.12.

1.4 Quantum phase transitions

The SIT is a manifestation of a quantum phase transition (QPT), a transition between two quantum ground states that is tuned by a non-thermal parameter. The transition between the insulating and the superconducting ground states is an abrupt change in the phase correlation, from some finite value to infinity, that happens as a function of a non-thermal quantity g at $T = 0$.

In our case, the SIT, g is the disorder and the transition occurs at the quantum critical point g_c. The two ground states are characterized by some energy scale δ. This energy scale changes with the control parameter as $\delta \propto |g - g_c|^{\nu z}$, with ν the critical exponent that is usually universal to QPT classes[33], and z the dynamical exponent.

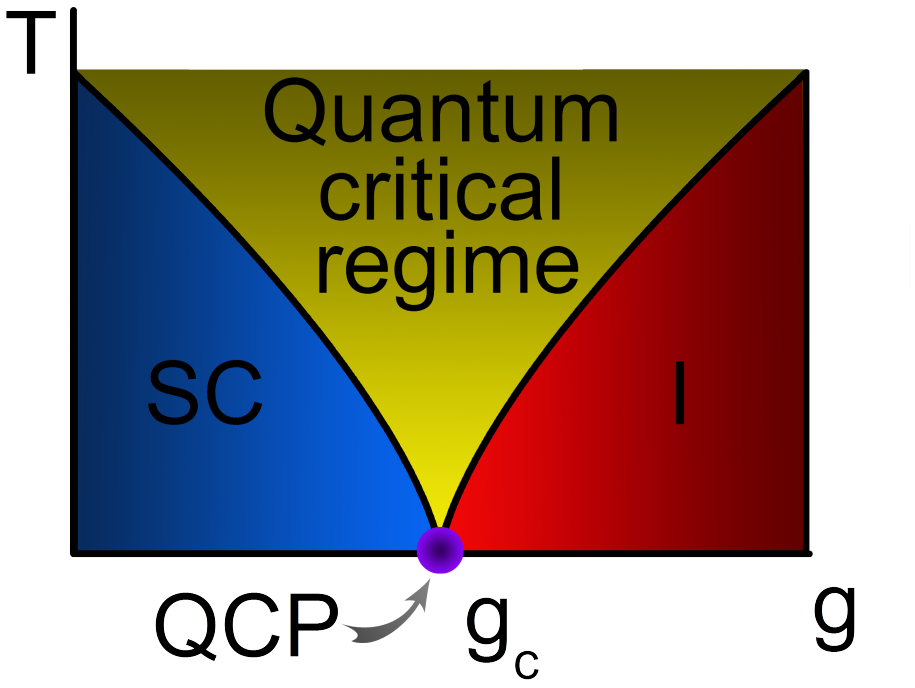

Figure 1.13: Phase diagram near a quantum phase transition. The blue and red regions satisfy $\delta > k_B T$, while the yellow region satisfies $\delta < k_B T$.

After defining the energy scale δ, one can discuss the behaviour of the QPT at finite temperatures, comparing it to k_BT. The two phases will now be separated by a "quantum critical regime" (QCR), in which $k_BT > \delta$. In this regime quantum and thermal are both important in the dynamics of the system.

For the SIT, since in finite temperatures no solid-state system is truly an insulator, there is no real transition between the insulating phase and the QCR, but rather a smooth crossover. On the other hand superconductors do exist in finite temperatures, and so one would expect to see a transition between the superconducting phase and the QCR [34].

1.5 Heat capacity of superconductors

In any normal crystalline solid there are two contributions to the heat capacity, as heat is absorbed both by lattice vibrations (phonons) and by electrons. At low temperatures the phonon's part is derived from the Debye model [35] to be proportional to T^3 while the electronic contribution to heat capacity is proportional to T. The total heat capacity is therefore

$$C_p = \alpha T + \beta T^3 \tag{1.20}$$

where $\alpha = \frac{1}{3}\pi^2 D(\epsilon_F) k_B^2$ with $D(\epsilon_F)$ the electron density of states at the Fermi level, $\beta = \frac{12\pi^4 R}{5\Theta^3}$ with $R = 8.31 \frac{J}{molK}$ the gas constant and Θ the Debye temperature.

When a material undergoes a phase transition the heat capacity is strongly affected. For first-order phase transitions, e.g. water to ice, the entropy shows a discontinuity between the ordered and disordered phases. This causes a delta function of the heat capacity at the transition. The area under this delta function, L, is the amount of energy it takes to change the phase of the material from one to the other, and known as latent heat. In a second-order phase transition, e.g. the Ising ferromagnetic transition, the entropy is not discontinuous, however its different behaviour below and above the transition gives rise to a discontinuity in its first derivative that is proportional to the

heat capacity.

Near the transitions different physical parameters behave as power laws. For example, above the transition temperature the correlation length behaves as

$$\xi \propto (T - T_c)^{-\nu} . \tag{1.21}$$

In a similar manner, the heat capacity and susceptibility have critical exponents noted as α and γ, respectively. Below T_c different critical exponents exist for the same quantities.

A lot of information is hidden in the thermodynamics of a system. This makes heat capacity measurements a fertile ground for new information about the systems in focus, disordered superconductors. However, in order to understand the effect of disorder on the system we must first understand the clean limit.

1.5.1 Bulk superconductors

The superconducting transition is a second-order phase transition, characterized by a discontinuous jump in its heat capacity C_p at the transition temperature T_c. This jump, ΔC_p, arises due to the change in entropy of electrons which are paired below T_c and unpaired above it, and its size is proportional to the electronic heat capacity just above the transition $C_{p_n} = \gamma T_c$ and is calculable by BCS theory [36]

$$\frac{\Delta C_p}{C_{p_n}} = 1.43 \tag{1.22}$$

When further decreasing the temperature below T_c the superconducting gap grows as

$$\Delta (T) = 3.07 k_B T_c \sqrt{1 - \frac{T}{T_c}} \tag{1.23}$$

thus the heat capacity is reduced exponentially, following [37]

$$C_{p_s} = 1.34 C_{p_n} \left(\frac{\Delta (0)}{k_B T} \right)^{\frac{3}{2}} e^{\frac{\Delta(0)}{k_B T}} \tag{1.24}$$

Figure 1.14, shows the sharp specific heat jump at the superconducting transition for lead.

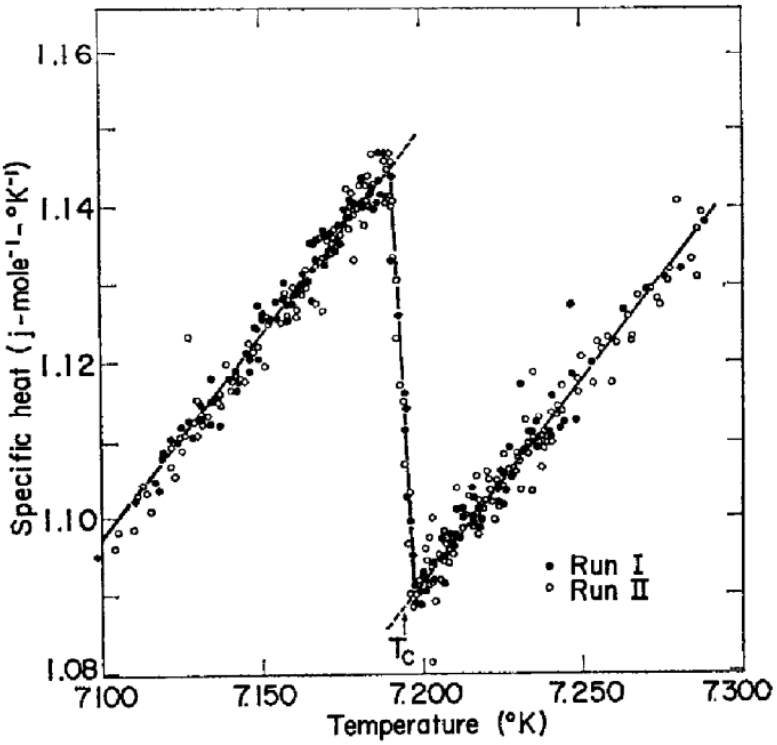

Figure 1.14: Heat capacity jump at the superconducting transition of lead. Taken from [38].

1.5.2 2D superconductors

Ovchinikov and Varlamov showed [39] that an excess heat capacity emerges from fluctuations near the BKT transition in thin films of thickness $t << \xi_{LG}$. This heat capacity grows when reducing the thickness of the films as

$$C_{excess}(\tau) = \frac{8\pi^2 St}{7\zeta(3)}\nu T_c \left(\frac{Gi_{2D}}{\tau}\right) - \frac{48\pi^2 St}{7\zeta(3)}\nu T_c \left(\frac{Gi_{2D}}{\tau}\right)^{\frac{1}{2}} \tag{1.25}$$

where $\tau = 1 - \frac{T}{T_c}$ is the reduced temperature, $\zeta(x)$ is the Riemann function with $\zeta(3) = 1.202\ldots$ and ν is the electron density of states at the Fermi

level. Gi_{2D} is the Ginzburg-Levanyuk number which equals

$$Gi_{2D} = \frac{21\zeta(3)}{\pi^2}\frac{1}{p_F^2 t l_{tr}} \tag{1.26}$$

with p_F the Fermi momentum and l_{tr} the electron mean free path. The first and second terms in the right hand side of Equation 1.25 correspond to long and short wavelength order parameter fluctuations, respectively. After substituting Equation 1.26 into Equation 1.25, one gets a dependence of

$$C_{excess}(t) \propto A - B\sqrt{t} \tag{1.27}$$

with A and B constants indifferent to t.

1.5.3 0D superconductors

When a small grain of a superconducting material is cooled below T_c, two factors come into play that smear the superconducting transition, by making it broader and suppressing ΔC_p. The two effects were shown in a paper by Mühlschlegel *et al* [40].

One of the factors is the approach towards the Anderson criterion, in which the energy levels separation becomes increasingly larger with reducing the grain diameter, eventually surpassing the superconducting gap and thus prohibiting superconductivity altogether.

However, in their paper it is shown that the effect of single-electron level discreteness becomes important only when the level spacing δ is of the order of $k_B T_c$ or less. This renders the effect negligible in most experiments.

A more important factor, which exists also in larger grains, is the constant number of electrons. By projecting grand-canonical ensemble calculations to the canonical ensemble, it was shown that this effect also smears out the transition seen in heat capacity.

Heat capacity of small superconducting grains has been measured in the past and was shown to be in excellent agreement with theoretical predictions of $C_p(T)$ [41], [42]. An example is given in Figure 1.15, showing the heat capacity of fine grains of Sn.

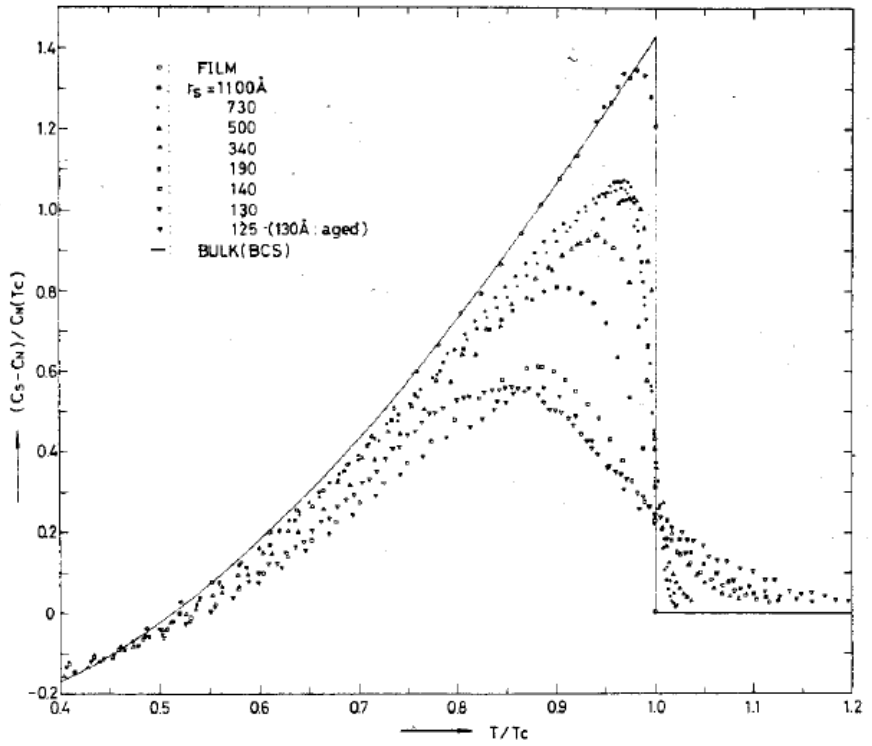

Figure 1.15: Heat capacity of small grains of Sn of different sizes. The solid line is the BCS form calculated for bulk Sn. Small grain sizes smear the transition, making the jump less prominent. Taken from [41].

1.6 Magnetic force microscopy

The atomic force microscope (AFM) was first described by Binning *et al.* [43] in 1986. In their paper they describe a method to measure forces as small as $10^{-18}N$ exerted on a diamond sharpened at its tip down to a single molecule. The tip is located at the end of a long cantilever and brought to a close proximity with a surface. The forces, e.g. van der Waals, affect the tip and move the cantilever. The displacement of the cantilever is measured with high accuracy by the reflection of a laser.

Improving this technique, in 1987 Martin *et al.* [44] forced the oscillation of the cantilever at its resonant frequency. This frequency changes with the gradient of an external force when one is introduced. This method allows one to measure long-distance forces with more accuracy and with no risk of

damaging the sample when working in close proximity to its surface.

Modifications can be made to the measurement system in order to obtain information from the different forces. When one wants, for example, to access the information of electric forces and fields, one may add a conductive layer to the tip [45]. Magnetic forces are sensed by a magnetic tip, chemical reactions can be measured by applying one of the reactants to the tip, etc.

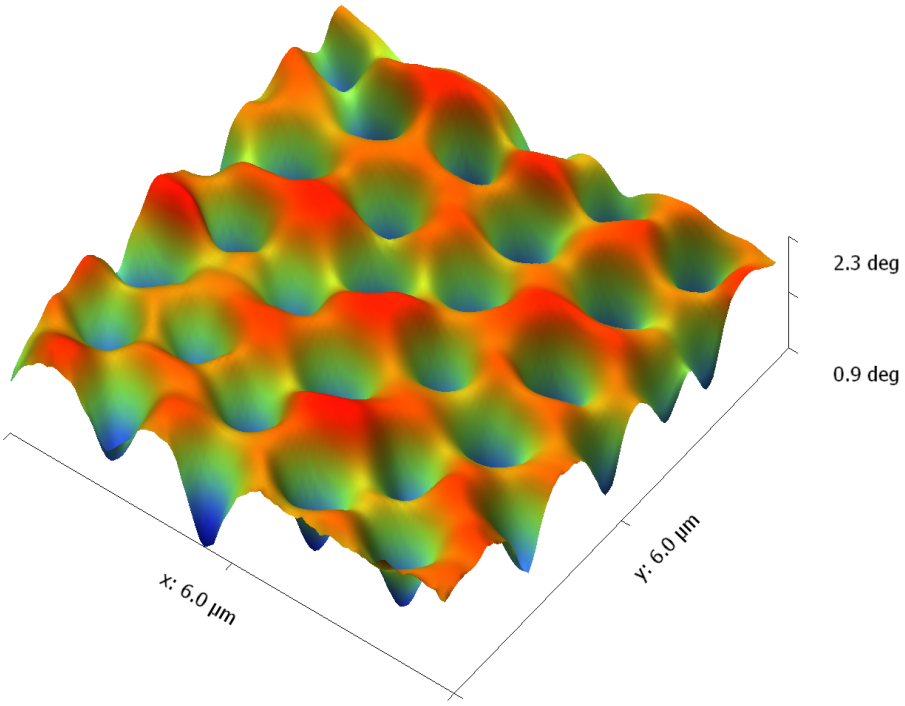

Figure 1.16: A constant-height MFM scan of a niobium film in the mixed state, taken with the system used in this study. each concave cone is where a superconducting vortex resides.

The field of superconductivity has benefited greatly from using scanning force microscopy. Being perfectly diamagnetic, superconductors provide a rapid change in magnetic field close to the surface. Magnetic measurements of vortices in the mixed state of low-T_c and high-T_c [46]–[48] were used to study the traits of the vortex lattices [49], vortex pinning [50] and other superconductivity-related phenomena. Figure 1.16 shows an example of vor-

tices in a superconducting niobium film imaged by the MFM used in this study.

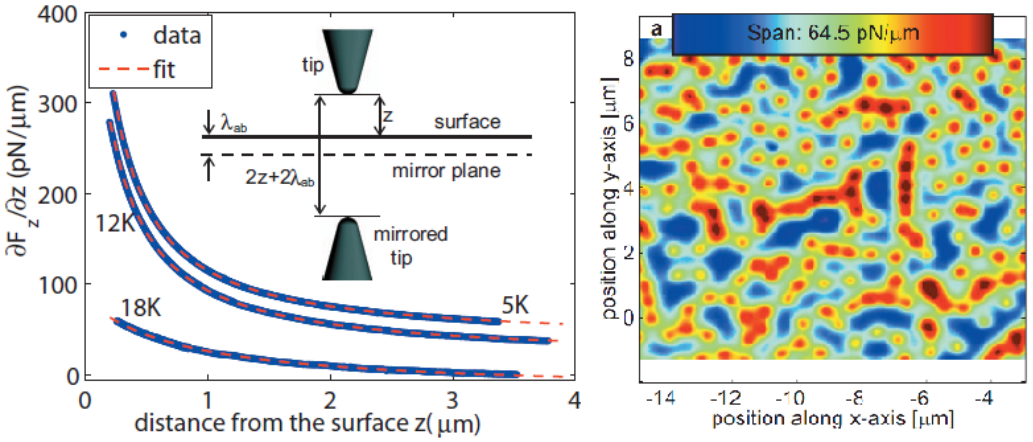

Figure 1.17: (**left**) Force derivative (as explained in section 3.4) as a function of tip-sample distance for a pnictide superconductor. Inset: image dipole technique used to calculate the force between the tip and the surface. (**right**) a force derivative scan showing the non-uniformity of λ_L through the disordered array of vortices where in the uniform case one would expect an Abrikosov lattice. Taken from [51].

Lately, a measurement of the local London penetration depth of a pnictide superconductor was performed by Luan *et al.* [51]. In their paper the authors measured the magnetic force versus tip-sample distance. If the superconducting film is infinite relatively to the tip size, the Meissner force it exerts on the tip can be calculated using a mirror dipole, much like the image charge technique used to calculate the force between a charge and a grounded plane. Since superconductors have a penetration depth, the mirror plane will be located at a distance λ_L below its physical surface. The authors used this feature to extrapolate the force curves they measured above the surface and find the point where the tip and its image would collide. Some of their results, as well as a sketch for the mirror dipole calculation, are given in Figure 1.17, showing two different methods they used to show the non-uniformity of λ_L in this material. The first method, shown in the left panel, is the measurement of distance-force curves. When temperature is reduced these

curves seem to diverge faster as λ_L is reduced and the divergence point of the Meissner force, when the dipole touches the mirror plane, is approached. λ_L is a fit parameter for these curves. The second method, shown in the right panel, does not allow the calculation of λ_L. The non-uniform scatter of vortices is a measure for the non-uniformity of the penetration depth, as the vortex-vortex interaction is dependent on it. See Equation 1.7.

We can see that MFM measurements, either surface scanning or tip-surface distance curves, are handy in characterization of magnetic materials, especially superconductors. In our experiment we try to use these techniques to shed new light on superconductivity in disordered a-InO.

1.7 Superconducting proximity effect

When a metal comes in good electrical contact with a superconductor Cooper pairs leak from the superconductor into the metal, inducing a gap in the metal that decreases exponentially with distance from the superconductor [52], [53].

If the metal is dirty, with mean free path l_N shorter than the superconductor's coherence length, the decay length of Cooper pairs in the metal will vary as:

$$\xi_N = \left(\frac{\hbar v_N l_N}{6\pi k_B T}\right)^{\frac{1}{2}} \tag{1.28}$$

where v_N is the Fermi velocity of the metal [55].

At the same time, the superconducting gap is decreased in the superconducting material close to the boundary [57], [58] on lengths scales of the characteristic coherence length. The effect of metal-superconductor proximity is schematically summarized in Figure 1.18, which shows the superconducting gap near the interface. The reduction of the gap in the superconductor causes a decrease of T_c in the superconductor and can, in some cases, reduce it down to zero [56], [59]. Figure 1.19 shows this T_c reduction in the interface between a normal metal and an superconductor thin films as a function of metal thickness and superconductor thickness.

A special case of the proximity effect was observed in granular Pb films.

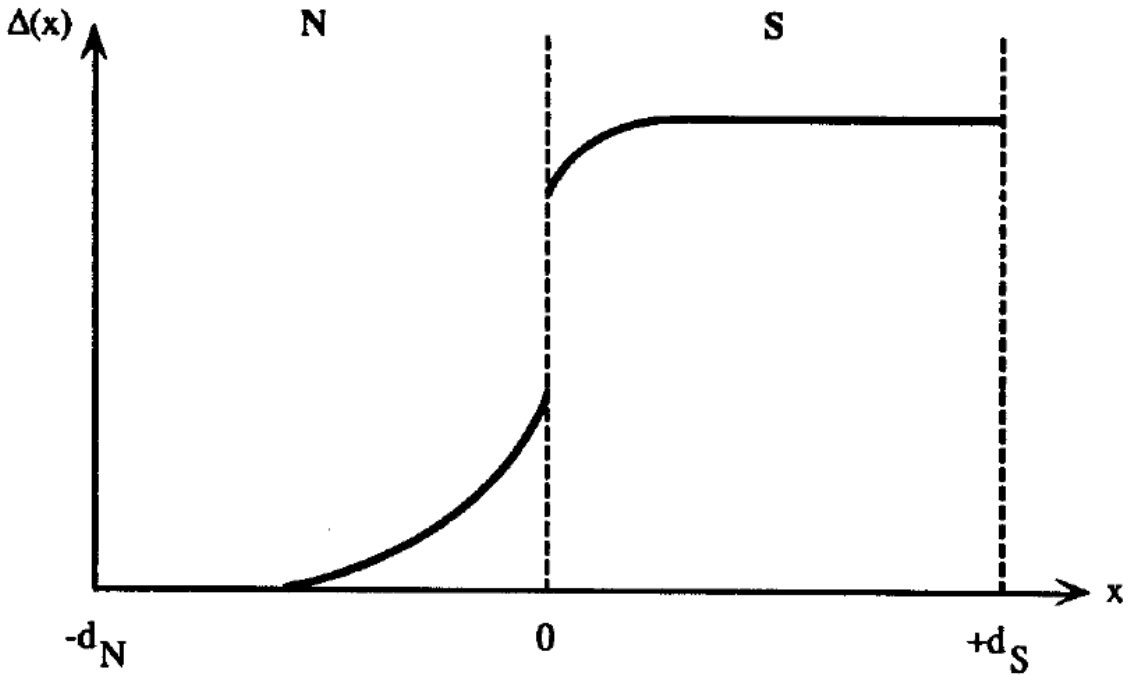

Figure 1.18: Superconducting gap as a function of position. The interface between the normal and the superconducting regions is at $x = 0$ with the normal metal to the left and the superconductor to the right. Taken from [54]

.

The addition of a metallic layer on top of an insulating granular layer of lead has turned it into a superconductor [60], [61].

$R(T)$ curves of this proximity effect experiment are shown in Figure 1.20. In this experiment, first granular Pb is deposited on a substrate. Curves **a** and **b** are seen in this stage. The following stages are for the gradual addition of silver on top of the Pb.

Silver is a non-superconducting metal, and so the fact that a transition is seen, making the film superconducting, is *a-priori* unexpected.

The change is gradual as layers of Ag are added. Curves **c**-**f** show the sharpening of the transition. We may attribute this sharpening to the in-

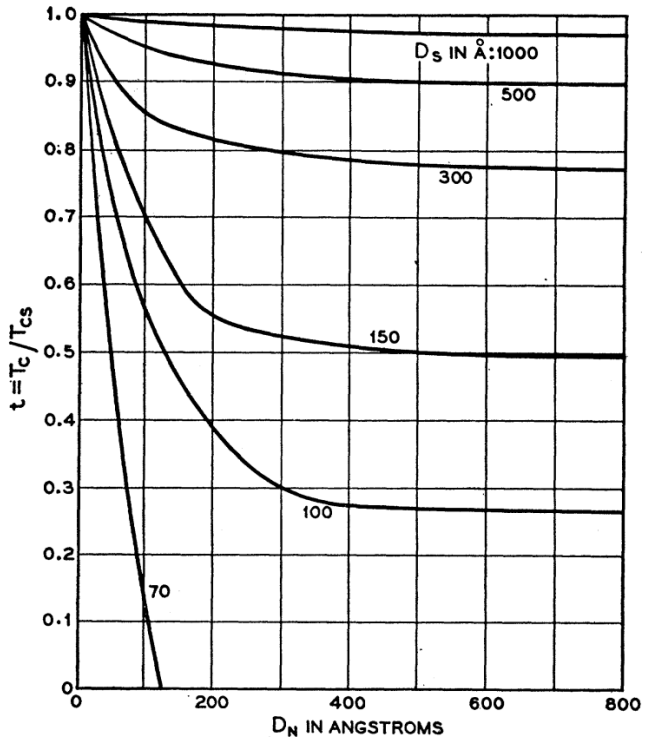

Figure 1.19: Change in superconducting transition temperature plotted versus the thickness of the normal metal near a normal-superconductor interface. The thickness of the superconductor is noted next to each curve. Taken from [56]

.

crease in phase coherence between the grains. At later stages, the transition is very sharp, however the inverse proximity effect decreases the T_c down to 2 Kelvin.

If indeed the insulating side of the granular SIT is comprised of superconducting islands, and the insulating behaviour stems from the incoherence of phases across the different grains, this effect can be explained as the increasing of the phase coherence between the grains by making them effectively larger and closer to one another.

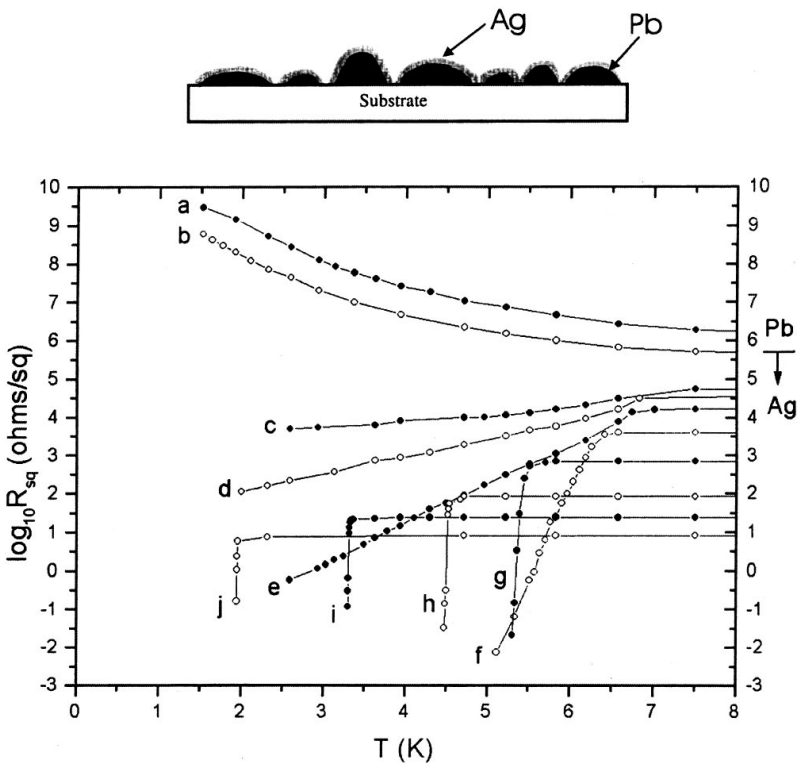

Figure 1.20: Sheet resistance of Pb/Ag layers. Curves a and b are for Pb layers, curves c-j are for the Pb layer from b with incremental addition of Ag. Taken from [60]

.

Chapter 2

Research motivation

The main goal of this work is to study different properties of materials that undergo a disorder-tuned superconductor-to-insulator transition. We focus on granular materials: either quench-condensed films that are structurally granular, or a-InO films that are believed to be electrically granular at low temperatures.

The SIT is of great interest as it is a manifestation of a quantum phase transition. The fact that it is observed in different systems and that it is tuned by various parameters, makes it a universal phenomenon rather than just an odd happenstance. A variety of theories arose around this subject, as well as various peculiar experimental findings.

To date, most of the experimental work that has been done on the SIT has focused on transport properties. These measurements are susceptible to percolation since the electric current has to flow from one electrode to the other. The current chooses the easiest path to traverse the sample and is thus susceptible to the sample inhomogeneity. In addition, the study of the insulating part of the SIT poses a challenge in measurement of extremely high resistances. In contrast, two of the experiments we report in this work, i.e. the heat capacity and the MFM experiments, do not depend on electric current traversing the studied material and therefore have clear advantages and provide important information inaccessible by conventional means.

The third experiment, involving the superconducting proximity effect,

supplements these by providing additional insight to the percolation nature of the transport through a disordered superconductor.

Heat capacity

In the first experiment we measure the heat capacity of thin quench-condensed granular Pb films. This is a global measurement, that measures the entire film's heat capacity at once. It is not at all sensitive to percolation arguments that are susceptible to the sample's inhomogeneity, and it is capable of measuring films with extremely high resistivity, as it does not depend on electron transport through the film.

Heat capacity measurements can uncover the physics behind phase transitions. Unique features are observed near classical phase transitions, that are driven by thermal fluctuations, such as divergence of the heat capacity (first-order transition) and critical exponents of different thermodynamic functions. One may expect such phenomena to show up in quantum phase transitions and in the quantum critical regime, where quantum fluctuations drive the transition as well . The measurement of such critical exponents is of great value, and may decide between different microscopic scenarios that were proposed to explain the SIT.

This kind of measurement is not limited to the SIT, and the set-up used in this study can also provide information about other QPTs in materials with extremely small masses.

Local magnetism

This experiment is aimed at measuring local magnetism effects in a-InO films. It is conducted by a magnetic force microscope, which can resolve sizes as small as 30nm.

Several experimental indications have been reported in the past few years that point at the existence of superconductivity at temperatures up to $2T_c$, where T_c is defined by transport measurements and hence is determined by the temperature at which the superconducting system is coherent across the film. Local diamagnetic signals, that we probe with the MFM, are expected

to be detectable in superconducting films even where global superconductivity does not exist.

We also use this tool to measure the local penetration depth of a superconducting a-InO film. One would expect the penetration depth variation to be large, as it is virtually infinite in regions with no superconductivity. Near superconducting islands it is expected to be much smaller. Measuring local penetration depths with such large variance between different sites will be a strong indication for the electrical granularity of the film.

Proximity effect

The third experiment is based on transport measurements. In this experiment we deposit a layer of gold on top of an a-InO thin film. This layer acts to allow superconductivity to spread through it by the proximity effect, and by doing so increases the coupling between neighbouring grains.

The gold is deposited *in-situ* by quench condensation. This allows us to deposit very small quantities, making the onset of the proximity effect gradual. By this we are able to see intermediate stages, rather than just the effect of bulk gold on the a-InO film.

By adding this layer we wish to change the level of phase coherence between superconducting islands in the films, and to quantify the change in the transport characteristics. Using this technique we probe how the percolation of superconductivity is affected in the film.

The granularity of a-InO films is emergent rather than structural as in the experiment we discussed in the introduction, and so differences in the results of the two experiments may be seen, and will be used to gain insight into emergent granularity.

Chapter 3

Experimental techniques

3.1 Quench condensation

The quench condensation technique allows the fabrication of ultra small grains or ultra-thin films of various materials. It is performed inside a vacuum chamber at cryogenic temperatures, allowing *in-situ* sequential deposition of clean layers without exposing the films to atmospheric conditions and room temperatures, both harmful to the samples.

Quench condensation is basically a thin film deposition technique employing physical vapour deposition. The uniqueness of the quench condensation technique is that the substrate is kept at low temperatures by thermally coupling it to a cryogenic heat bath. This means that the evaporated atoms that adhere to the surface become rapidly immobile, as their kinetic energy is transferred to the heat bath. Despite this rapid freezing process, nucleation sites may be present in the substrate which attract additional nearby atoms, resulting in a granular film on our silicon substrates. One may add a wetting layer of Sb or Ge before performing the quench-condensing. This makes the atoms adhere better to the surface, and will result in uniform rather than granular films.

The quench-condensation set-up allows the study of ultra-thin films as a function of thickness with a sequential deposition of layers on the same sample. It is done *in-situ* without the need to heat up the sample or exposing

it to the atmosphere.

In our study we use quench-condensation for two of our experiments. One is the heat capacity experiments, where the studied samples are granular Pb or Sn films, and the second is the proximity effect where we use a quench-condensation set-up in order to deposit a thin layer of gold, to act as a proximity layer, on top of a-InO samples. The two experiments were performed in two different systems, but the essentials of quench-condensation are the same in both.

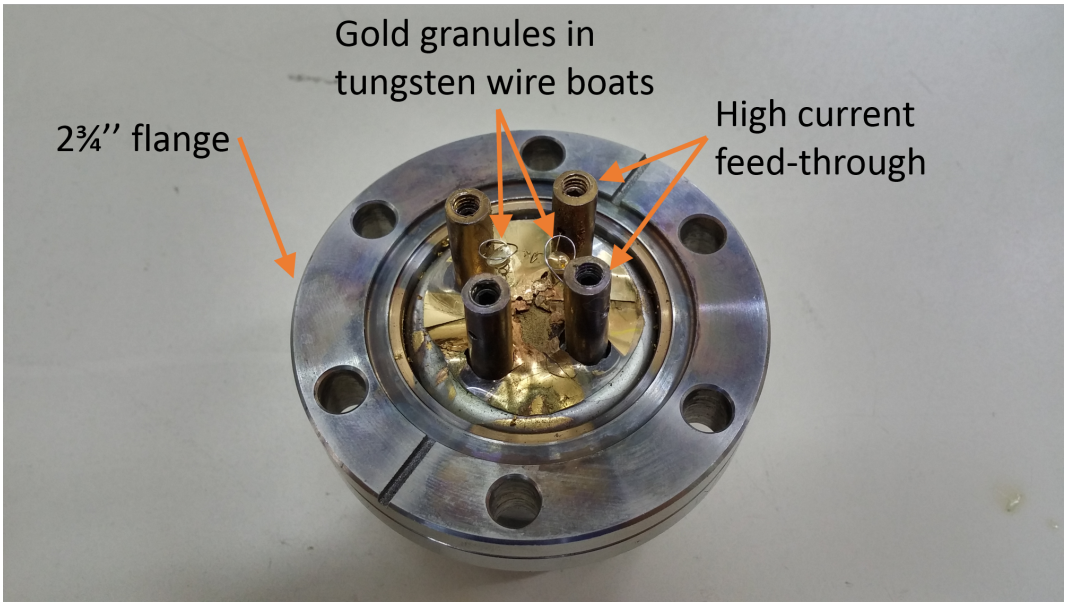

Figure 3.1: The physical vapour deposition source used in the proximity effect experiment. The four metallic columns that feed the current for the evaporation boats exit the chamber without breaking the vacuum inside.

The set-up consists of electrical wiring that run from the room-temperature current source, through the helium bath, and into the bottom of sample chamber. In order not to break the vacuum in the chamber we use a commercially available $2\frac{3}{4}''$ flange with electrical feed-through that was modified to hold the deposition source in the proximity effect set-up. In the heat capacity experiment set-up we use copper wires that feed through a copper container filled with helium-tight Stycast resist brazed on the stainless steel

flange.

In both systems a tungsten wire is wound to form a conical helix shape, to be used as the evaporation boat. A small granule of the material to be deposited is placed inside this cone. The feed-through are inserted into a vacuum chamber and connected to a current source. Current is driven through the boat to the point where the material is melted. This ensures that when moved and handled later the granule does not fall out of the boat. Figure 3.1 shows the melted granules and the evaporation set-up used in the proximity effect experiment.

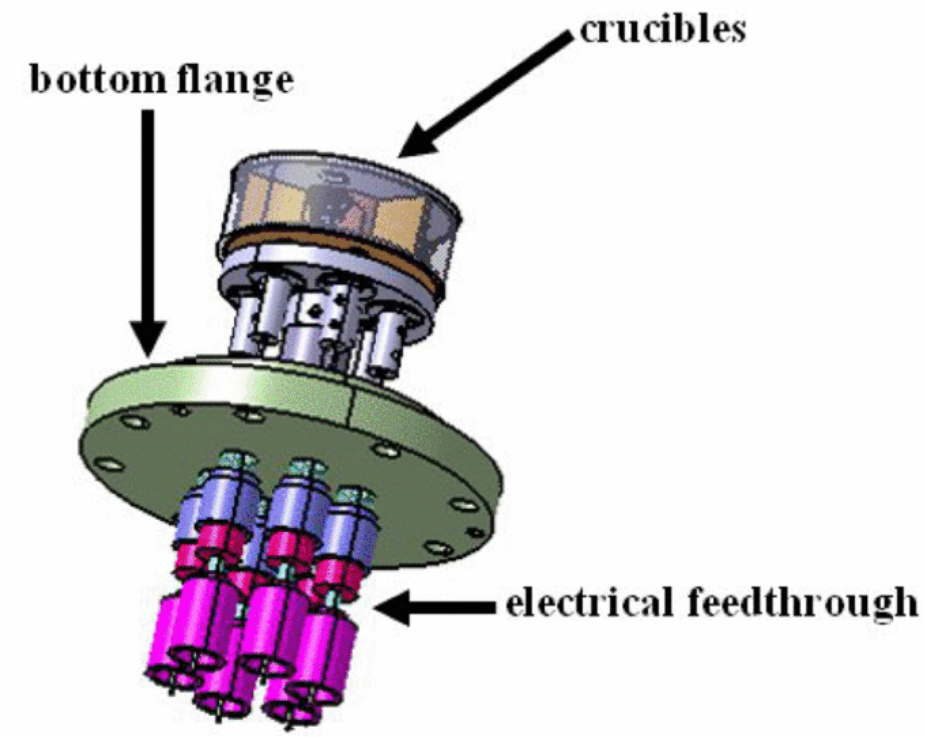

Figure 3.2: A sketch of the quench-condensation source used in the heat capacity experiment. The copper wire feed-through container (magenta) is filled with stycast to prevent leaks. The wire itself is connected at its end to tungsten crucibles that are covered with a stainless-steel radiation shield.

The boats are covered by a metallic shield, with holes perforated above the boats, to prevent heat from radiating and heating up the sample during deposition. Figure 3.2 shows a sketch of the quench-condensation set-up

used in the heat capacity experiment, including the stycast feed-through, the evaporation boats, the flange and the radiation guard.

3.2 a-InO

We performed two of our experiments on thin a-InO films. The first is the magnetic force microscopy experiment, where the thin films were magnetically characterized, and the second is the proximity effect experiment, where a metallic layer was deposited on the a-InO films.

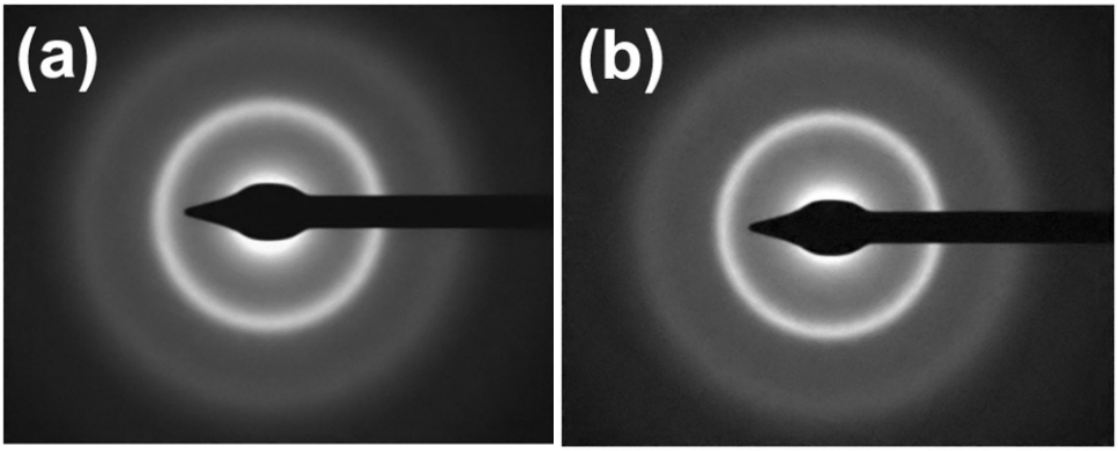

Figure 3.3: Electron diffraction pictures of an indium oxide films before (**a**) and after (**b**) thermal annealing. The diffraction pattern indicates the amorphousness of the films. Taken from [62].

The a-InO films used in our study were e-gun evaporated on a room-temperature substrate with 99.999% (5N) pure crystalline indium oxide pieces as the target. The deposition chamber's base vacuum was better than 10^{-6}mbar. High purity oxygen gas was introduced into the chamber by a needle valve at a pressure of $(1-5)\times 10^{-5}$mbar. In this oxygen environment, deposition was performed at rates of $0.5-1\frac{\mathring{A}}{s}$. Indium oxide films fabricated in this manner were shown in the past [62] to be completely amorphous even after a long thermal annealing at temperatures up to 90°C. Figure 3.3, taken

from [62], shows electron diffraction images of such a film before and after the annealing process. In both cases the material is amorphous.

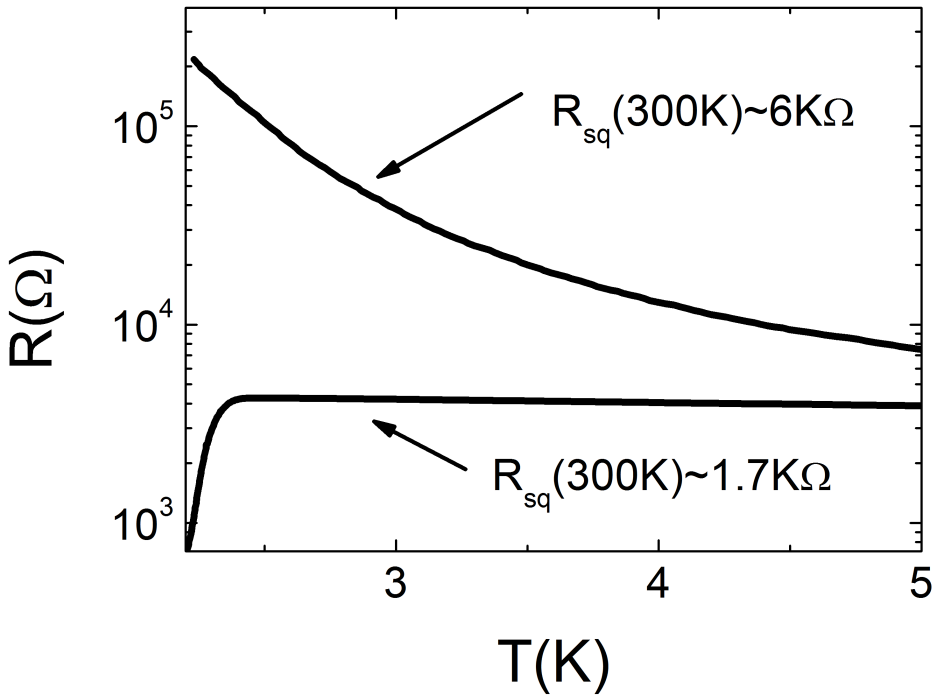

Figure 3.4: $R(T)$ curves for a superconducting a-InO sample with $T_c \approx 2.3$K and an insulating a-InO sample with $T_0 \approx 5.5$K. The two are differentiated by their room-temperature resistance.

The oxygen pressure and deposition rate determine the film's level of disorder. Samples deposited with higher oxygen pressures and lower deposition rates have a greater degree of disorder. In general samples having room-temperature resistance larger than $2\frac{K\Omega}{\square}$ are insulating at low temperatures. Their counterparts, samples with lower oxygen levels and higher deposition rates, have a room-temperature sheet resistance of the order of $2\frac{K\Omega}{\square}$ and less, and at low temperatures form a superconductor. An example for the $R(T)$s for a superconducting and an insulating a-InO films is shown in Figure 3.4.

3.3 Specific heat measurements

3.3.1 Sensor preparation

In order to determine the heat capacity of a system, it is necessary to supply heat into it and measure its temperature change. In our system we use a thin film heater and a thin film thermometer for those purposes.

The measurement of thin films that undergo the SIT poses a difficulty as the system is inevitably coupled to a substrate that also holds the heater and the thermometer. A great challenge it is to minimize the heat capacity of the substrate and the different component to be of the order of that of the deposited film's heat capacity.

We use a unique fabrication process with cooperation with Olivier Bourgeois' group in institute Neel, Grenoble. Thanks to their expertise we are able to fabricate samples in which the substrate's heat capacity is comparable to the thin film's heat capacity, and does not overshadow it in the measurements.

In the following subsections we detail the fabrication process of the calorimetric cell (CC).

Silicon thinning

In order to reduce the heat capacity contribution of the substrate to a minimum, we use wet etching of the silicon with KOH in order to thin a $4mm \times 4mm$ square part of a $15mm \times 10mm$ silicon die.

The etching is performed on the back side of the die, as seen in Figure 3.5, leaving the front face flat for the next fabrication steps. The silicon is covered by a $200nm$ thick SiN, which is not affected by the KOH. Selective etching is achieved by removing the SiN using reactive ion etching (RIE) with SF6 gas.

Leads

The front side of the die is covered by 100nm thick niobium titanium layer topped by a 30nm thick gold layer to protect it from oxidation. Resist is then

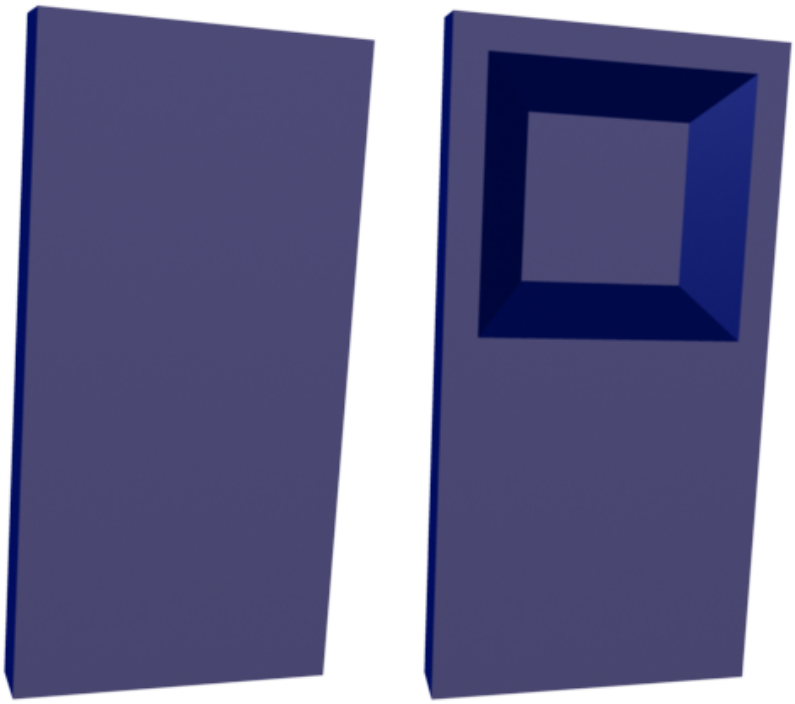

Figure 3.5: The back side of a silicon die, the left die is before etching, and the right die is wet-etched in order to thin the active part of the calorimeter.

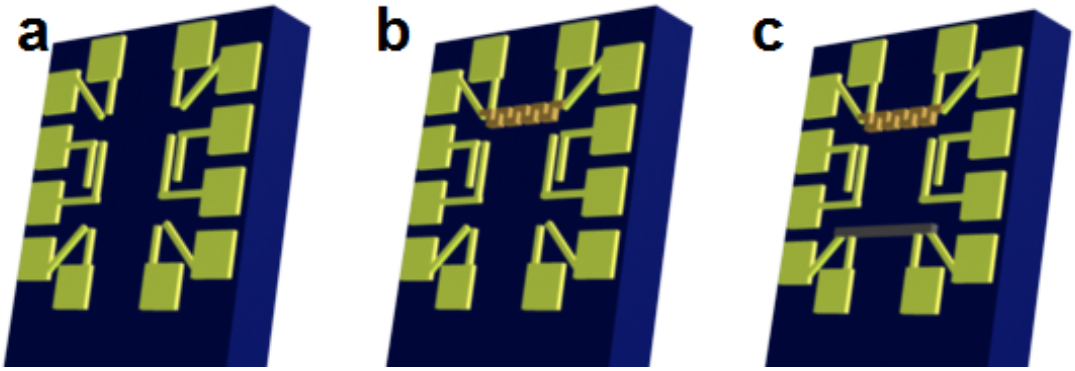

Figure 3.6: **a** A CC after the fabrication of leads that go to the thinned section of the silicon. **b** The same section after deposition of the copper heater. **c** The same section after deposition of the NbN thermometer.

spin coated on the bilayer and defined by a photo-lithography process into eight thin wires that lead from the thick part of the silicon to the thinned part. These will be used as electrical wiring for the different components on the sensor. The excess material is removed by wet etching with potassium iodide for the gold layer and hydrochloric acid for the NbTi. A sketch of the result can be seen in Figure 3.6**a**.

Heater

In order to measure the specific heat we need to supply heat to the system and measure the change in its temperature. The heat is supplied by a 200nm thick copper meander deposited in a lift-off process.

The resistance of this meander is rather constant in the temperature range of our measurements, and so a steady current supplied to it will dissipate into the same amount of heat through Joule heating. A sketch of the result can be seen in Figure 3.6**b**.

Thermometer

The thermometer is made of a $200nm$ thick niobium nitride (NbN) film deposited as a long slab on four of the NbTi wires, defined by a photo-lithography lift-off process. It is deposited by a plasma deposition. The base pressure in the plasma chamber is approximately 10^{-7} mbar. During the deposition process argon and nitrogen gas flow through the chamber, with the pressure regulated to 2×10^{-2} mbar. A pulsed power supply operating at 275 kilohertz creates the plasma. The partial concentration of each gas in the mixture and the working frequency of the power supply determine the properties of the deposited film. Higher nitrogen concentrations and higher frequencies yield films with higher resistance. A sketch of the result can be seen in Figure 3.6**c**.

In order to optimize the heat capacity measurement, it is essential to have a thermometer which has a low resistance and a high sensitivity to

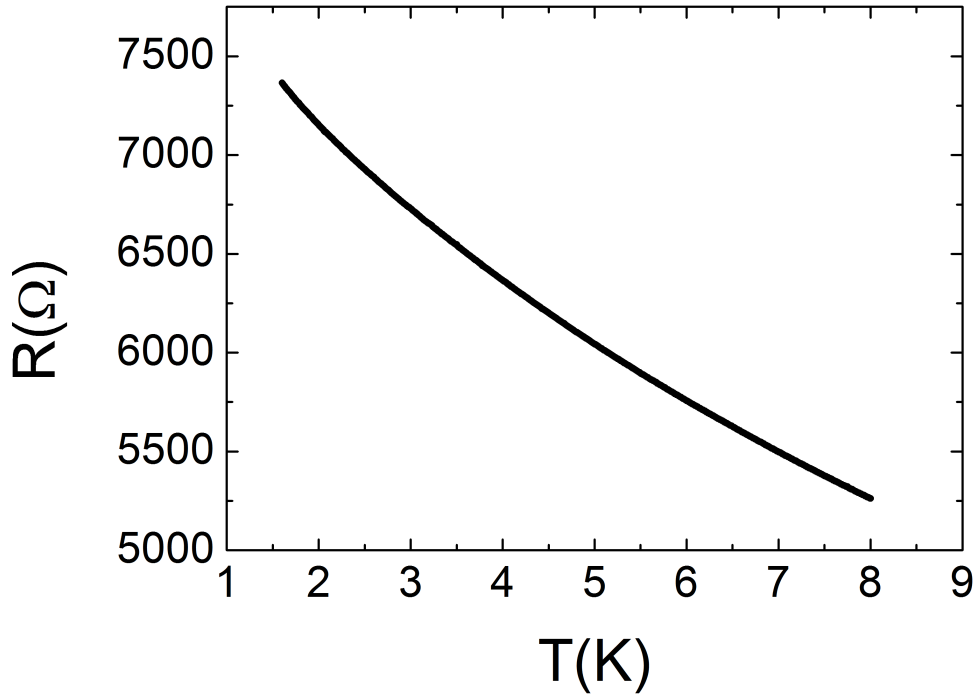

Figure 3.7: $R(T)$ curve of a NbN thin-film thermometer used in our study.

temperature change. We define

$$\alpha = -\frac{1}{R_{th}}\frac{dR_{th}}{dT} \tag{3.1}$$

as the determining factor for thermometer's quality. Higher α values will yield a higher signal in the measurements, as will be explained in subsection 3.3.3.

α at low temperatures can be estimated by the ratio between the thermometer's resistances at room temperature and at liquid nitrogen $RR = \frac{R(77K)}{R(300K)}$. In order to achieve the best α at several Kelvin, the critical temperature of our superconductors, we aim to have an RR in the range $3.5 - 4.5$. This yields thermometers with common values of α in the range $0.03 - 0.3$ for the temperature span of interest. Experience shows that these RR values are achieved by 4/14 nitrogen to argon ratio in the gas mixture and a 275KHz

power source frequency.

Figure 3.7 shows an $R(T)$ curve of a NbN thermometer used in this study. Its resistance is several $K\Omega$ with a span of about $2K\Omega$ in our range of interest.

Separation from the bulk substrate

Figure 3.8: The same section of the calorimetric set-up as in Figure 3.6, taken from a different angle, after the separation of the CC from the bulk.

Another photo-lithography step is performed, which defines 12 $40\mu m$ thin legs that will support the active calorimetry cell. These legs carry the NbTi wires along them. An RIE process with SF6 gas is used to remove all of the silicon around the thinned part, leaving it thermally disconnected from the bulk. A sketch of the result can be seen in Figure 3.8.

To allow transport measurement of the thin film sample a bilayer of $5nm$ titanium and $25nm$ gold is deposited by using a mechanical mask on four additional legs. A sketch of the complete active sensor is shown in Figure 3.8, showing all the elements mentioned above.

3.3.2 Sample mounting

The sample is placed on a copper holder and its contacts are connected with a micro-bonder, as seen in Figure 3.10. In order to perform the quench condensation measurements, a mechanical mask is placed over the sample, covering all of the silicon die and the sample holder, except for a single

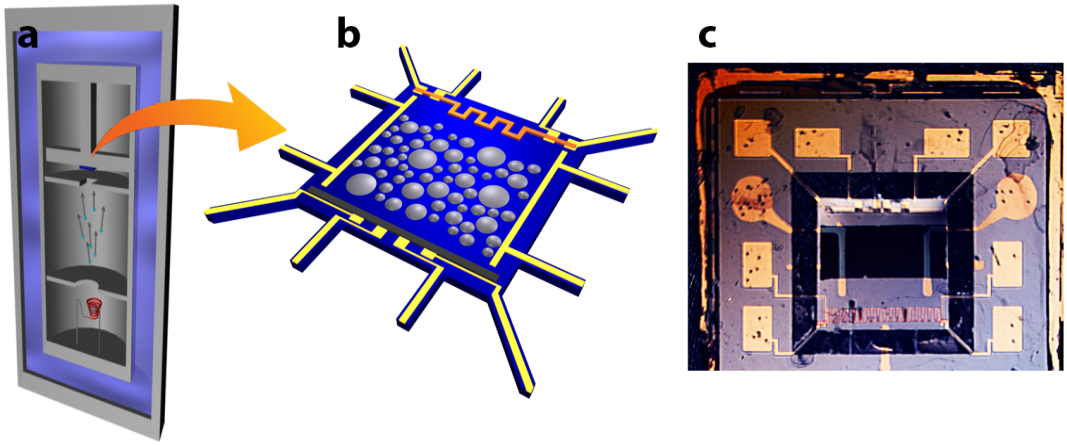

Figure 3.9: **a** A schematic view of the quench-condensation chamber submerged in liquid helium (light blue). The evaporation boat (red) is heated which causes the deposition material to evaporate (cyan balls) and condense on the sample (dark blue) which is located behind a mechanical mask. **b** A schematic view of the suspended membrane. It includes the leads (yellow), the heater (orange), the thermometer (dark grey) and the deposited film (light grey circles). **c** A used sensor. The thermometer is at the top of the suspended membrane, the heater is at the bottom, and the deposited film is the dark rectangle in between the two. The suspending silicon legs are barely visible.

window which exposes the two transport leads (see the deposited rectangle in Figure 3.9**c** and in the sketch in Figure 3.9**b**). The sample holder is then mounted on a probe supplied with three thermal evaporation sources loaded with Pb or Sn. This probe is fitted with a 1K-pot, which allows it to be cooled down to 1.4K. A sketch of the cryogenic deposition chamber is shown in Figure 3.9**a**.

3.3.3 Measurement protocol

An ac calorimetry technique which was developed by Sullivan and Seidel [63] is used to measure the heat capacity of the CC. In this technique the temperature of the CC is oscillated by applying an alternating current $I =$

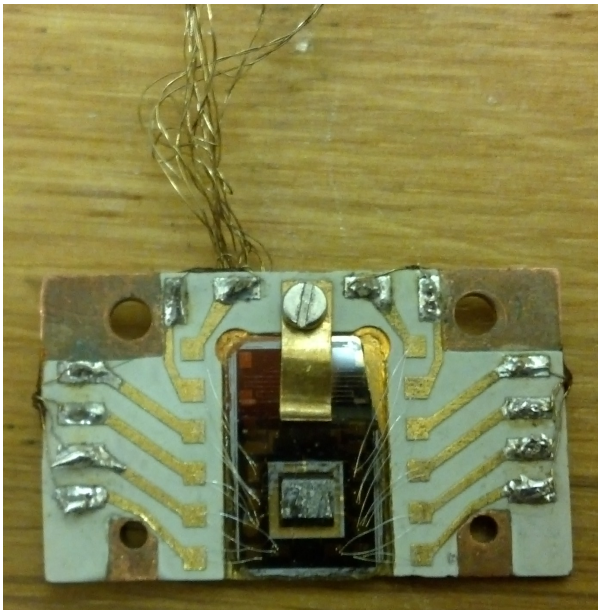

Figure 3.10: A used sample, the deposited Pb can be seen flaking on the active CC, bonded to the sample holder which is later placed in the quench-condensation chamber.

$I_0 sin\,(\omega t)$ to the heater. The power dissipated in the heater is therefore

$$P = RI^2 = P_0\,(1 - cos\,(2\omega t)) \tag{3.2}$$

with $P_0 = \frac{RI_0^2}{2}$. The ac term of the power therefore oscillates at the second harmonic of the applied current, which in turn oscillates the temperature of the cell at amplitude δT_{ac}. This 2ω signal from the thermometer is picked up by a lock-in.

Assuming good thermal anchoring of the heater and thermometer to the CC, the model system is reduced to the heating power, a relaxation time to the bath τ_b, a diffusion time of the heat throughout the CC τ_d and of course the heat capacity of the entire system C_p. These relate to the ac temperature oscillations by

$$\delta T_{ac} = \frac{P_0}{\omega C_p}\left[1 + \frac{1}{\omega^2\tau_b^2} + \omega^2\tau_d^2\right]^{-\frac{1}{2}} \tag{3.3}$$

The relaxation times in this equation act as a high-pass and low-pass

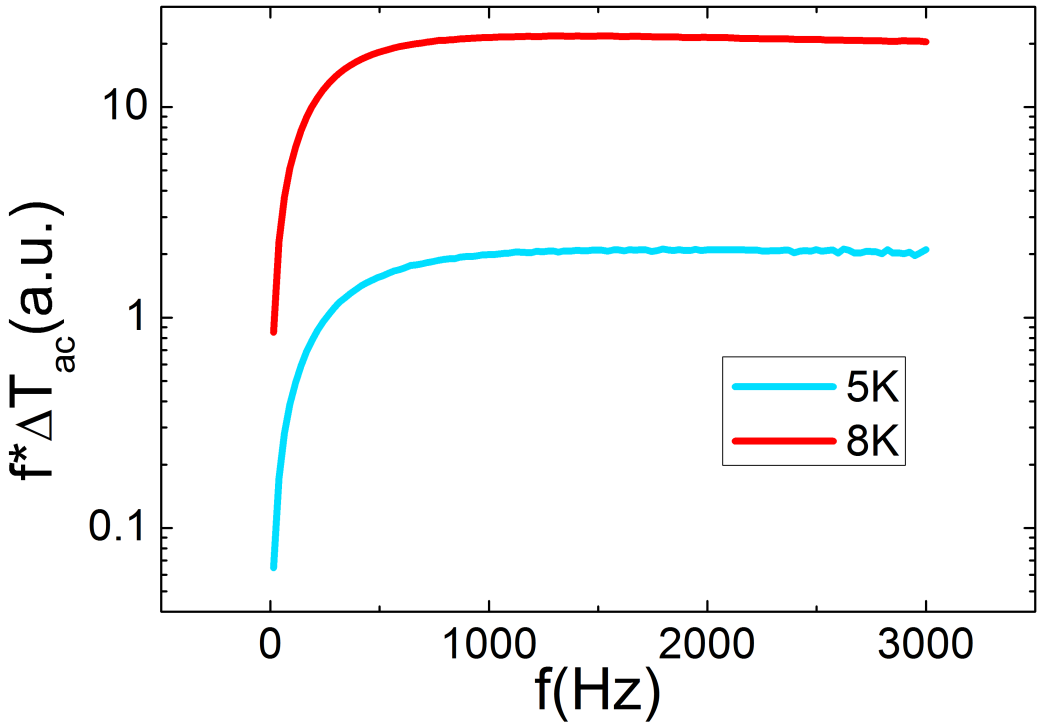

Figure 3.11: Measurement of the adiabatic plateau in different temperatures. The plateau is seen where $f_d \ll f \ll f_b$, which allows neglecting the limiting term in Equation 3.3.

filters for the temperature signal. In order to be able to extract C_p one must either measure them, or perform the measurement in a frequency range where the respective terms are negligible. The latter option is the one used in this work. The appropriate frequency is chosen by scanning the frequency range and choosing the maximum value measured for T_{ac} this way. This maximum may be broad, and is usually temperature-independent as can be seen in Figure 3.11. Neglecting these limiting terms one gets the formula for the heat capacity

$$C_p = \frac{P_0}{\omega \delta T_{ac}}. \tag{3.4}$$

P_0 is calculable from the resistance of the heater, which is constant in this temperature range, and the current driven through it. δT_{ac} is measured

by applying a small dc current I_{dc} through the thermometer and measuring the 2ω ac voltage that drops on it, V_{ac}. Each CC thermometer's resistance $R_{th}(T)$ is calibrated against another thermometer which is coupled to the sample holder, and is in turn calibrated to a Lake Shore Cernox thermometer. Through this calibration and the measurement of V_{ac} we can calculate

$$\delta T_{ac}(T) = \frac{V_{ac}(T)}{\alpha R_{th}(T) I_{dc}} \tag{3.5}$$

with α the temperature-dependent quality factor for the thermometer.

3.3.4 Sensor characterization

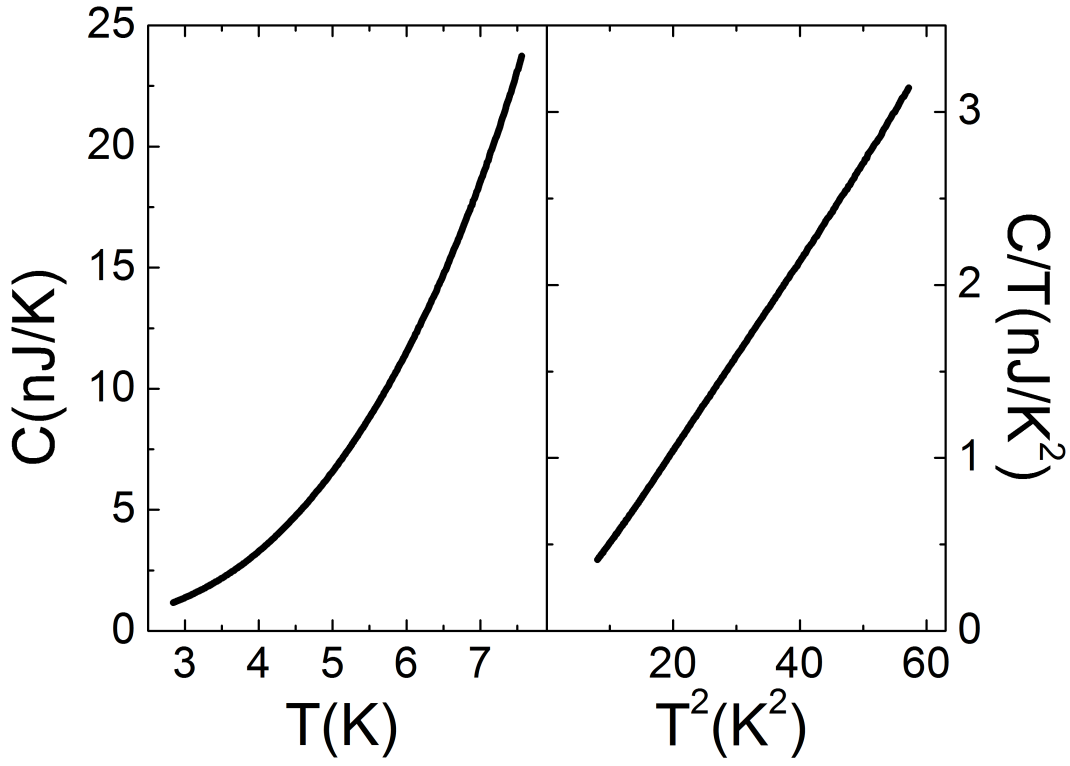

Figure 3.12: **left** Heat capacity of the bare substrate, leads, thermometer and heater of the CC used for the Pb sample. **right** the reduced form of the same heat capacity. The straight line stands for the classic 3D heat capacity of Equation 1.20.

For each CC before we begin measuring the heat capacity of the thin film we first measure the contribution of the bare substrate with the contacts, the heater and the thermometer. The result for the sensor used to measure the Pb sample is shown in the left panel of Figure 3.12. This measurement has a double purpose. First and foremost is the need to verify that the sensor indeed measures the heat capacity accurately. We check that the measured C(T) curve follows Equation 1.20, by plotting the reduced heat capacity $\frac{C_p}{T}$ versus T^2. This should result in a linear curve as is shown in the right panel of Figure 3.12. The second purpose of this measurement is to form a baseline which will later be subtracted from all following measurements. From this point onwards the reported heat capacity is that of thin films after the subtraction of this background.

3.3.5 Experimental process

After measuring the heat capacity of the bare substrate, we incrementally quench-condense thin layers of the superconducting metal onto the substrate. For each step the $C_p(T)$ and $R(T)$ curves are measured.

3.4 Magnetic force microscopy

In our work we use a commercially available set-up manufactured by Attocube. The sample is mounted on an XYZ scanner with scanning range up to 30μm laterally and up to 13μm of the Z axis when working in cryogenic temperatures. The scanner is mounted on a slip-stick piezoelectric crystal stack for rough positioning of the scanning area in front of the tip. The set-up is placed in a thermally isolated cylinder with a small amount of helium exchange gas and inserted into a variable temperature insert (VTI) which controls the temperature with one mK precision down to temperatures of 1.5K. The Dewar in which the VTI resides is hung on springs to dampen mechanical noise. It is fitted with a superconducting magnet that can provide field of up to 9T.

The tips used in this work are products of Veeco Instruments. Magnetic

tips are the MESP model, with cobalt plating acting as the magnetic supplement to the Si tips. Some measurements were performed with an electrically conducting tips, those are the SCM-PIC model with 20nm of platinum iridium as the conducting layer.

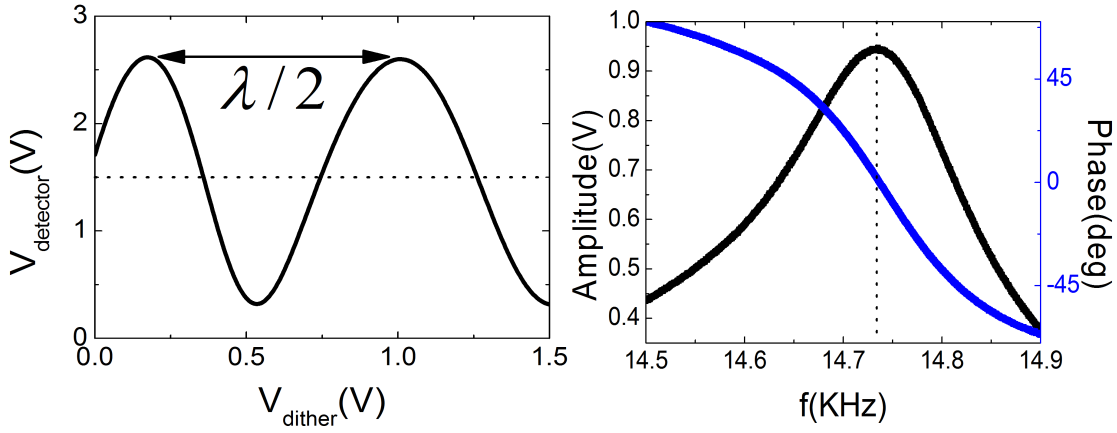

Figure 3.13: **left** Interference pattern when changing the cantilever-fibre distance by applying a dc voltage to the dither piezo. The dotted line is the working point used for non-contact microscopy. **right** Amplitude and phase of the cantilever oscillations as a function of the excitation frequency for a Veeco SCM-PIC tip. The dotted line is the resonant frequency, which is used as the excitation frequency.

The cantilever is aligned in front of an optical fibre ferrule. A laser is split to two different paths, one of which is through this fibre, and reflected from the cantilever. The two different paths are then recombined, and the resultant beam is directed at a photo-detector. The output of the photo-diode is a function of the distance the laser travels to and from the cantilever as seen in Figure 3.13. This allows a highly sensitive measurement of the position of the cantilever within a half-wavelength interval. The laser is provided by a ThorLabs PRO800 WDM source. Its wavelength is $\lambda = 1538.98$nm.

A piezoelectric crystal, the dither-piezo, is mechanically coupled to the tip. It is used both as an exciter for the tip's oscillations and to control the cantilever-fibre distance with a dc voltage applied to it. The ideal cantilever-fibre distance for non-contact measurements is at the mid point between

constructive and destructive interference, where a slight change in cantilever position causes the largest change in measured intensity. A proportional-integral (PI) feedback loop keeps the cantilever at this correct position during the entire measurement. The dither-piezo is supplied with an ac voltage which oscillates the tip at a given frequency f, and the voltage oscillations that result on the photo-detector are picked up by a lock-in amplifier. In order to measure the resonance frequency of the tip f_0 a chirp is sent through the cantilever. The result is shown in Figure 3.13, where the resonance peak is clearly visible. Alongside its amplitude, the phase ϕ between the excitation oscillator and the measured oscillations is recorded.

When the tip approaches the sample's surface, any height-dependent force exerted on it will change its resonant frequency. Modelling the cantilever as a mass-loaded spring, one classically obtains the relation

$$2\pi f_0' = \sqrt{\frac{k_e}{m_e}} \tag{3.6}$$

with $k_e = k_0 - \frac{\partial F_z}{\partial z}$ an effective spring constant of the cantilever including the free spring constant k_0 and the external force gradient $\frac{\partial F_z}{\partial z}$, and m_e an effective mass loaded on the spring. When $\frac{\partial F_z}{\partial z} \ll k_e$ one can use a Taylor expansion for the right hand side and get

$$\frac{\partial F_z}{\partial z} = -\frac{2k}{f_0}\Delta f \tag{3.7}$$

Measurement of $\frac{\partial F_z}{\partial z}$ is performed by measuring Δf in one of two manners. The first is by measuring the change in phase ϕ. This phase behaves as

$$\phi = \arctan\left[\frac{f f_0}{Q\left(f_0^2 - f^2\right)}\right] \tag{3.8}$$

with Q the Q-factor of the cantilever's oscillation. This equation is approximately linear around $f \approx f_0$, one of the inflection points of the arctangent, as can be seen in a calibration measurement given in Figure 3.13. The second method is by using a PI loop which locks ϕ to a constant value by continually changing the excitation frequency to the altered resonant frequency f_0' and recording the change Δf. The two give almost identical results in our

measurements and thus we report them in either degrees (first method) or Hz (second method) interchangeably.

The force we strive to measure in this work is the magnetic force. A problem which may arise in the process is the fact that the tip feels forces other than the magnetic. Two other forces that the magnetic tip is bound to feel are the van der Waals force and the electrostatic force. The first is a short-range force which decays quickly within a few nanometers from the surface, in contrast to the electric and magnetic forces which are long-range, therefore cancelling out this force in our measurements is done by measuring at a tip-sample distance of $d > 30$nm.

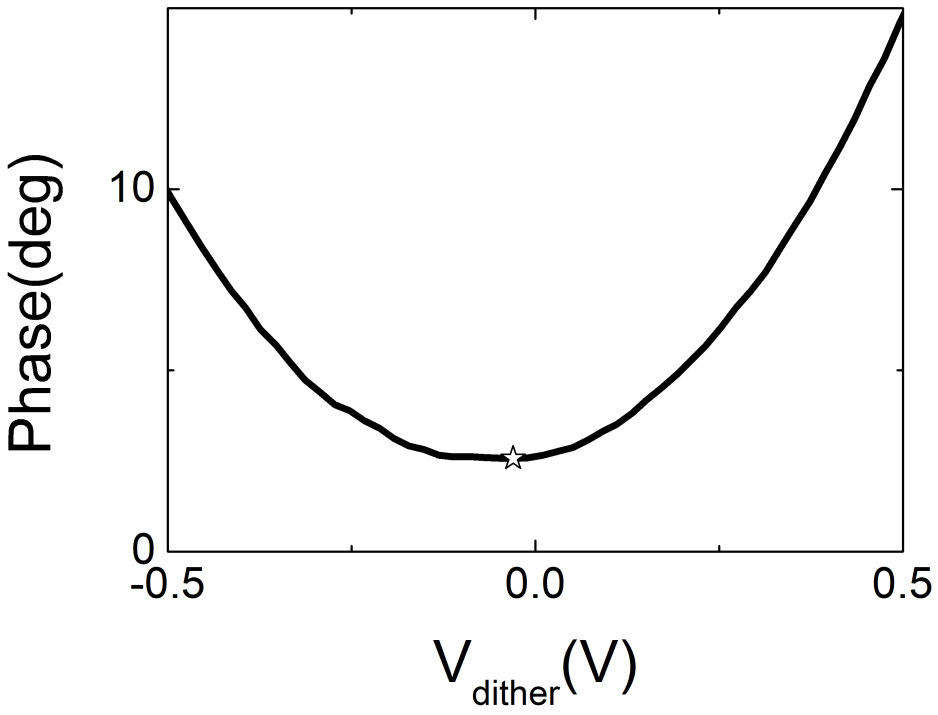

Figure 3.14: Cantilever oscillation phase versus voltage applied between the tip and the surface. Minimum is observed in this case at -30mV, marked by a star.

However, the electrostatic force is long-range. It may arise due to charging effects, differences in material's work function, capacitance and so forth. This

force is always proportional to the voltage difference ΔV between the tip and the sample by

$$F_E = \frac{1}{2}\frac{dC}{dZ}\Delta V^2 - E_z C \Delta V \tag{3.9}$$

with C the capacitance between the tip and the surface and E_z the z-component of the electric field. Its cancellation is achieved by applying an external voltage bias between the two. A phase versus voltage curve is shown in Figure 3.14, which shows a distinct minimum where the electric forces are cancelled out. Unfortunately, this method does not allow an ideal force correction in a case where the electric field above the surface is inhomogeneous.

Two different modes of measurement are reported in this study, each allowing the dissection of the volume above the sample's surface in a different manner. Upon approaching the surface the tip is expected to sense the Meissner repulsion, which will grow steadily and monotonously with approaching the surface. For a point dipole distanced above a perfectly superconducting infinite plane the force follows the formula [64]

$$F_z = \frac{3\mu_0 m^2}{32\pi \left(z + \lambda_L\right)^4} \tag{3.10}$$

with m the tip's dipole strength and μ_0 the vacuum permeability. The finite size of the tip and the shape of the superconductor can be incorporated as small perturbations for this formula. The first mode of operation is the measurement of the force derivative while approaching the surface in the z direction. The second mode is a lateral scanning of the force derivative. That is, scanning in the $x-y$ directions to allow a map to be extracted, such as the one in Figure 1.16. By scanning vortices one may calculate the penetration depth by fitting to the magnetic field profile expected from a single vortex [65]

$$\vec{B}\left[\vec{R}, z\right] \approx \frac{\phi_0}{2\pi} \frac{\vec{R} + \left(z + \lambda_L\right)\hat{z}}{\left(R^2 + \left(z + \lambda_L\right)^2\right)^{\frac{3}{2}}} \tag{3.11}$$

with $\vec{R}$ the lateral distance from the vortex centre.

3.5 Proximity effect

In this experiment we measure the effect that a metallic layer, i.e. gold, deposited on top of an a-InO film has on the bi-layer's transport properties. The metallic layer is quench-condensed on the film, first ultra-thin and incrementally thicker, slowly increasing the metal's mean free path with its thickness. This translates into a change of length scale of the superconducting proximity effect in the superconductor and the metal.

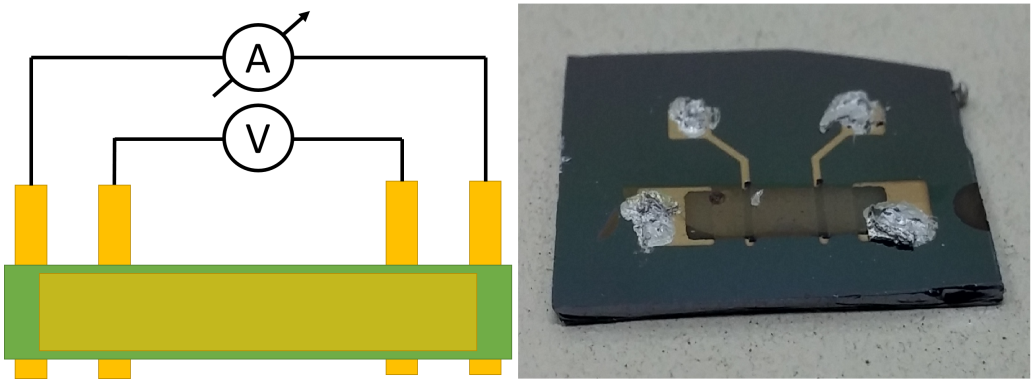

Figure 3.15: **left** Sketch of the four-probe circuit used to measure the resistance of a-InO films. The yellow legs are gold leads, the green slab represents the a-InO film and the translucent yellow in its middle is where the gold is quench-condensed during the experiment. **right** A used sample. The grey blobs are silver paint drops used to connect the wiring to the sample.

A four-probe configuration of gold leads is deposited on an insulating silicon oxide substrate using a mechanical mask. 30nm of a-InO is deposited between the four probes, each sample with a different partial pressure of oxygen in the evaporation chamber, which leads to a different level of disorder. A mechanical mask is placed on top of the sample, with a window open in front of the a-InO slab, and mounted on a ^{3}He UHV cryostat capable of reaching $250mK$. The sample is in the line of sight of thermal evaporation boats loaded with gold granules. A schematic sketch and a photo of a sample are shown in Figure 3.15.

The resistance of the a-InO sample is measured over the temperature range $0.25 - 10K$. Sequential evaporations of ultra-thin gold films are con-

ducted at cryogenic temperatures by the quench-condensation set-up. After each incremental layer the sample's $R(T)$ is measured again. This process is repeated until the normal-state resistance of the sample is reduced considerably.

Chapter 4

Results and discussion

4.1 Specific heat

Two different samples, both spanning the SIT from the insulating side to the superconducting side, were measured in our study. The first was a Pb sample with 18 consecutive depositions, and the second was Sn with 35 depositions. As will be shown, both samples show qualitatively similar results.

Figure 4.1 shows the resistance and the heat capacity of the thickest Pb film we measured. The $R(T)$ curve shows a sharp transition, approximately 30mK wide, from the normal state to the zero-resistance superconducting state at $T_c = 7.2$K, which is the bulk critical temperature. We can therefore consider this film to be a bulk specimen. Indeed, its heat capacity shows a sharp jump that is about 30mK wide at the same T_c. This jump is characteristic of a second-order phase transition.

Figure 4.2 shows the reduced heat capacity of the thinnest Pb film we measured versus T^2. The sheet resistance of this film was immeasurably high at low temperatures, and at 8K it was about $1G\Omega$. The curve is seen to be linear for most of the temperature range, excluding a region close to $50K^2$, which corresponds to about $T = 7.1$K, close to the bulk T_c. At this point a deviation is seen from the straight line.

This deviation is in fact the transition jump we see for the thickest film, except for the fact that it is smeared, just as the curves for the smaller

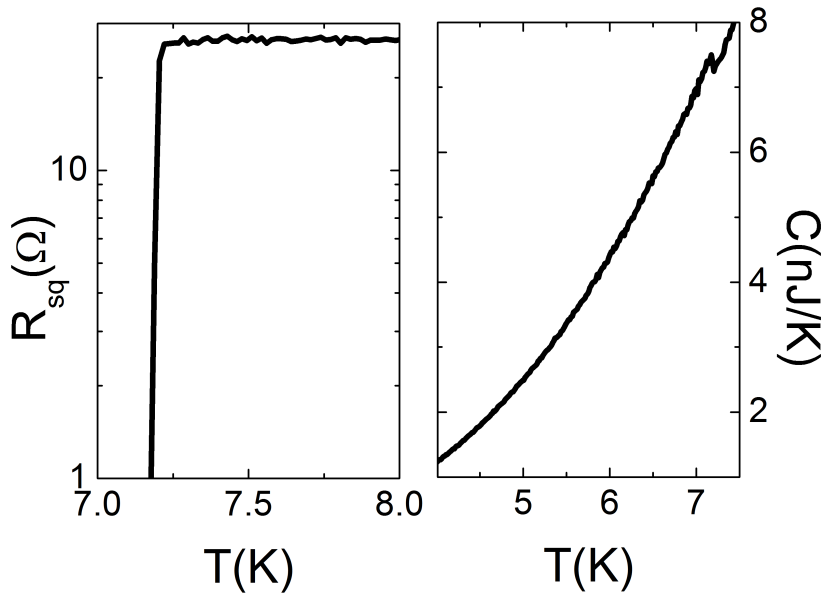

Figure 4.1: **left** $R(T)$ curve for the thickest Pb film. **right** heat capacity C_p versus temperature for the same film.

grains of Sn are smeared in Figure 1.15. Interestingly this signature of the superconducting transition occurs both in superconducting and insulating films at practically the same temperature.

The full evolution of the transition with the film's thickness is depicted in Figure 4.3, showing the heat capacity for all of the Pb depositions alongside their $R(T)$ curves. The $R(T)$ curves show the classic granular SIT [21] as was illustrated in Figure 1.4, including the insulating state with diverging resistance, the intermediate stages of re-entrant behaviour, long exponential tails, and the sharp superconducting transition.

All of the $C_p(T)$ curves show similar features: they form a straight line at low temperatures. They all deviate from that straight line at temperatures close to the bulk T_c, and later approach another straight line. This deviation, which we address as the specific heat jump ΔC_p, becomes sharper and larger with greater film thickness.

When comparing the $R(T)$ curves with their corresponding $C_p(T)$ curves in Figure 4.3, a striking difference emerges that should be addressed: The SIT is not directly observed in the heat capacity curves. While the SIT

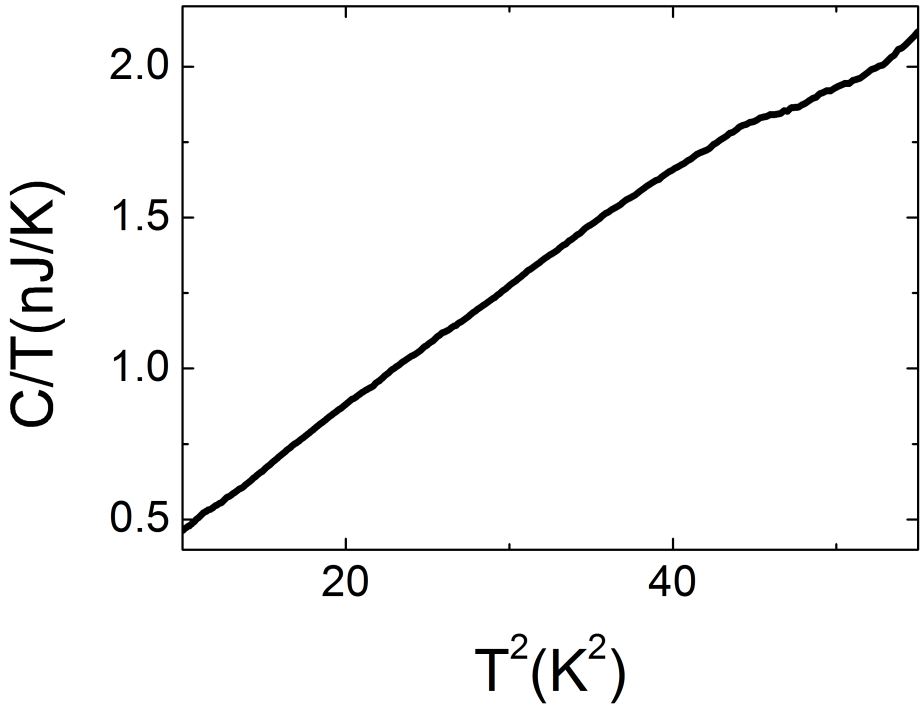

Figure 4.2: Reduced heat capacity $\frac{C_p}{T}$ versus T^2 for the thinnest Pb film we measured. Its resistance was immeasurable with our set-up.

is well-defined in the resistance curves that can easily be divided into the insulating and superconducting cases at $T = 0$K, it is impossible to tell what is the current state of the system just by looking at the specific heat.

The heat capacity curves, along with the jumps at T_c, evolve smoothly all the way from the insulating state to the bulk superconductor. This is due to the fact that the specific heat is not sensitive whatsoever to the percolation of superconductivity through the film. However, it is most sensitive to the forming of Cooper pairs, that in this experiment always occurs in the bulk T_c. At this temperature, the entropy behaviour versus temperature changes abruptly, and so the transition stands out above the normal-state $C_p(T)$ baseline.

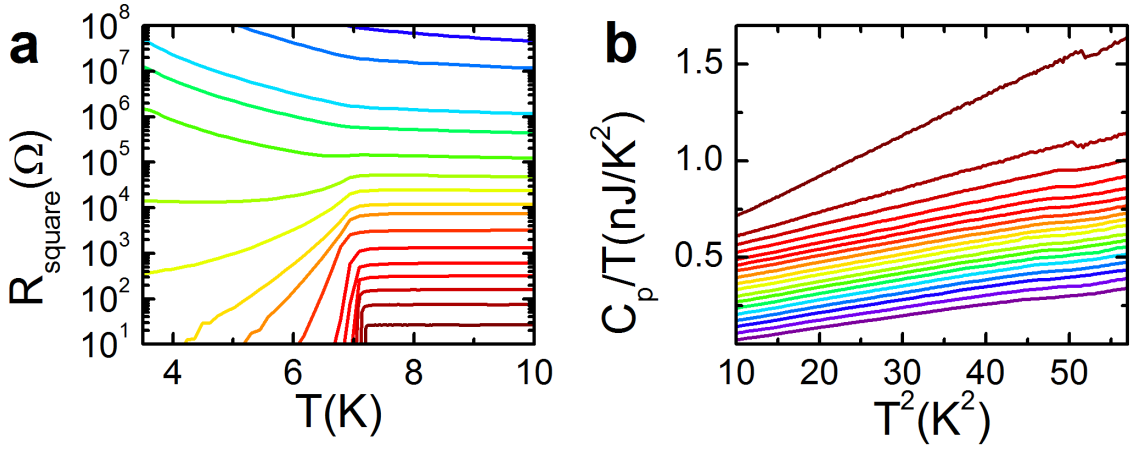

Figure 4.3: **a** $R(T)$ curves for the set of Pb thin films, showing the transition from the insulator for the thinnest films (violet to cyan) to the superconductor for the thickest ones (red to brown). The intermediate states of re-entrance (green curves) and exponential tails (yellow to orange) are also seen. **b** reduced heat capacity $\frac{C_p}{T}$ versus T^2 for the same films as the left panel. The curves are shifted in the y-axis for clarity.

Heat capacity of all films shows a clear

$$\frac{C_p}{T} = \alpha + \beta T^2. \tag{4.1}$$

behaviour for almost all temperatures. As was discussed in section 1.5, this is the heat capacity that is expected for the normal-state electronic and phonon part of the material. Figure 4.4 shows linear extrapolations of the reduced heat capacity versus T^2, according to the behaviour expected from Equation 4.1, for the thickest and thinnest films. We use these extrapolations as a baseline, and subtract it from the original $\frac{C_p}{T}(T^2)$ curves. We repeat this process for all of the different stages. This allows us to zoom in on the characteristics of the transition close to T_c, where the curve deviates from that baseline.

To validate our fits, we plot β of Equation 4.1 as extracted from fits to the $\frac{C_p}{T}$ curves below T_c versus the film's thickness. It is expected to show a linear dependence. Indeed, this is the case as can be seen in Figure 4.5. An

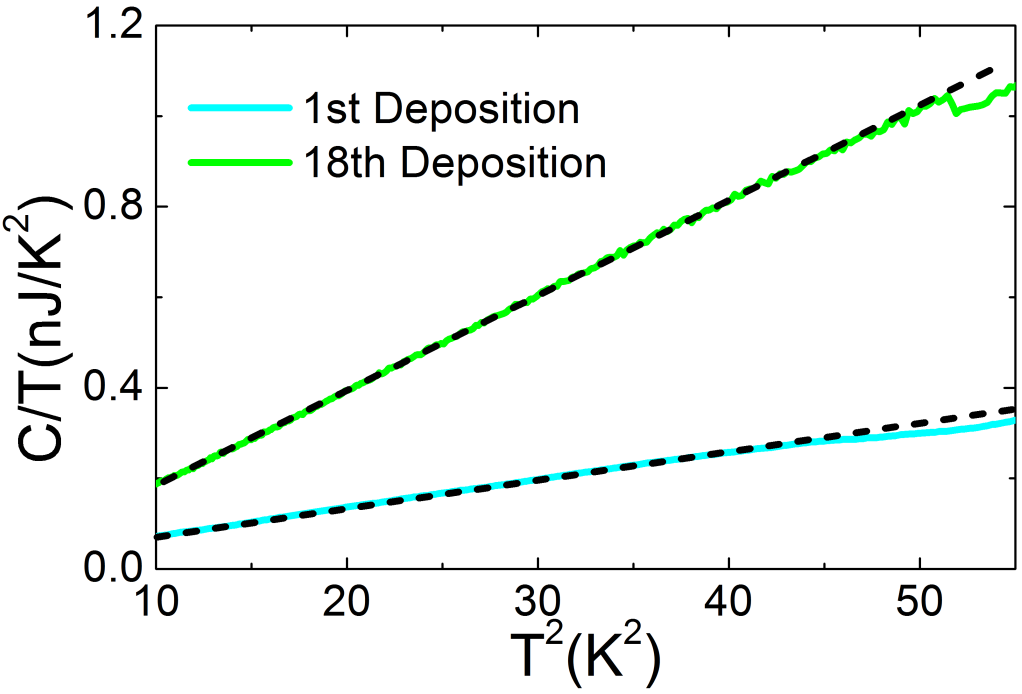

Figure 4.4: $\frac{C_p}{T}$ versus T^2 for the first and last depositions. The dashed lines are a guide to the eye that emphasizes the deviation from the normal-state heat capacity seen even in the thinnest film.

intercept very close to $\beta = 0$ for $t = 0$ affirms our calculations as well.

Several curves of the superconducting heat capacity after the subtraction of the film's phonon background are shown in Figure 4.6. The similarities between the curves are obvious. For example, all of them show a clear transition from zero to some finite value, and this transition occurs roughly at the same temperature.

We define three important quantities that emerge from these curves. One is the transition temperature T_c, another is the transition width ΔT and last is the size of the specific heat jump Δc. We shall now present the different quantities as a function of film thickness and discuss the significance of these findings.

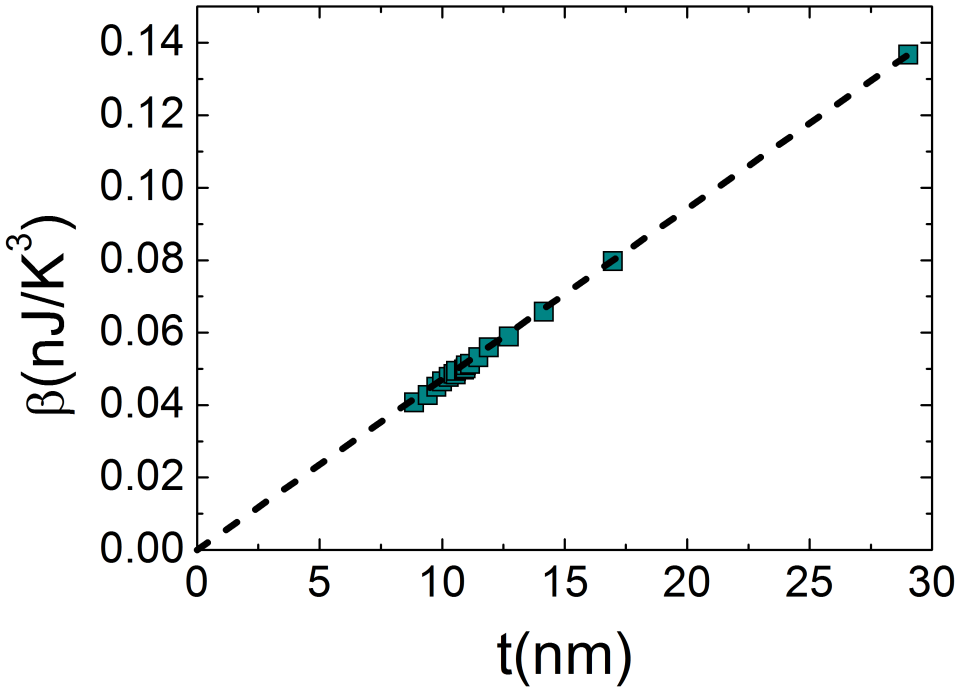

Figure 4.5: β for lines of the form $\alpha T + \beta T^3$ fitted to the different curves in Figure 4.3. The dashed line is a guide to the eye, emphasizing the linearity between the two quantities and the zero intercept for $t = 0$.

4.1.1 Transition temperature

We define the critical temperature, T_c, of the transition observed by the heat capacity measurements as the temperature that corresponds to the middle of the heat capacity jump. T_c is showed in Figure 4.7 as a function of film thickness.

For the thickest films, the critical temperature is similar to that of bulk samples, which is marked by a dotted line. The plot shows that a slight decrease, less than 5 percent, is observed for the thinnest films.

We see therefore that T_c is rather constant for the entire transition, and is in the insulating regime very similar to the T_c seen at the superconducting transition.

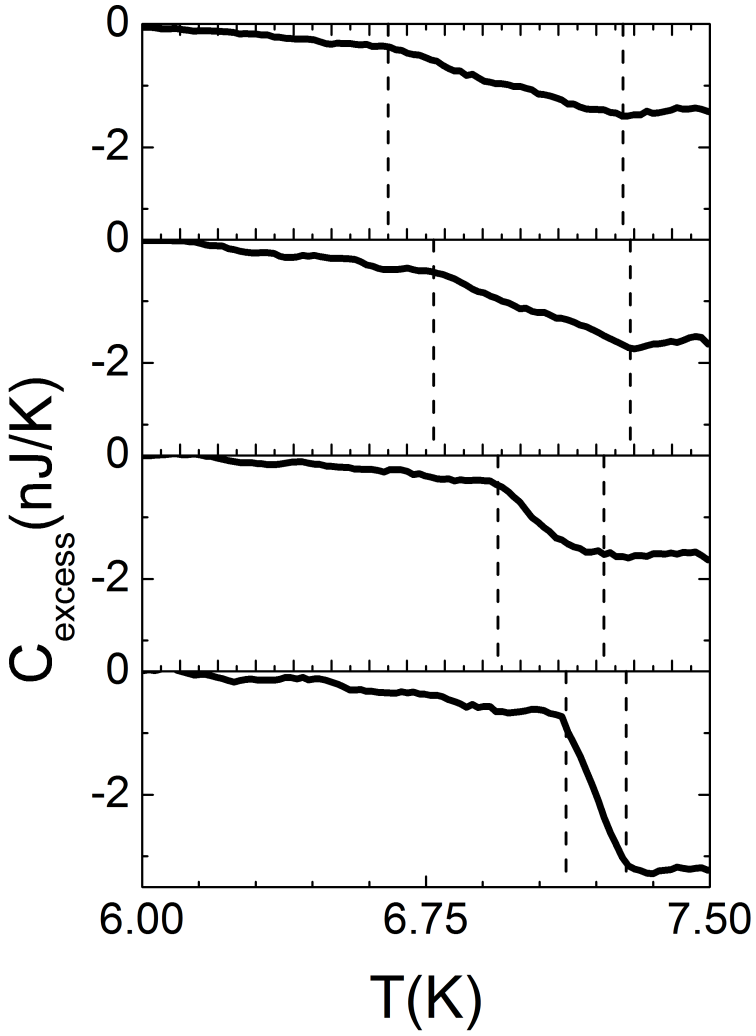

Figure 4.6: Superconducting heat capacity of Pb depositions number 1, 6, 15, and 18, from top to bottom. These were obtained by subtracting straight lines similar to those in Figure 4.4 from each curve. The dashed lines correspond to the onset and end of the transition, marking its width.

The notion of superconductivity in the insulating regime of the SIT, with the localized charge carriers being Cooper pairs as in the bosonic model, is not new and can be seen in previous experiments as was discussed in section 1.3.2. However our results, to the extent of our knowledge, are the first true thermodynamic evidence for superconductivity with bulk T_c in an insulator.

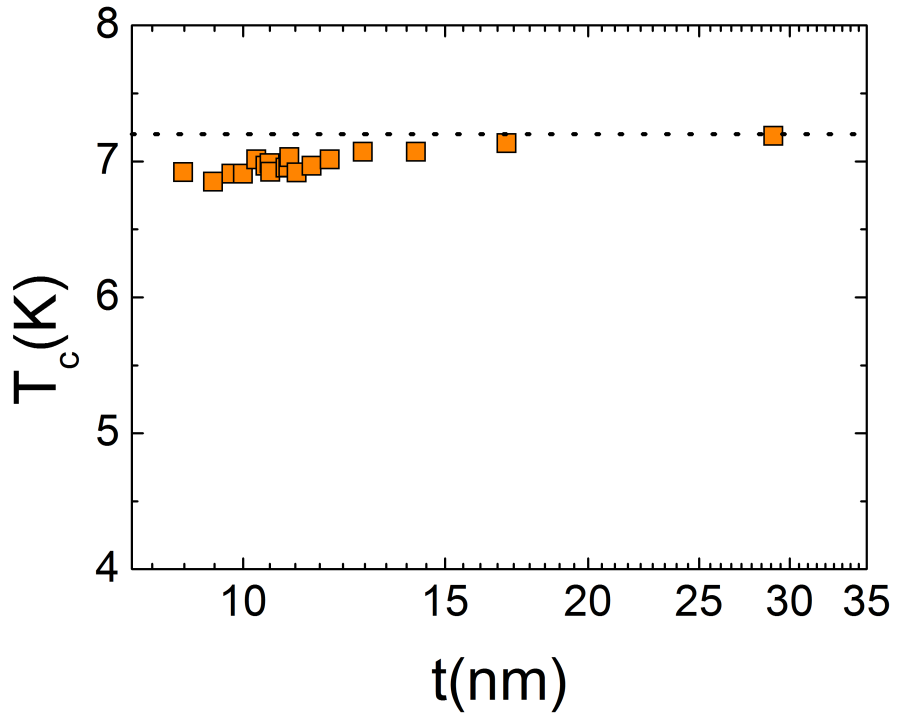

Figure 4.7: T_c, the middle of the sharp jump in c_p, as a function of thickness for the Pb sample. Dotted line is the bulk value $T_c = 7.2K$.

As was discussed before, unlike all transport and tunnelling measurements, this heat capacity singularity does not depend on the specifics of percolation paths and the quenched inhomogeneity of the measured system. The fact that a clear transition is seen around bulk T_c confirms that superconductivity is *global* in the measured films and appears in all of the grains, rather than just a small portion of the grains turning superconducting. This will be further elaborated upon in section 4.1.3.

4.1.2 Transition width

The width of the transition, ΔT, is marked between two dashed lines in Figure 4.6. It can be seen that the transition becomes narrower as the thickness is increased. We plot this transition width as a function of film thickness in

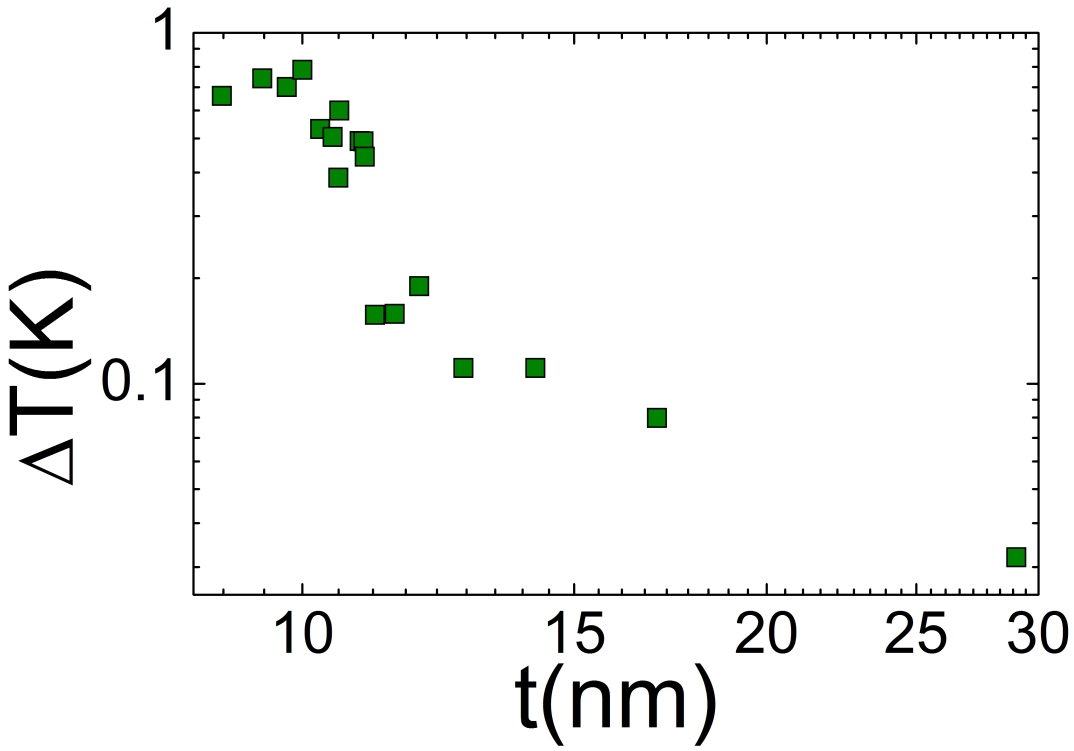

Figure 4.8: ΔT, the width of the transition seen in C_p, as a function of thickness for the Pb sample.

Figure 4.8. The transition for the thickest film is of the order of our measurement resolution, which is limited by $\delta T_{ac} \approx 25mK$. For the thinnest films this width is increased up to about 0.8 Kelvin.

The behaviour of ΔT, where the width increases with the reduction of film thickness, corresponds nicely with the reduction in dimensionality. Both in 2D and in 0D superconductors, the transition is expected to smear out. Arguably, thin granular films lay in between the two as they are composed of a 2D array of 0D superconductors.

Fluctuation effects allow the heat capacity to start and rise above the bulk T_c, and causes it to slowly approach the appropriate value below T_c. It is therefore not surprising to see this behaviour in our film.

In addition, as was noted in subsection 1.5.3, the constant electron number may play a role in smearing the superconducting transition. In our system

the grains in insulating films are disconnected from one another, and become gradually interconnected with the addition of more layers of material. This makes the electron number in each grain less determinable, and therefore we may expect this smearing to be reduced gradually for thicker films - as is indeed observed.

4.1.3 Heat capacitance jump

The heat capacity jump ΔC_p is an extrinsic quantity. This means that its value is linear in the mass m of the measured system

$$\Delta C_p = m\Delta c_p \tag{4.2}$$

where c_p is the specific heat, and Δc_p stands for the specific heat jump. One can divide the superconducting heat capacity by the nominal mass of each film. This leaves us with the superconducting specific heat c_{sc}. The specific heat jump Δc_p of the transition was measured previously for bulk superconductors and is expected to be $107\frac{\mu J}{gK}$ for Sn[66] and $280\frac{\mu J}{gK}$ for Pb[67].

The jump amplitude of our films behaves non-trivially. One would naïvely expect that if superconductivity is observed in all grains even on the insulating side, then the heat capacitance jump will be constant across the SIT. If some of the grains do not hold superconductivity, e.g. due to the Anderson criterion (see section 1.5.3), then the heat capacitance will be effectively smaller, since we calculate Δc by dividing the measured ΔC by the *nominal* mass, which includes the non-superconducting grains.

Figure 4.9 shows that neither of these two cases are observed, but rather the heat capacitance rises with the reduction of thickness down to d_c, the thickness where the SIT is observed via $R(T)$ measurements, that is marked with vertical dashed lines. Below d_c, Δc is suppressed down to the edge of our measurement capabilities. Δc therefore forms a peak around the SIT. At its maximum, Δc_p for lead reaches $484\frac{\mu J}{gK}$, and for tin it reaches $220\frac{\mu J}{gK}$, both values exceed that of the bulk considerably.

This anomalous Δc behaviour is very surprising, and has to be addressed. Unfortunately for the case of small superconducting grains with Josephson

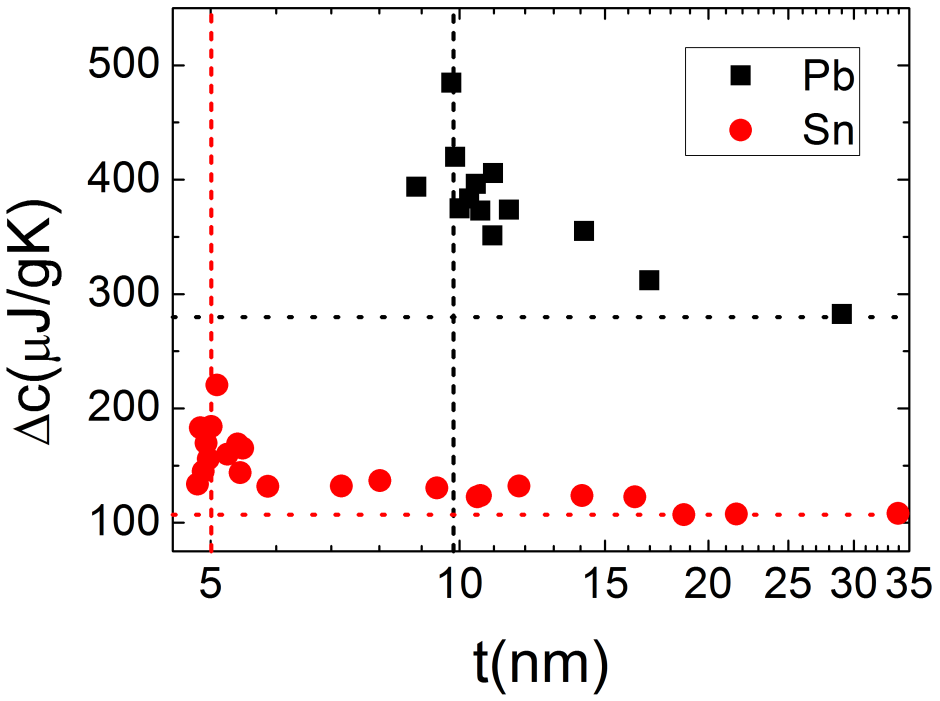

Figure 4.9: Δc_p, the specific heat jump, as a function of thickness for the Pb and Sn films. Horizontal dashed lines stand for the bulk values. Vertical dashed lines are the critical thickness values, where the SIT is observed by transport measurements.

coupling between them, there are to the extent of our knowledge no published theoretical predictions regarding the behaviour of the heat capacity, and no notable experiments have been conducted on the subject. This makes the analysis of our results rather difficult.

We try, however, to explain it in two manners: BKT transition and QPT.

BKT transition

There is a straightforward mapping between the phases of coupled grains and the discrete sites we consider in the XY model. This may guide us in the understanding of heat capacity of granular superconductors, remembering that inherent in the XY model is the BKT transition. This transition may

occur close to T_c and therefore the transition's heat capacity is added to our results.

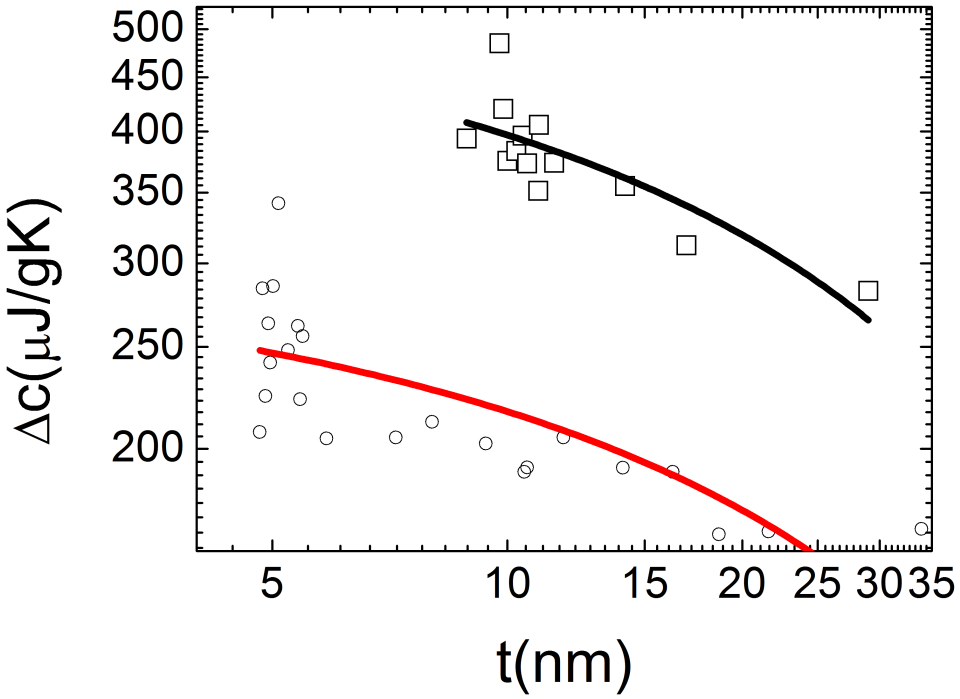

Figure 4.10: The Pb (squares) and Sn (circles) datasets from Figure 4.9, accompanied by a least-squares fits to Equation 1.27.

We therefore turn to Ovchinikov and Varlamov's theory, discussed in section 1.5.2, regarding the BKT transition in thin films.

In the scope of their work, the heat capacity due to fluctuations close to T_c behaves with film thickness t as $A + B\sqrt{t}$. Fitting our data to this theory yields the curves shown in Figure 4.10.

The fitted curves seem to fit our data for high values of t. However, one can notice that the theory does not comply with the data at lower thickness. While a certain correspondence might be seen for the Pb sample, the suggested function does not fit well with the data.

Two main things stand out that show the inability of this theory to fit our data. For one, the square-root of thickness cannot not capture the approach

to bulk values for thicker samples, as a $\sqrt{t}$ term diverges with $t \to \infty$. Another blow is the absence of a peak. The square-root term is monotonous for all $t \geq 0$, and cannot form a peak for any A and B chosen.

QPT

Remembering that the SIT is a model manifestation of a QPT, one should ask how would the heat capacity behave near such transitions. The scaling parameter for the different thermodynamic quantities near a transition should be universal, just as all thermodynamic quantities behave as a power law of $\tau = 1 - \frac{T}{T_c}$ near classical phase transitions. Similarly, close to a QPT they should scale with

$$x = \frac{g - g_c}{g_c T^{\frac{1}{\nu z}}}. \tag{4.3}$$

where the tuning parameter g is the film thickness d for our case of the SIT [34].

We normalize the data from Figure 4.9 by the bulk value of the jump and plot it versus the proposed scaling parameter, x. We take $z = 1$ and $\nu = 0.67$, which are the appropriate values for the XY model [68], [69]. The results are shown in Figure 4.11 on a log-log scale.

Using the guides to the eyes in the plot, we see that for small values of $d - d_c$, up to $x = 0.05$ for the Pb film and up to $x = 0.1$ for the Sn film, the data points are nearly aligned on a straight line. This means that for this range the excess heat capacity behaves as a power law with the scaling parameter

$$c_p = c_0 x^{-\eta}. \tag{4.4}$$

Using a least-squares fit, we find that $\eta = 0.209 \pm 0.092$ for the Pb films and $\eta = 0.278 \pm 0.039$ for the Sn films, leading to the estimated form

$$c_p = c_0 \left(\frac{g - g_c}{g_c T^{\frac{1}{\nu z}}} \right)^{-0.245}. \tag{4.5}$$

The two values are quite close to one another, and overlap when including the fit error. This serves as another reinforcement for the SIT being a universal

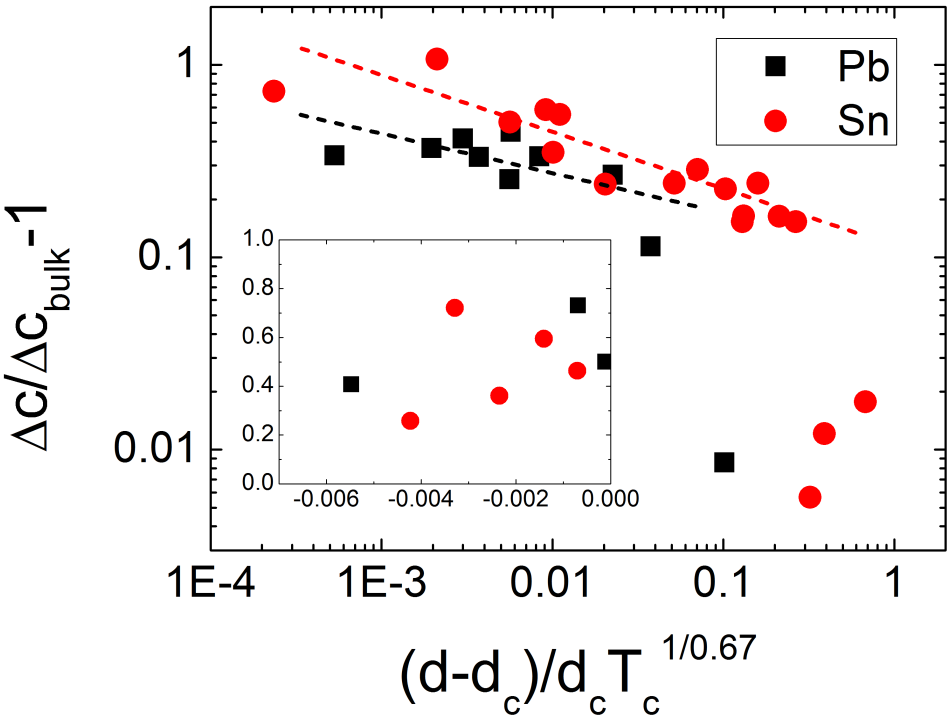

Figure 4.11: Excess specific heat jump in the superconducting transition, normalized by the bulk value, versus $\frac{d-d_c}{d_c T_c^{\frac{1}{0.67}}}$, the distance from the quantum phase transition, for $d > d_c$. The dashed lines are guides to the eye. Inset: the same quantities as the main figure, shown in the range $d < d_c$.

phenomenon, since the particular differences between Pb and Sn do not seem to affect it critical values.

For the range of $d < d_c$, seen in the inset of Figure 4.11, unfortunately only a small amount of points is available. In addition, the extremely small mass of the film makes the scatter noise large, and any attempt to fit them to a power law yields values with extremely large error. For example, an attempted least-squares fit yields $\eta = 0.057 \pm 0.14$ for the Pb film and $\eta = 0.17 \pm 0.31$ for the Sn film.

Our experimental results currently lack the theoretical work to support it and to try and explain where the values of η spring from. We have received private communications supporting the formation of a heat capacity peak at

the superconducting transition [70]. The reason for this peak is the mechanism of bosonic collective modes, those are the Higgs and Goldstone modes. In a bulk superconductor these modes are damped and are barely observable, however close to a quantum critical point the modes are systained for longer times and thus they play a role in the thermodynamics of the system.

This theory agrees well with a recently published paper. The authors claim to have seen collective modes in spectroscopy measurements [71]. According to this paper, the gap of the Higgs collective mode is diminished close to the SIT, and as it becomes smaller than the superconducting gap it absorbs terahertz radiation with energy lower than the superconducting gap.

To summarize, we see clear indications for a peak in c_p near a quantum phase transition that follows the appropriate scaling. We have extracted the critical exponents near this transition, and expect a rigorous theoretical explanation for our results will be found soon.

4.2 Magnetic force microscopy

The MFM measurements were conducted on an a-InO sample which is on the superconducting side of the SIT. Its $R(T)$ and magneto-resistance, both taken inside the MFM chamber, are shown in Figure 4.12. In the $R(T)$ curve we see the usual resistance drop, with $T_c \approx 3$K. In the $R(H)$ curve we see the rise of the resistance towards the magneto-resistance peak. Both curves are typical of the material at hand.

A cornucopia of different structures is revealed when scanning the tip laterally above the sample. The vast majority of them can be reduced to a set of multi poles: monopoles, dipoles and quadrupoles. Figure 4.13 shows three samples of these cases of isolated structures.

All of the pole structures have shown no observable dependence on temperature and external magnetic field. Figure 4.14 shows two images taken at 3K and 8K, both showing the same picture other than the noise that is attributed to the measurement rather than the sample.

Since these structures are indifferent to temperatures far beyond T_c, we must assume that they are not related to superconductivity. We attribute

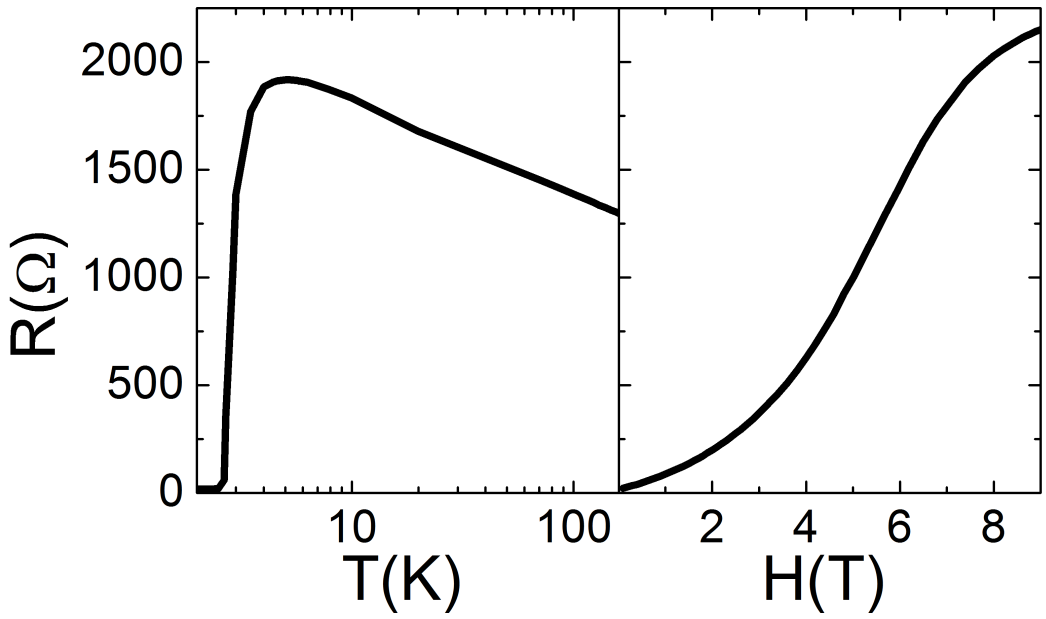

Figure 4.12: **left** $R(T)$ and **right** magneto-resistance taken at $T = 2K$ of the a-InO film.

these structures to localization regions, that are formed due to Anderson localization. These regions hold a large amount of electrons, compared to the region around them that is rather depleted from electrons. Therefore, these sites appear as very strong electric field sources.

As was discussed in section 3.4, it is possible to cancel out an electric force if the field is homogeneous. In this case the high inhomogeneity of the electric field near the localization sites does not allow us to do so by simply applying a constant voltage bias. Since these forces dominate over the magnetic forces, we turn to other means to measure them.

The tool we use is $\frac{\partial F_z}{\partial z}(z)$ curves. We call these force-distance curves for simplicity. Measuring these curves allows us to take different profiles at the same point, and look for small changes in the curves at different temperatures and magnetic fields, that will occur due to the change in superconducting properties.

Naïvely, assuming homogeneity of the superconducting condensate in the film, we would expect these curves to follow the Meissner repulsion given in

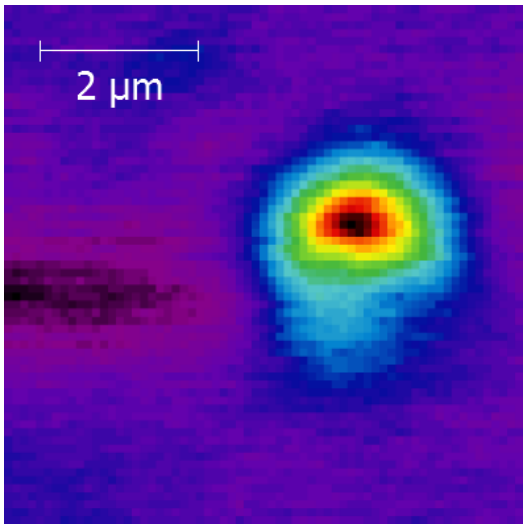

(a) Monopole

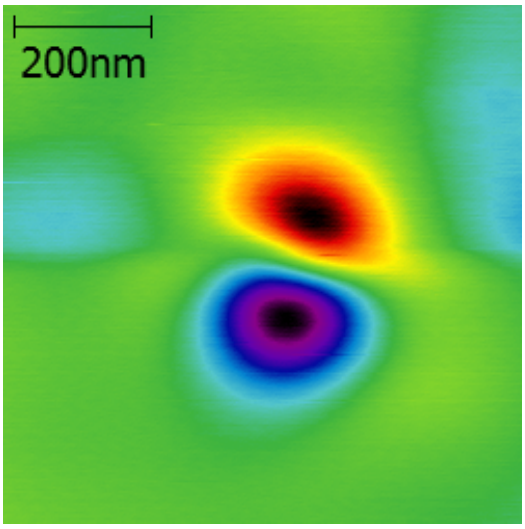

(b) Dipole

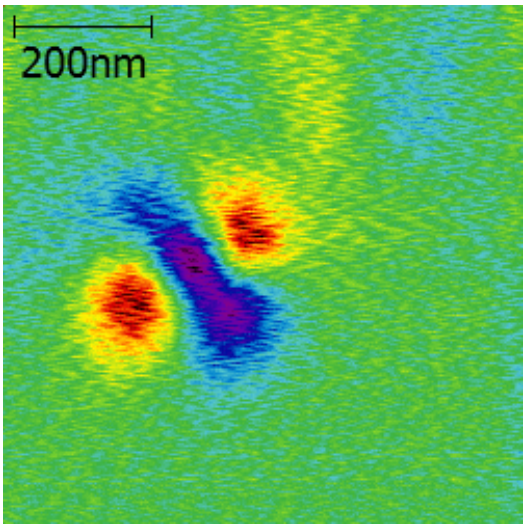

(c) Quadrupole

Figure 4.13: A variety of structures revealed by lateral scans of the tip above the sample. Note the inversion of forces between the trace and retrace of the quadrupole. The scans were taken at zero magnetic field and temperature of 2.7 Kelvin. The frequency span is 15Hz.

Equation 3.10, that is

$$\frac{\partial F_z}{\partial z} \propto \frac{1}{(z+\lambda_L)^5}. \tag{4.6}$$

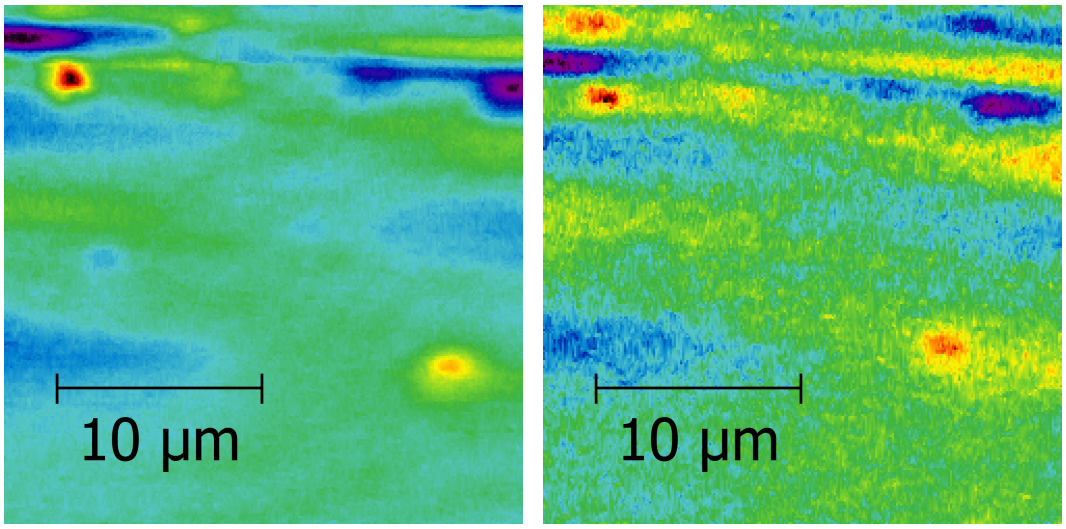

(a) 3K (b) 8K

Figure 4.14: A pole-rich landscape taken at two different temperatures, 3K and 8K. Despite the added noise at higher temperatures, all poles can be seen. Note that $T_c \approx 3$K. The frequency span is 7.5Hz.

Most of the force-distance curves we measured show this behaviour, as expected. An example for such a force-distance curve for the a-InO film is shown in Figure 4.15 with a fit to the Meissner force. We repeated measurements of such curves in many locations and obtained similar fits. The fits give λ_L in the range of $20 - 160\mu$m at a temperature of 2.7K. These are extremely large values, and a rather wide range, spanning almost an order of magnitude.

Past global measurements of the penetration depth in our group by optical measurements have given values of just a few microns (unpublished). Since these measurements probe the average value of the penetration depth in a large area of the sample, we may expect to find regions of the sample that have a much smaller λ_L to balance out the average. This is indeed the case, as we will show below.

When performing force-distance measurements close to one of the pole structures, similar to those of Figure 4.13, the shape of the force-distance curve is distorted, and additional features appear at distances up to 2 μm

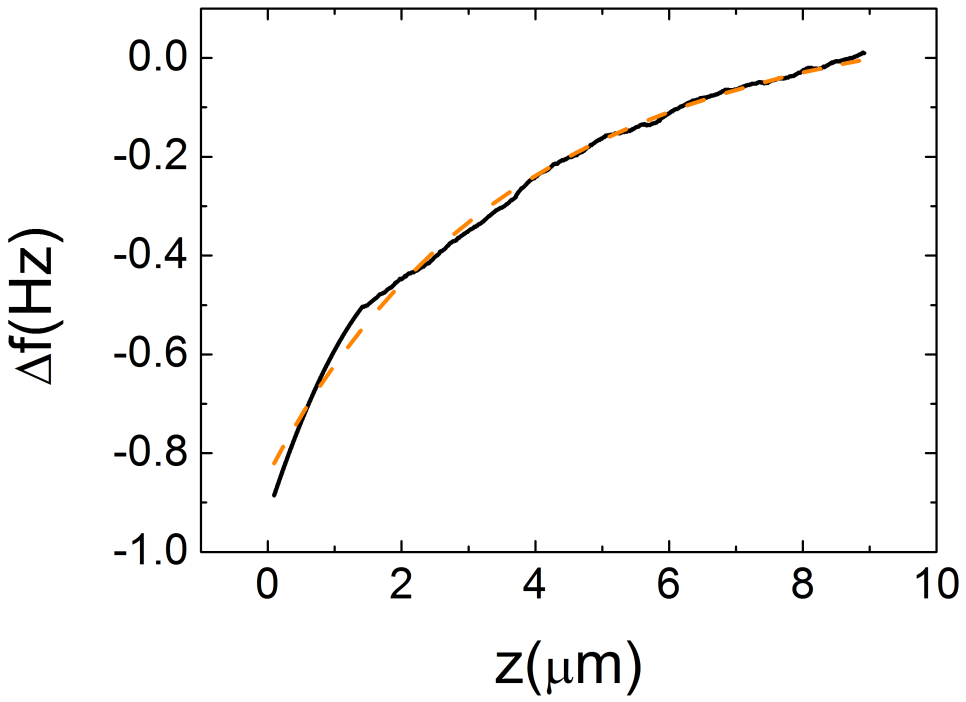

Figure 4.15: Shift of the cantilever's resonant frequency (proportional to the force derivative) as a function of distance from the a-InO film. Black curve is the raw data, the dashed orange line is a fit to the z-derivative of Equation 3.10.

from the surface. Figure 4.16 shows three force-distance curves. Each of these curves was taken at a different location on the sample, and each of these locations was close to a different pole. The additional anomalous force-derivative features are seen clearly. In the remainder of this section we will name these anomalous features dFF.

Figure 4.17 shows the force derivative scanned in the x-z plane above the sample. It was taken close to a monopole. It shows that the dFF decreases in amplitude when moving away from the pole. At a distance of $2\mu m$ from its centre the dFF is entirely suppressed. The right panel of the Figure shows a line taken from the left panel, along with a fit to the Meissner force for distances above the onset of the dFF. This fit gives $\lambda_L \approx 60\mu$m.

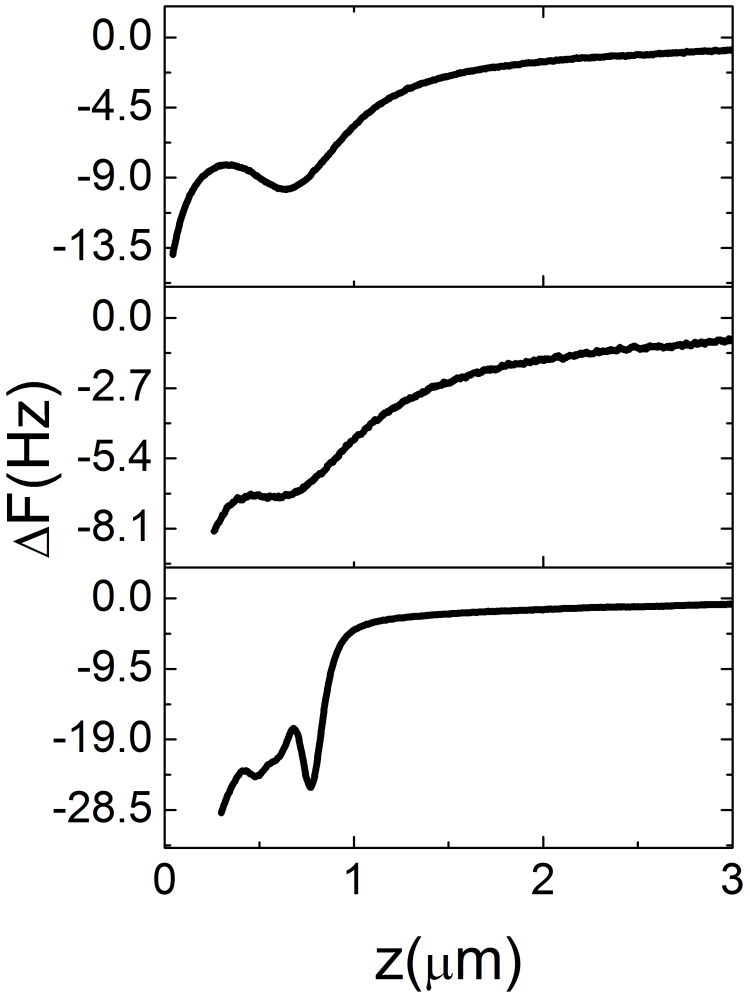

Figure 4.16: Anomalous force-distance curves above different locations of the sample, near three different poles.

The dFFs show a clear dependence on temperature and magnetic field. Figure 4.18 shows that the amplitude of a typical dFF is reduced with increasing temperature. The feature is observable at $T = 4.5K$ and $T = 5K$, however at $T = 6K$ the dFF is entirely suppressed.

Figure 4.19 shows the magnetic field dependence of two different dFFs. The left panel shows curves taken at the same location as that of Figure 4.18, for fields up to 1500mT. It can be seen that increasing the magnetic

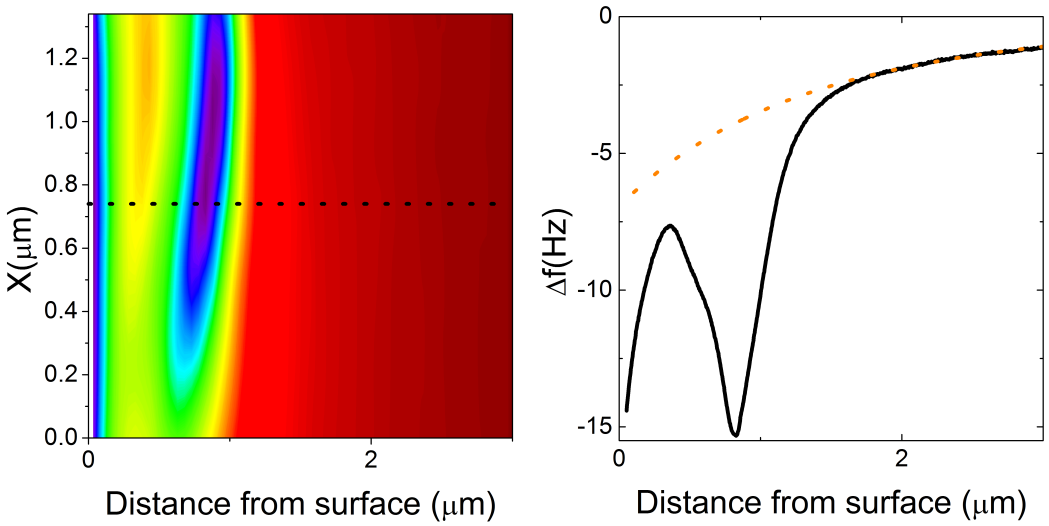

Figure 4.17: (**left**) A cross section in a plane perpendicular to the sample's surface (x-z plane). The purple strip at the left is caused when the tip touches the surface. The purple puddle to the right of it is where the non-monotonic anomaly is observed. The entire span of colours is $15Hz$. (**right**) A single profile from the colour map, taken at the dashed line. The dotted orange line is a fit to Equation 3.10 calculated for the curve part above the anomaly.

field reduces the amplitude of the anomaly, until its complete disappearance at $H = 1500$mT. The right panel shows force-distance curves at a different location in which the field was increased above $1500mT$. It is seen that the dFF reappears with an amplitude as prominent as that measured at low fields.

This dependence of the dFF on T and H can be directly attributed to superconductivity properties. It is weakened with increasing T up to T_c until its complete suppression at T_c, and the oscillatory behaviour in magnetic field may be attributed to the motion of vortices. As we will show below, the forces exerted on the tip can be attributed to its interaction with a nearby vortex.

In the following we suggest a model to reconstruct the force that causes these anomalies. The force-distance curve such as the one seen in Figure 4.17 shows two extrema. Clearly, a simple combination of an attractive

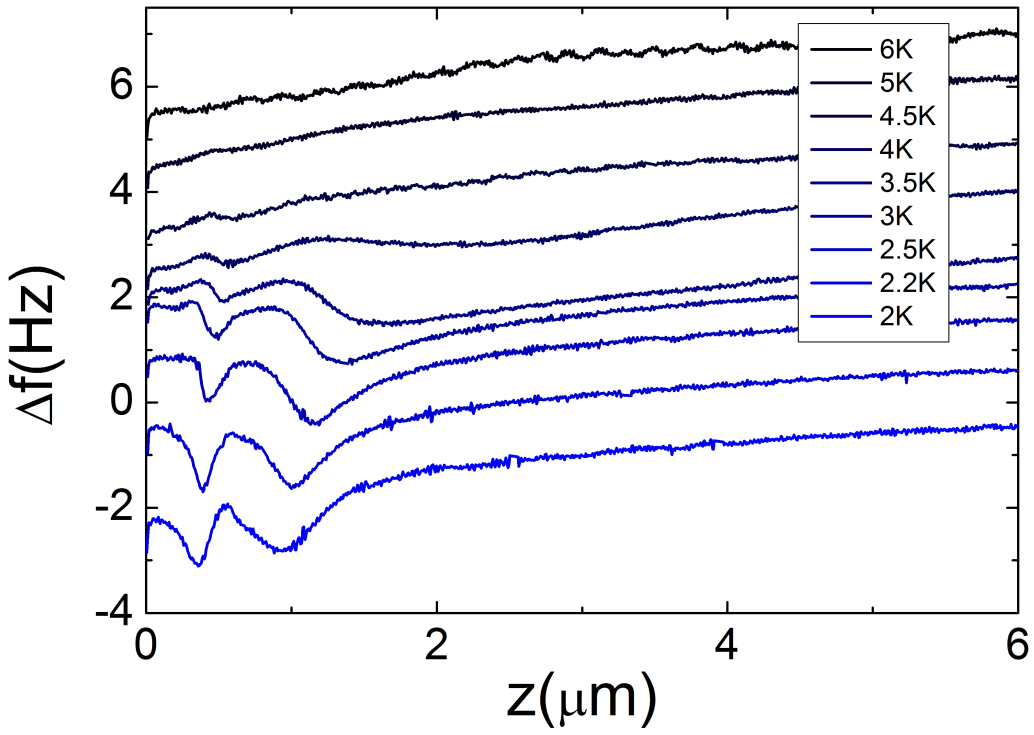

Figure 4.18: Force-distance curves for different temperatures. Curves are shifted vertically for clarity.

and a repulsive force with different decay rates with distance, such as the Lennard-Jones potential, does not suffice as those will yield only a single extremum.

Instead we develop a model in which the tip is a magnetic dipole with moment $\vec{m} = m\hat{z}$. The magnetic field, $\vec{B}$, that is generated by the vortex is the field of a magnetic monopole, since its opposite pole is masked by the superconducting film [72].

$$\vec{B} = \frac{\phi_0}{2\pi} \frac{x\hat{x} + (z + \lambda_L)\,\hat{z}}{\left(x^2 + (z + \lambda_L)^2\right)^{\frac{3}{2}}} \tag{4.7}$$

where we assume that $y = 0$ (the tip is in the x-z plane) for simplification. A sketch of these components can be seen in Figure 4.20.

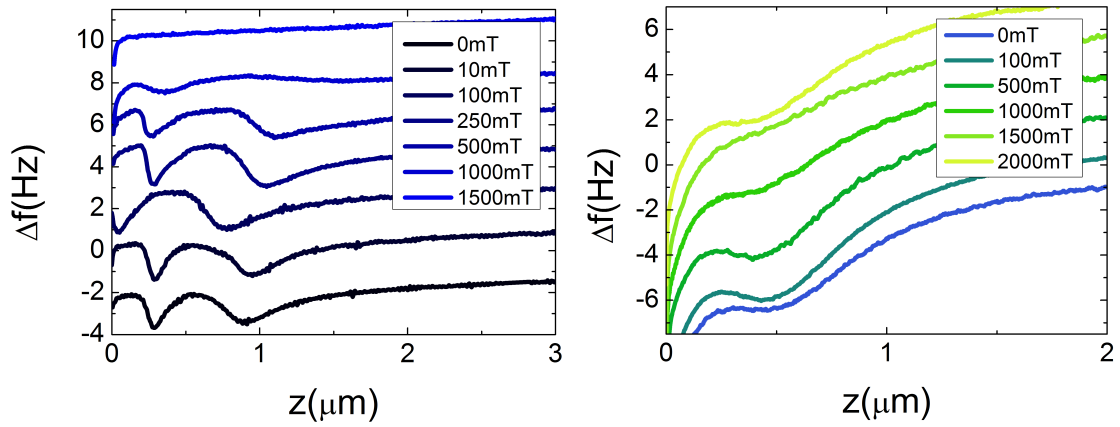

Figure 4.19: Force-distance curves for different magnetic fields for two different locations at $T = 2.7$K. Note that the in the right panel dip at $2000mT$ is deeper than the one at $1500mT$.

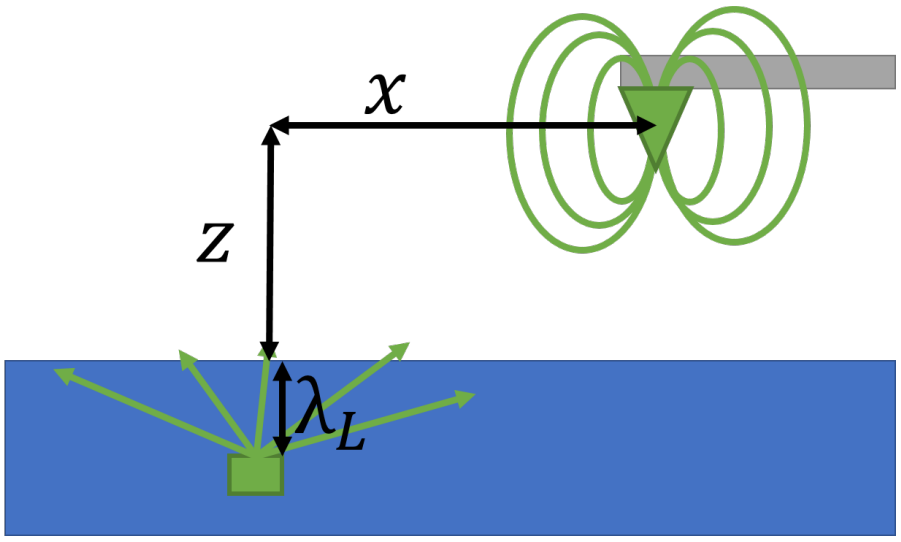

Figure 4.20: A sketch of the proposed scenario for the non-monotonous force-distance curves. The magnetic entities are green: the magnetic tip with a dipole field that is located at a height of z above the superconductor's surface and a lateral distance x from the vortex core. The vortex has a monopole field, and is located distance λ_L below the surface.

The force exerted on the tip is

$$\vec{F} = \vec{\nabla}\left(\vec{m} \cdot \vec{B}\right) \tag{4.8}$$

which ends up to be

$$F_x = m\frac{\phi_0}{2\pi}\frac{3x\left(z+\lambda_L\right)}{\left(x^2+\left(z+\lambda_L\right)^2\right)^{\frac{5}{2}}} \tag{4.9}$$

and

$$F_z = m\frac{\phi_0}{2\pi}\left[\frac{1}{\left(x^2+\left(z+\lambda_L\right)^2\right)^{\frac{3}{2}}} - \frac{3\left(z+\lambda_L\right)^2}{\left(x^2+\left(z+\lambda_L\right)^2\right)^{\frac{5}{2}}}\right]. \tag{4.10}$$

Since the measured quantity is proportional to the derivative $\frac{\partial F_z}{\partial z}$, one can write the following expression:

$$\frac{\partial F_z}{\partial z} = m\frac{\phi_0}{2\pi}\left[\frac{15\left(\lambda_L+z\right)^3}{\left(x^2+\left(z+\lambda_L\right)^2\right)^{\frac{7}{2}}} - \frac{9\left(\lambda_L+z\right)}{\left(x^2+\left(z+\lambda_L\right)^2\right)^{\frac{5}{2}}}\right]. \tag{4.11}$$

To this equation we add the derivative of Equation 3.10

$$\frac{\partial F_z}{\partial z} = \frac{3\mu_0 m^2}{8\pi\left(z+\lambda_L\right)^5} \tag{4.12}$$

and end up with a fitting equation. The fitting parameters are the amplitudes of the two forces, the penetration depth λ_L, and the lateral distance between the tip and the vortex core x.

While Equation 4.12 is a monotonous function, Equation 4.11 is not. This function tends to zero as $z \to \infty$, and has another zero when $z+\lambda_L = \sqrt{\frac{3}{2}}x$, assuming that $z+\lambda_L > 0$. Between these two zeros lies an extremum, as is shown in Figure 4.21 which shows the contributions of the two forces. Therefore such an interaction with a superconducting vortex may count for the non-monotonicity of the measured data.

We perform fits to the set of datum from Figure 4.19. The result is shown if Figure 4.22 where an excellent agreement, both quantitative and qualitative is seen.

From similar sets of data fitted to this theory we have calculated the penetration depth and found $\lambda_L = 0.73 \pm 0.1\mu$m at $T = 2K$ in this a-InO

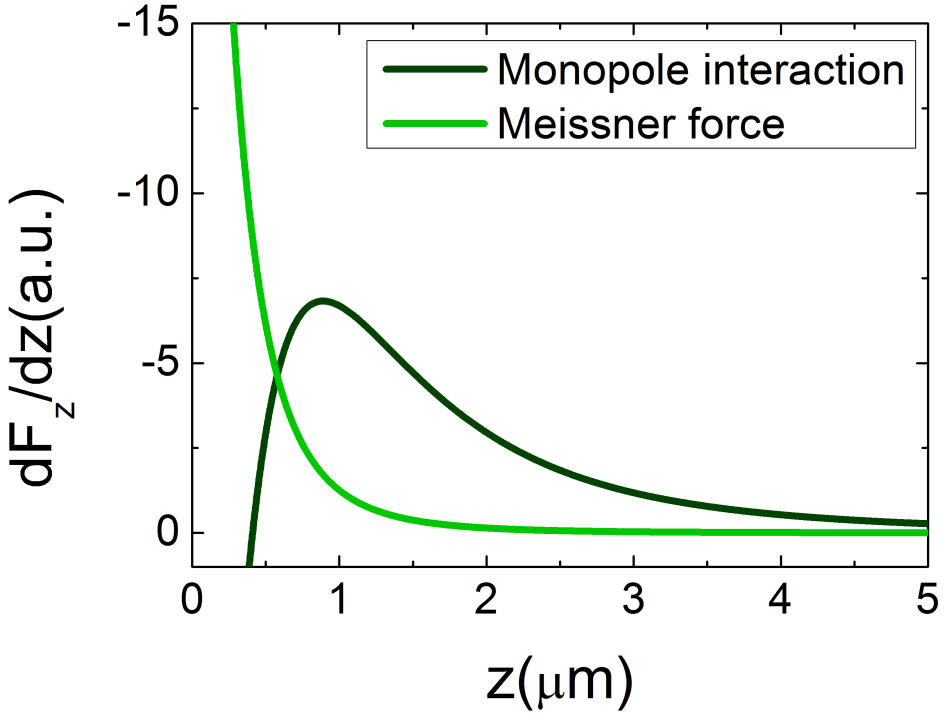

Figure 4.21: An example for curves calculated from Equations 4.11 and 4.12.

sample. This is a length much shorter than those measured with global measurements. It is also much smaller than the numbers we get with this local measurement in regions where the force-distance curve is monotonous (see Figure 4.15), which range in $20 - 160$ microns.

We infer from the above that the monotonous force-distance curves are observed in regions where superconductivity is weak or that it is locally absent. The non-monotonous measurements are in regions where superconductivity is strong enough to pin a vortex.

Note that according to Equation 4.9 another force acts on the vortex which may move it laterally in the film. This may account for some of misshapen force-distance curves which show only qualitative rather than quantitative agreement with our calculations, and even for the appearance of double peaks, if the vortex is pushed from one pinning site to another, like in Figure 4.19.

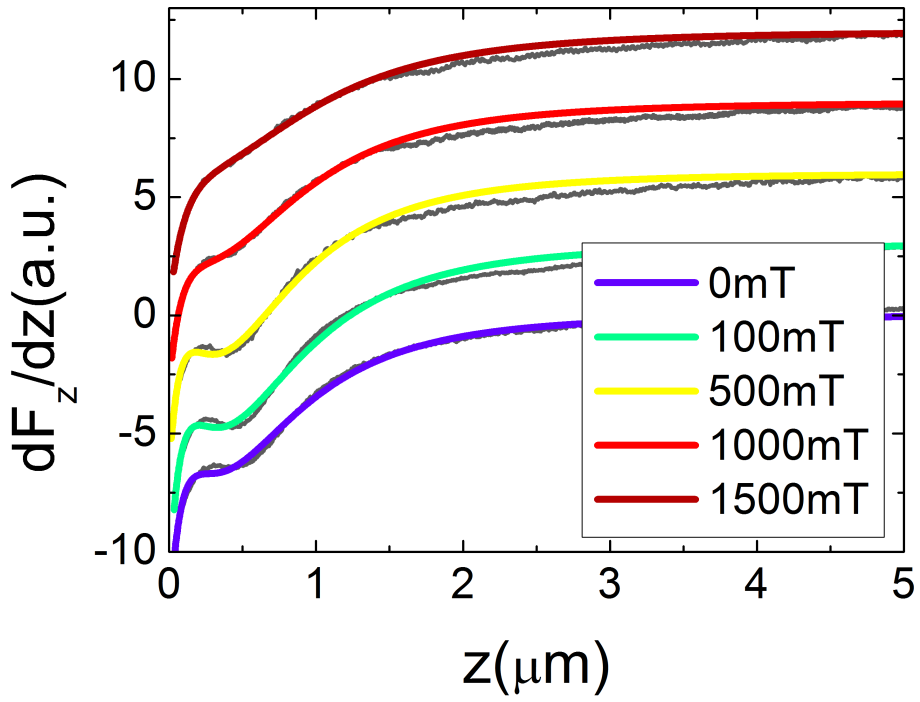

Figure 4.22: A set of fits (in colours) for the data from Figure 4.19 (replotted here in grey).

After we established that these force-distance curves probe superconductivity, we now turn the attention to Figure 4.18, which shows the temperature dependence of such force-distance curves. The peaks and valleys that are seen close to the surface at low temperatures slowly reduce in amplitude with the rise in temperature. However they completely disappear at $T = 6$K, which is much higher than the $T_c \approx 3$K we measure for this sample by transport. This implies that superconductivity exists at temperature above T_c.

Signs for superconductivity above T_c was measured before in high-temperature superconductors [73], [74], and also in a-InO in the form of a local pseudogap as shown in Figure 1.9. Our experiment adds another confirmation of the fact that T_c measured by transport does not tell the whole story of superconductivity in these films. Rather, the inherent electrical granularity allows superconductivity to exist in separate incoherent islands above T_c de-

termined by transport, which only signals the temperature at which global phase coherence is established.

Another important finding is the correspondence between the poles seen in Figure 4.13(a) and the anomalies in the touchdown curves. It seems that superconductivity in the film is 'attracted' to those massive poles.

We interpret these strong poles as places of great free electron concentrations, whereas the medium between them is highly localized sites that are formed due to Anderson localization. It is in these electron-rich regions that superconductivity is formed when reducing the temperature, rather than in the spaces between them where free electrons are scarce. This is the reason why λ_L is one or two order-of-magnitudes smaller in this region than in places far from localization sites.

The strong inhomogeneity of the electric field near these sites masks the magnetic effect from the superconducting vortices, however we believe that our results act as strong indications for the interplay between electron localization and superconductivity in a-InO films.

4.3 Proximity effect

As discussed in the background section (1.7), the proximity effect between a superconductor and a normal metal works in two ways, one is the leaking of superconductivity into the normal metal and the other is the weakening of superconductivity in the superconductor. We see evidences of the two effects in our measurements.

Fig. 4.23 shows two panels, each showing a pair of $R(T)$ curves. Each panel represents a different sample. The blue curve for each sample is the $R(T)$ taken for the bare a-InO film before any gold was deposited on top of it, and the red curve is taken after a minute amount of gold is deposited on top of it. The gold is so thin at this stage that the change in normal-state resistance of the film due to the addition of a parallel resistance is barely detectable, however a significant change is observed for the $R(T)$ curve.

We define, for the sake of rigorousness, the critical temperature of these films as the point where the film's resistance is half of its maximal value.

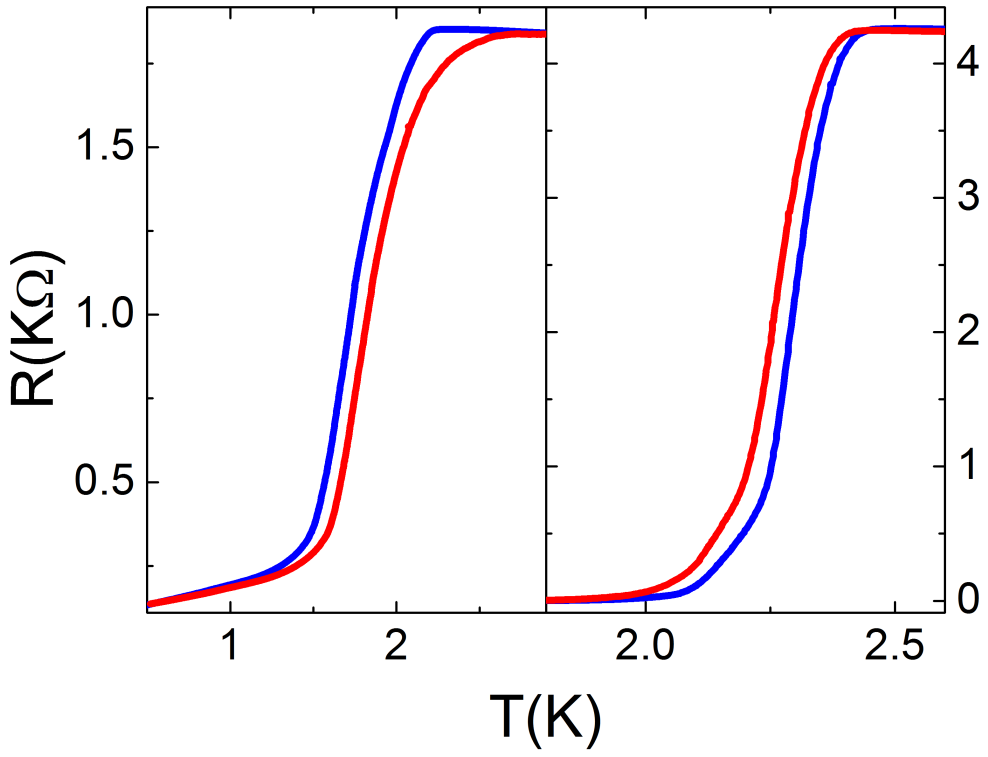

Figure 4.23: Measurements of two different samples, each showing two $R(T)$ curves. For both samples, the blue curve is for a bare a-InO film, and the red is with a small amount of gold deposited on top of it. The **left** panel shows an increase in T_c, and the **right** panel shows a decrease.

Other definitions of T_c yield qualitatively similar results. T_c of the sample in the left panel is changed from 1.755 Kelvin to a higher value of 1.858 Kelvin. For the sample in the right panel it is decreased from 2.296 Kelvin to 2.269 Kelvin. We see that the addition of gold can in some cases increase T_c and in others it may reduce it.

In Figure 4.24 we plot the maximal increase (or decrease) in the critical temperature in percent $\frac{\Delta T_c}{T_{c_0}}$ versus the critical temperature of the bare film T_{c_0}. The points that lay below the line $y = 0$ represent samples that showed a decrease in T_c upon the deposition of a gold top layer.

A clear separation between these two behaviours is seen, with the differentiating parameter being the bare sample critical temperature, T_{c_0}. This

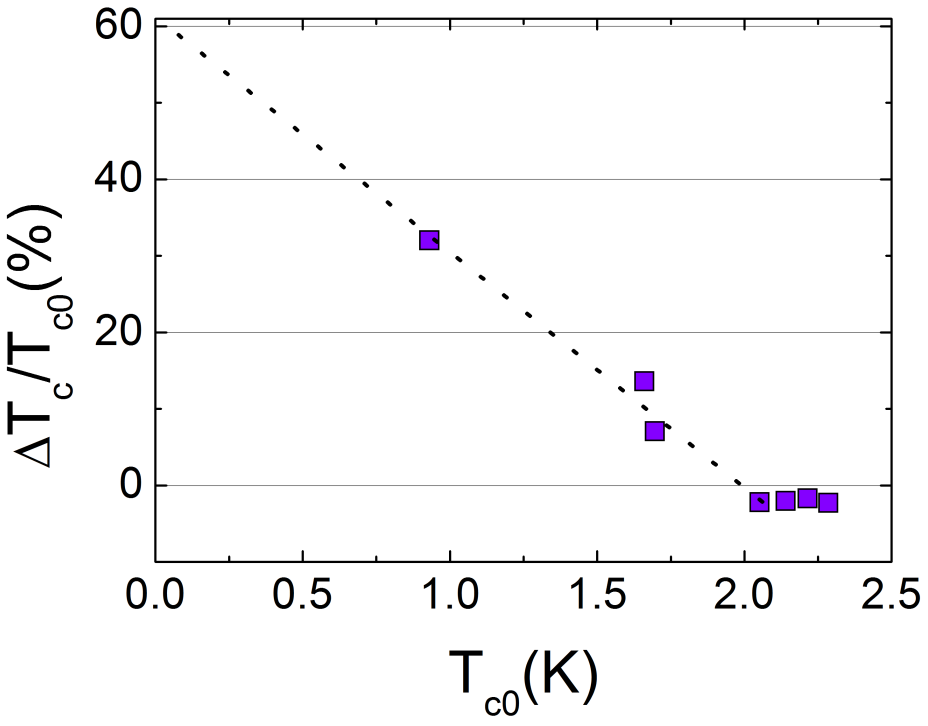

Figure 4.24: Maximal change in T_c in percent versus the initial T_c. The dotted line is merely a guide to the eye.

difference in T_{c_0} is due to a difference in disorder between the samples. Samples with lower disorder have a higher T_{c_0}, and vice versa. The 'critical' value of T_{c_0} which separates the two behaviours is 1.9K.

The change in T_c is more prominent in more disordered samples, and reaches about 30 percent in the most disordered superconducting sample we measured.

We mark the first group of samples, those with lower disorder and $T_{c_0} >$ 1.9K, as type A samples. All of these samples showed a small monotonous decrease in T_c, of 2-3 percent.

The second group, with samples that have a higher level of disorder and $T_{c_0} <$ 1.9K, we mark as type B samples. These samples showed a non-monotonous behaviour of T_c with Au thickness. Figure 4.25 shows T_c for all stages of deposition on an a-InO film versus resistance of deposited gold. For

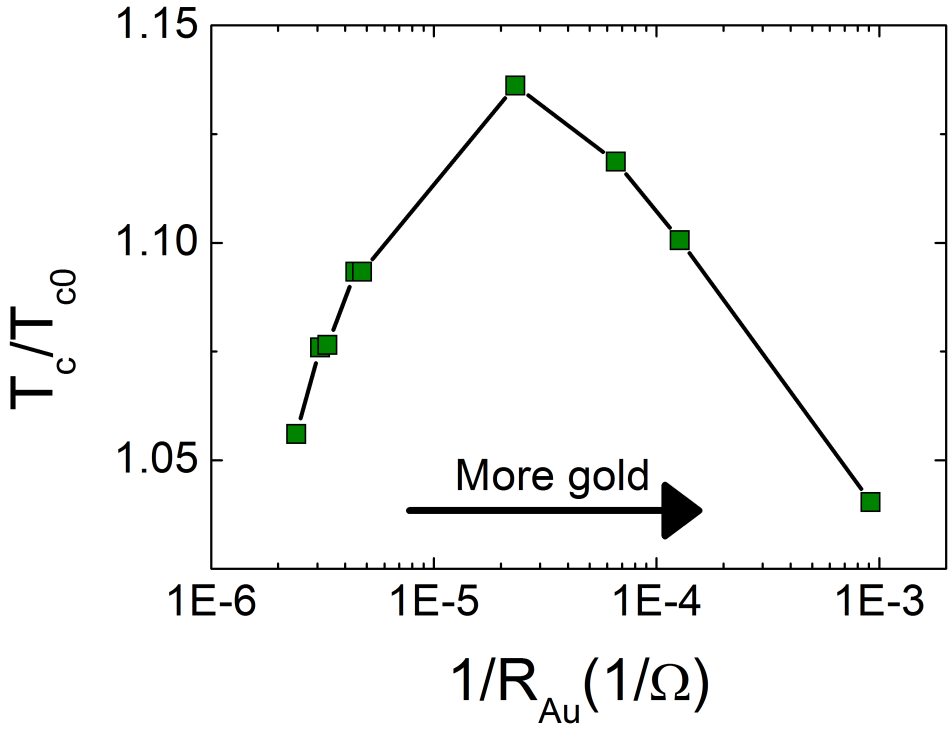

Figure 4.25: The change of T_c versus the normal-state resistance of the gold deposited on it for a type B sample which showed an increase in T_c. At some point a maximum value of T_c is reached, after which the addition of gold causes a decrease in T_c.

the first deposition stages an increase in T_c is observed. Upon adding yet more gold, a following decrease in T_c is observed.

We propose to interpret these results on the premises that a-InO has an emergent electrical granularity, and that the two effects in play are the proximity effect and the inverse proximity effect. We make this assertion as the only effect expected from depositing a gold over-layer on a homogeneous superconductor is a reduction of T_c, as seen in Figure 1.19. An increase in T_c was only seen in granular superconductors, as shown in Figure 1.20.

The main parameter that affects T_c in granular films is the inter-grain distance. As grains come closer to one another, the phase coherence between them is increased and so T_c increases. Figure 4.26 shows a sketch of the effect

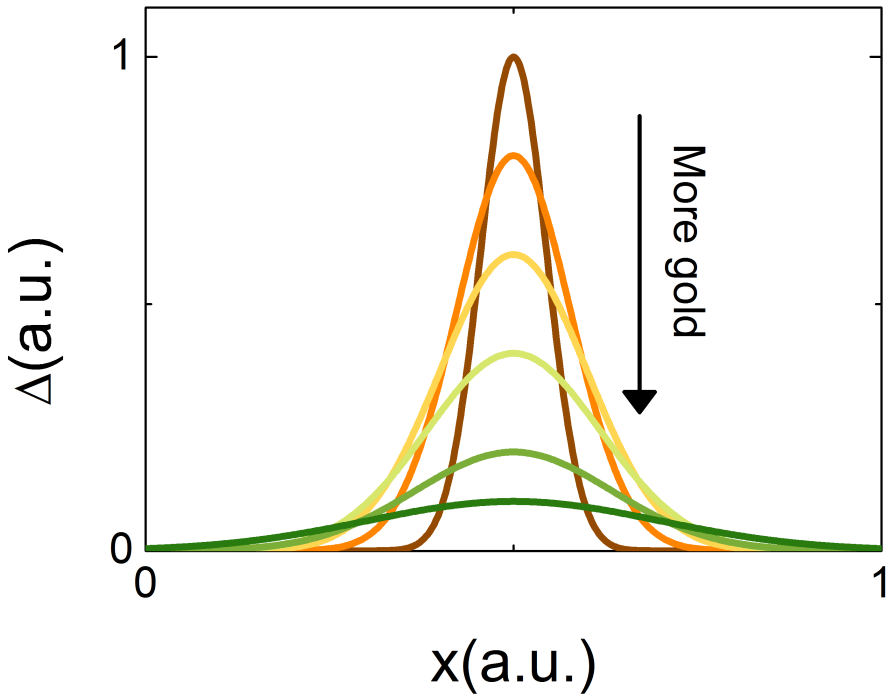

Figure 4.26: A schematic description of the effect of the proximity layer on a single grain of superconductivity in the a-InO film.

a proximity layer has on a superconducting island, illustrating that as more gold is added, the size of the grain increases and its height decreases.

When approaching the case where the islands are initially very close to one another, close to overlapping, the increase of grain size will not affect the coupling between the grains much. Instead, the inverse proximity effect would dominate and cause a decrease of T_c. When the inter-grain distance is slightly increased, the enlargement of grain size may act to increase T_c by improving the Josephson coupling between the grains.

We conclude that the difference between type A and type B samples is the initial coupling between superconducting islands. If they are initially well-coupled, their T_{c_0} is high, and the addition of the proximity layer will not affect the coupling much. If they are initially small and decoupled they will have a low T_{c_0} and the addition of a proximity layer may increase T_c

considerably.

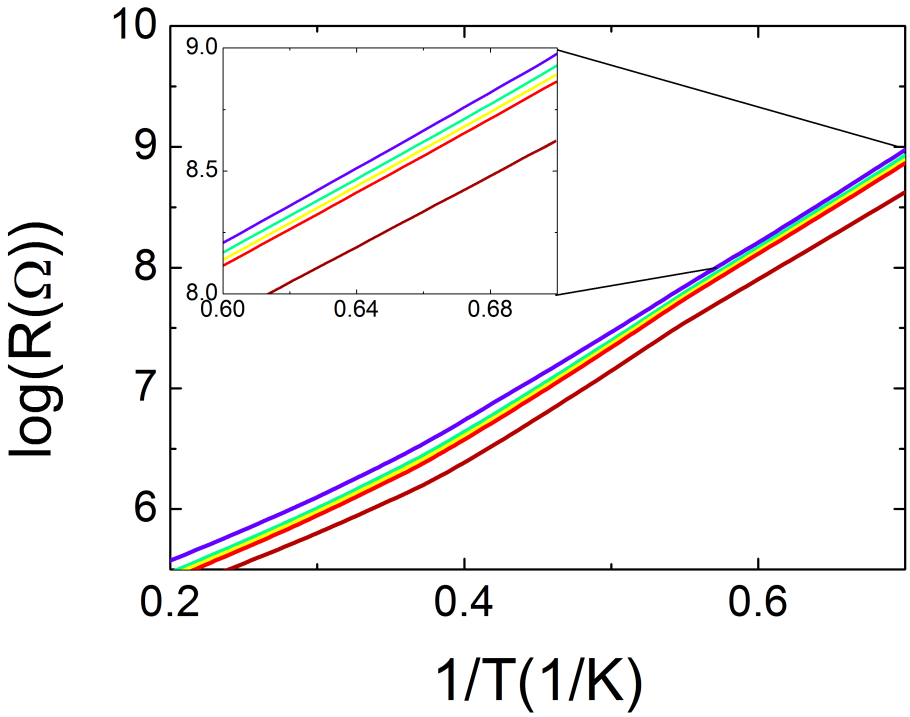

Figure 4.27: Logarithm of resistance versus inverse temperature for a proximity effect experiment conducted on an insulating a-InO film. The bare film resistance is plotted in blue, thickest gold layer is brown. Inset: a zoom-in to part of the larger plot, showing the lines to be parallel.

Several proximity effect measurements were also conducted on films that are on the insulating side of the SIT. Figure 4.27 shows a set of logarithm of resistance versus inverse temperature curves taken for an insulating film. This representation demonstrates that the $R(T)$ curves follow an Arrhenius behaviour

$$R(T) = R_0 e^{\frac{T_0}{T}} \tag{4.13}$$

with T_0 the activation temperature. As is seen in the inset, at low temperatures all lines are straight and are parallel to each other. The activation temperature for all of them is $T_0 = 7.3$K. Hence for samples on the insulating side of the transition it is seen that despite the reduced resistance due to the

addition of gold, the basic quantifier of disorder in the insulating state is unchanged.

This indifference of T_0 to the proximity layer stems from the large inter-grain distance. Since the proximity effect is limited in length, the effective size of the enlarged grains is limited by $r+\xi_N$, where r is the initial grain size and ξ_N is the length scale of Cooper pairs leaking into the normal metal, as defined in Equation 1.28. The inter-grain distance is larger than that limit in the case of this insulating film.

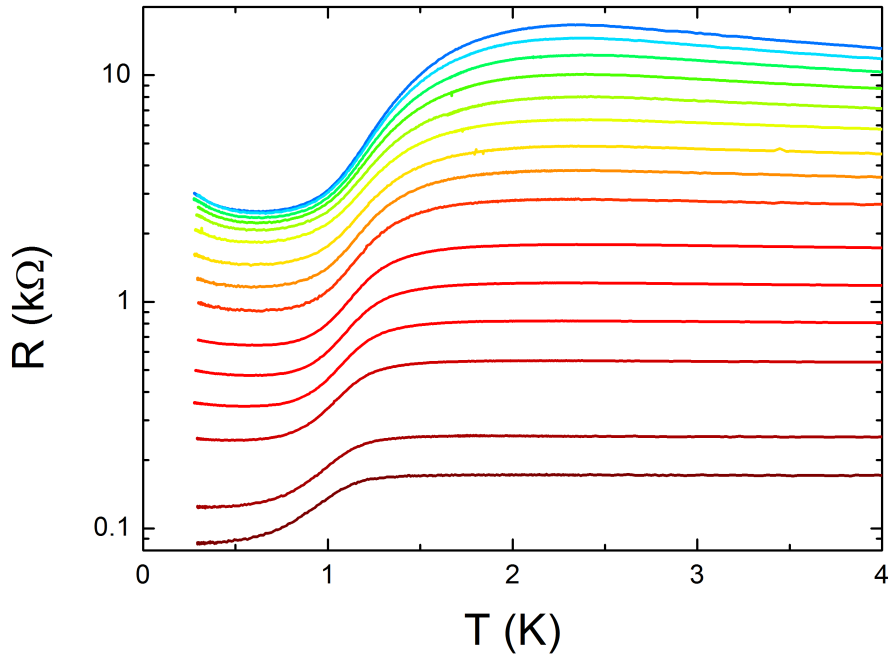

Figure 4.28: A set of $R(T)$ curves for a sample which shows resistance re-entrance. The addition of gold on top of it wipes out the re-entrant behaviour, making the sample superconducting at low temperatures.

Samples that are close to the SIT exhibit different results. An example for such a film is one that shows a re-entrant behaviour before the deposition of gold, similar to the re-entrant resistance shown in Figure 1.4.

Figure 4.28 shows a set of $R(T)$ curves for such a sample. For the first

Au layers the main effect of the Au layer is to reduce the resistance of the normal state. However for the following stages, those with a large amount of gold on them, the re-entrant part of the curves at low temperatures is reduced until no re-entrance can be seen in the last few curves. Hence in this case a proximity-effect-driven SIT has taken place.

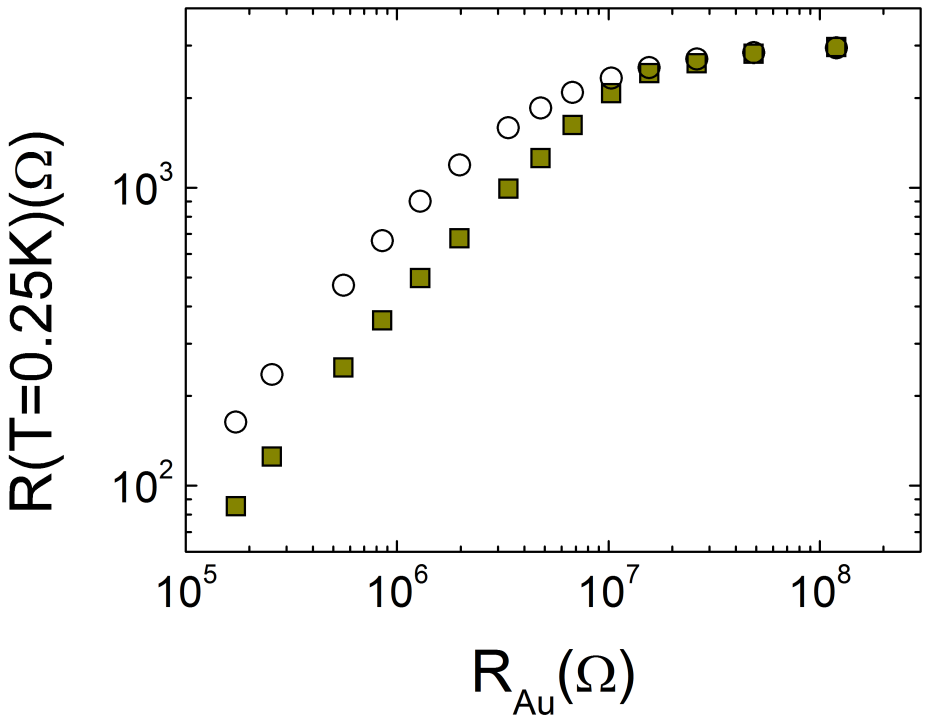

Figure 4.29: Resistance of the sample from Figure 4.28 at a temperature of 250mK versus the resistance of the gold deposited on it. Yellow squares are the measured values, and the empty circles are a calculation assuming the proximity effect does not affect the gold layer's resistance.

One may wonder whether the reduction in resistance is indeed due to the proximity effect, or whether it is just due to the addition of a resistance in parallel. In order to emphasize that the proximity effect indeed has a great part in changing the low-temperature behaviour, we assume that at high temperatures $T = 7K$ the change in resistance is due to the addition of a

parallel resistor, and extract the gold resistance by

$$R_{Au} = \frac{R_{total} R_{a-InO}}{R_{a-Ino} - R_{total}} \tag{4.14}$$

where R_{a-InO} is the resistance of the bare a-InO layer. We use the resistance of the gold layer for each stage of deposition, and calculate what the resistance for this stage would be at $T = 250mK$. In Figure 4.29, plotting the resistance at $250mK$ versus the gold resistance at $7K$, we compare these calculations with experiment. It is clear that as more gold is deposited these two resistances separate, up to a factor of 2 for the thickest layers of gold. We can therefore infer that it is the proximity effect that dominates the resistance behaviour in low temperatures.

The re-entrant behaviour is a fingerprint of phase fluctuations, and is seen in practically every quench-condensation experiment of granular superconductors. We can thus straightforwardly attribute the change in behaviour to the reduction of phase fluctuations between superconducting islands via the proximity layer. Superconductivity leaks into the gold layer in all directions, effectively enlarging the superconducting islands, making them closer to one another and increasing the Josephson coupling between them.

We conclude by pointing out that our interpretation fits well with the four different types of samples we measure:

Type A samples show a decrease in T_c as their initial state is of nearly overlapping islands, making the inverse proximity effect the only one that has detectable effect on them.

Type B samples show an increase in T_c as the enlargement of grains betters the inter-grain coupling.

Re-entrant behaviour is wiped out due to an increase in coupling, pushing the film out of the insulating state and into the superconducting state at $T = 0$.

Insulating films show indifference to the proximity effect as the initial inter-grain distance is too large for the proximity effect, which is limited in

range, to overcome.

Similar effects of the proximity effect and the inverse proximity effect were observed in high-T_c superconductors, namely LSCO [75], where a layer of over-doped LSCO caused an increase of T_c. In this case the over-doped LSCO is regarded as a metallic proximity layer. Similarly to our interpretation, they suggest that the increase in T_c is caused by an increase of phase stiffness in the interface between the different layers.

These results are a new strong indication that despite the structural homogeneity of a-InO films, an electrical granularity emerges that dominates the transport properties of the material.

Chapter 5

Summary and outlook

In this work we explored the disorder-driven SIT in a variety of methods, focusing on granularity, either in a physically granular system or in one where the granularity is emergent.

The unique approaches that we used for the characterization of the SIT allowed us to uncover new aspects and to reinforce previous findings.

Heat capacity

We used a unique set-up that allowed us to measure the heat capacity of ultra-thin films. This first-of-its-kind measurement, that we performed on granular films that undergo the SIT, allowed us an exclusive glimpse into the thermodynamics of the quantum phase transition.

We measured the heat capacity of two different granular films, one Pb and one Sn, as they underwent the SIT. Both showed the same qualitative results. Since heat capacity measurements, unlike transport measurements, are not sensitive to specific paths that electrons may prefer to travel by through the sample, we were able to conclusively show that superconductivity ia present in the grains of the film, even in the insulating side of the SIT. We found that the superconductor and the insulator stages of the SIT, which were characterized by transport measurements, are separated by a peak in the specific heat jump. We showed that this jump behaves as a power law of a quantum scaling parameter in the superconducting side of the SIT. The two

films yielded similar values of the critical exponent, about 0.25.

Clearly, further theoretical work is necessary to explain our results.

Future applications of the set-up used in this work may be used to study other systems that undergo the SIT, such as a-InO films, NbN films, TiN films and many more. It is an exceptional tool that allows one to make a distinction between the thermodynamic T_c of a superconductor and the temperature where in achieves global phase coherence.

In addition, it may be interesting to measure other thermodynamic functions in similar systems. The same fabrication techniques used in this study may be used to study the thermal conductivity of these systems. Susceptibility may be measured using a SQUID set-up. The different critical exponents may hold some information regarding the basic physics at play in these systems.

The Nernst effect may also be measured with high accuracy using the fabrication methods used in this study. Two high-accuracy thermometers and one heater are needed for such a set-up. The measurement of a vortex-induced voltage in the insulating side of the SIT, and the specifics of the Nernst factor versus the quantum scaling parameter may hold a lot of information.

Local magnetism

We used a cryogenic MFM system in order to study local magnetism in a-InO films. Following hints from past experiments, we looked for diamagnetic signals and other hints for superconductivity, such as vortices, at temperatures higher than the T_c that is determined by transport measurements.

We found new evidences for the existence of superconductivity in the film at temperatures as high as 6K in a film with $T_c < 3$K. This was achieved by measuring anomalous force-distance curves that we attributed to vortices that reside in the film.

Using normal force-distance curves we found that λ_L is extremely large, of the order of tens to hundreds of microns, away from the superconducting islands in the film, and is reduced considerably down to less than one micron

in the islands.

In addition, we have shown a strong indication for the interplay between the Anderson localization and the disorder-induced superconducting grains, as strong superconductivity with small values of λ_L was only observed in areas of high electron concentrations, i.e. away from the localization sites.

Proximity effect

We used a quench-condensation apparatus in order to deposit minute amounts of gold on top of thin a-InO films. By doing so we changed the $R(T)$ characteristics of the films. These changes are caused by the proximity effect and the inverse proximity effect, both interplaying in either spreading superconductivity or diminishing it.

We observed two major changes in the sample. One is the shift of T_c to either higher or lower values. There is a clear separation between the two different behaviours, depending on the initial T_c of the sample.

We also saw several cases where the addition of a proximity layer on top of a film that is insulating at $T = 0$ pushed the film into the superconducting regime, demonstrating a proximity-effect-tuned SIT.

We attributed all of the phenomena observed in this set of proximity effect experiments to the interplay between the spreading of superconductivity in the gold layer due to the proximity effect that makes the superconducting islands larger and more coupled to one another, and the diminishing of superconductivity due to the inverse proximity effect that causes the islands to become smaller and more decoupled.

Bibliography

[1] "The cold wars: A history of superconductivity", in, J. Matricon and G. Waysand, Eds. Rutgers University Press, 2003.

[2] H. K. Onnes, *Comm. Phys. Lab. Univ. Leiden*, vol. 120b, 1911.

[3] V. L. Ginzburg and L. D. Landau, *Zh. Eksp. Teor. Fiz.*, vol. 20, p. 1064, 1950.

[4] J. Bardeen, L. N. Cooper, and J. R. Schrieffer, *Phys. Rev.*, vol. 101, p. 162, 1957.

[5] J. G. Bednorz and K. A. Mueller, *Z. Phys.*, vol. 64, p. 189, 1986.

[6] H. F. Hess, R. B. Robinson, R. C. Dynes, J. J. M. Valles, and J. V. Waszczak, *Phys. Rev. Lett.*, vol. 62, p. 214, 1989.

[7] A. A. Abrikosov, *Sov. Phys. JETP*, vol. 5, p. 1174, 1957.

[8] S. Komineas, *Phys. Rev. Lett.*, vol. 99, p. 117 202, 2007.

[9] A. Pourret, P. Spathis, H. Aubin, and K. Behnia, *New Journal of Physics*, vol. 11, p. 055 071, 2009.

[10] P. A. Lee and T. V. Ramakrishnan, *Rev. Mod. Phys.*, vol. 57, p. 287, 1985.

[11] P. Anderson, *Phys. Rev.*, vol. 109, p. 1492, 1958.

[12] N. Mott, *Phil. Mag.*, vol. 19, p. 835, 1969.

[13] A. L. Efros and B. I. Shklovskii, *J. Phys. C*, vol. 8, 1975.

[14] P. W. Anderson, *J. Phys. Chem. Solids*, vol. 11, p. 26, 1959.

[15] A. Abrikosov and L. Gor'kov, *Sov. Phys. JETP*, vol. 9, p. 220, 1959.

[16] D. B. Haviland, Y. Liu, and A. M. Goldman, *Phys. Rev. Lett.*, vol. 62, p. 2180, 1989.

[17] O Crauste, F Couedo, L Bergé, C Marrache, and L Dumoulin, *J. Phys.: Conf. Ser.*, vol. 400, p. 022 012, 2012.

[18] A. F. Hebard and M. A. Paalanen, *Phys. Rev. Lett*, vol. 65, p. 927, 1990.

[19] A. Johansson, I. Shammass, N. Stander, E. Peleda, G. Sambandamurthya, and D. Shahar, *Solid State Communications*, vol. 151, p. 743, 2011.

[20] A. T. Bollinger, G. Dubuis, J. Yoon, D. Pavuna, J. Misewich, and I. Božović, *Nature*, vol. 472, p. 458, 2011.

[21] A. Frydman, *Physica C*, vol. 391, p. 189, 2003.

[22] S. Maekawa and H. Fukuyama, *J. Phys. Soc. Jpn*, vol. 51, p. 1380, 1981.

[23] H. Takagi, R. Souda, and Y. Kuroda, *Progress of Theoretical Physics*, vol. 68, p. 426, 1982.

[24] A. Finkel'shtein, *JETP*, vol. 45, p. 46, 1987.

[25] R. P. Barber, L. M. Merchant, A. L. Porta, and R. C. Dynes, *Phys. Rev. B*, vol. 49, p. 3409, 1994.

[26] D. Shahar and Z. Ovadyahu, *Phys. Rev. B*, vol. 46, p. 10 917, 1992.

[27] D. Kowal and Z. Ovadyahu, *Physica C*, vol. 468, p. 322, 2008.

[28] B. Sacepe, T. Dubouchet, C. Chapelier, M. Sanquer, M. Ovadia, D. Shahar, M. Feigelman, and L. Ioffe, *Nature Phys.*, vol. 7, p. 239, 2011.

[29] K. Bouadim, Y. L. Loh, M. Randeria, and N. Trivedi, *Nature Physics*, vol. 7, p. 884, 2011.

[30] P. Curty and H. Beck, *Phys. Rev. Lett.*, vol. 91, p. 257 002, 2003.

[31] G. Sambandamurthy, L. W. Engel, A. Johansson, and D. Shahar, *Phys. Rev. Lett.*, vol. 92, p. 107 005, 2004.

[32] Y. Dubi, Y. Meir, and Y. Avishai, *Phys. Rev. B*, vol. 73, p. 054 509, 2006.

[33] "Quantum phase transitions", in, S. Sachdev, Ed. Cambridge, 2011.

[34] S. L. Sondhi, S. M. Girvin, J. P. Carini, and D. Shahar, *Rev. Mod. Phys.*, vol. 69, p. 315, 1997.

[35] P. Debye, *Annalen der Physik*, vol. 39, p. 789, 1912.

[36] "Introduction to superconductivity", in, M. Tinkham, Ed. Dover Publications, 2004.

[37] W. Corak, B. Goodman, C. Satterthwaite, and A. Wexler, *Phys. Rev.*, vol. 96, p. 1442, 1954.

[38] C. A. Shiffman, J. F. Cochran, and M. Garber, *J. Phys. Chem. Solids*, vol. 24, p. 1369, 1963.

[39] Y. N. Ovchinikov and A. A. Varlamov, *Phys. Rev. Lett.*, vol. 94, p. 107 007, 2005.

[40] B. Muhlschlegel, D. J. Scalapino, and R. Denton, *Phys. Rev. B*, vol. 6, p. 1767, 1972.

[41] T. Tsuboi and T. Suzuki, *Journal of the Physical Society of Japan*, vol. 42, p. 437, 1977.

[42] N. A. H. K. Rao, J. C. Garland, and D. B. Tanner, *Phys. Rev. B*, vol. 29, p. 1214, 1984.

[43] G. Binnig, C. F. Quate, and C. Gerber, *Phys. Rev. Lett.*, vol. 56, p. 930, 1986.

[44] Y. Martin, C. C. Williams, and H. K. Wickramasinghe, *J. Appl. Phys.*, vol. 61, p. 4723, 1987.

[45] Y. Martin and H. K. Wickramasinghe, *Appl. Phys. Lett.*, vol. 50, p. 1455, 1987.

[46] A. Moser, H. Hug, B. S. I. Parashikov, O. Fritz, H. Thomas, A. Baratoff, and H. Guntherodt, *Phys. Rev. Lett.*, vol. 74, p. 1847, 1995.

[47] A. Volodin, K. Temst, C. V. Haesendonck, and Y. Bruynseraede, *Appl. Phys. Lett.*, vol. 73, p. 1134, 1998.

[48] A. Volodin, K. Temst, C. V. Haesendonck, and Y. Bruynseraede, *Physica C*, vol. 332, p. 156, 2000.

[49] A. Volodin, K. Temst, C. V. Haesendonck, and Y. Bruynseraede, *App. Phys. Lett.*, vol. 73, p. 1134, 1998.

[50] A. Volodin, K. Temst, Y. Bruynseraede, C. V. Haesendonck, M. I. Montero, I. K. Schuller, B. Dam, J. M. Huijbregste, and R. Griessen, *Physica C*, vol. 369, p. 165, 2002.

[51] L. Lan, A. O. M., L. T. M., H. C. W., K. Beena, C. Jiun-Haw, A. J. G., F. I. R., K. J. R., and M. K. A., *Phys. Rev. B*, vol. 81, p. 100 501, 10 2010.

[52] R. Holm and W. Meissner, *Z. Physik*, vol. 74, p. 715, 1932.

[53] "Superconductivity", in, R. D. Parks, Ed. Marcel Dekker, 1969, ch. 17.

[54] P. Visani, "Superconducting proximity effect between silver and niobium", PhD thesis, University of Milano, 1990.

[55] P. G. D. Gennes and E. Guyon, *Phys. Lett*, vol. 3, p. 178, 1963.

[56] N. R. Werthamer, *Phys. Rev.*, vol. 132, p. 2440, 1963.

[57] P. G. D. Gennes, *Rev. of Mod. Phys.*, vol. 36, p. 225, 1964.

[58] P. Hilsch, *Zeitschrift für Physik*, vol. 511, p. 225, 1962.

[59] J. Clarke, *Journal De Physique*, vol. 29, pp. C2–3, 1968.

[60] L. Merchant, J. Ostrick, R. P. B. Jr., and R. C. Dynes, *Phys. Rev. B*, vol. 63, p. 134 508, 2001.

[61] A. Frydman, L. Merchant, and R. Dynes, *Physica status solidi (b)*, vol. 218, p. 173, 2000.

[62] U. Givan and Z. Ovadyahu, *Phys. Rev. B*, vol. 86, p. 165 101, 2012.

[63] P. Sullivan and G. Seidel, *Phys. Rev.*, vol. 173, p. 679, 1968.

[64] J. H. Xu, J. H. M. Jr., and C. S. Ting, *Phy. Rev. B*, vol. 51, p. 424, 1994.

[65] J. Pearl, *Appl. Phys.*, vol. 37, p. 4139, 1966.

[66] W. S. Corak and C. B. Satterthwaite, *Phy. Rev.*, vol. 102, p. 662, 1956.

[67] J. E. Neighbor, J. F. Cochran, and C. A. Shiffman, *Phy. Rev.*, vol. 155, p. 384, 1967.

[68] W. G. Bouwman and W. H. de Jeu, *Phys. Rev. Lett.*, vol. 68, p. 800, 1992.

[69] A. P. Gottlob and M. Hasenbusch, *Physica A*, vol. 201, p. 593, 1993.

[70] A. Auerbach, Private communication.

[71] D. Sherman, U. S. Pracht, B. Gorshunov, S. Poran, J. Jesudasan, M. Chand, P. Raychaudhuri, M. Swanson, N. Trivedi, A. Auerbach, M. Scheffler, A. Frydman, and M. Dressel, *Nature Physics*, vol. 11, p. 188, 2015.

[72] A. M. Chang, H. D. Hallen, L. Harriott, H. F. Hess, H. L. Kao, J. Kwo, R. E. Miller, R. Wolfe, J. van der Ziel, and T. Y. Chang, *App. Phys. Lett.*, vol. 61, no. 16, 1992.

[73] M. Hashimoto, I. M. Vishik, R. He, T. Devereaux, and Z. Shen, *Nature physics*, vol. 10, p. 483, 2014.

[74] S. Kaiser, C. Hunt, D. Nicoletti, W. Hu, I. G. H. Y. Liu, M. L. Tacon, T. Loew, D. Haug, B. Keimer, and A. Cavalleri, *Phys. Rev. B*, vol. 89, p. 184 516, 2014.

[75] O. Yuli, I. Asulin, O. Millo, D. Orgad, L. Iomin, and G. Koren, *Phys. Rev. Lett.*, vol. 101, p. 057 005, 2008.

Appendix A

An article describing the heat capacity experiment

Specific heat measurement set-up for quench condensed thin superconducting films

Shachaf Poran,[1,2,3] Manel Molina-Ruiz,[1,2,4] Anne Gérardin,[1,2] Aviad Frydman,[3] and Olivier Bourgeois[1,2]

[1]*Institut NÉEL, CNRS, 25 Avenue des Martyrs, F-38042 Grenoble, France*
[2]*Univ. Grenoble Alpes, Inst NEEL, F-38042 Grenoble, France*
[3]*Department of Physics, Bar-Ilan University, Ramat Gan 52900, Israel*
[4]*Departamento de Física, Universidad Autónoma de Barcelona, 08193 Bellaterra, Spain*

(Received 4 March 2014; accepted 27 April 2014; published online 22 May 2014)

We present a set-up designed for the measurement of specific heat of very thin or ultra-thin quench condensed superconducting films. In an ultra-high vacuum chamber, materials of interest can be thermally evaporated directly on a silicon membrane regulated in temperature from 1.4 K to 10 K. On this membrane, a heater and a thermometer are lithographically fabricated, allowing the measurement of heat capacity of the quench condensed layers. This apparatus permits the simultaneous thermal and electrical characterization of successively deposited layers *in situ* without exposing the deposited materials to room temperature or atmospheric conditions, both being irreversibly harmful to the samples. This system can be used to study specific heat signatures of phase transitions through the superconductor to insulator transition of quench condensed films. © *2014 AIP Publishing LLC*. [http://dx.doi.org/10.1063/1.4875590]

INTRODUCTION

Understanding the emergence of macroscopic quantum states (superfluidity, superconductivity) in low-dimensional systems or in disordered media still represents a major challenge for condensed matter physics at low temperatures. In many cases, the lower dimensionality plays the same role as the disorder to induce a transition from a superconducting state to an insulating state. This phase transition occurs at zero temperature, hence it is an example for a quantum phase transition in which quantum rather than classic fluctuations drive the transition.[1–3]

The materials of interest are characterized by a critical parameter (film thickness, impurity concentration, magnetic field, disorder) that induces a transition from a superconducting state to an electrically insulating state. Despite many years of research in this field a unified and comprehensive theoretical picture is still lacking and the full understanding of the interplay between disorder and dimensionality is among the most exciting problems of contemporary condensed matter physics.

Experimentally there has been much activity in the field focusing on transport (see, for example, Refs. 4–9), magnetoresistance,[10–15] proximity effect,[16] tunneling,[17–21] and ac conductivity,[22–24] however a true thermodynamic approach has not been explored yet. In this respect, measuring the specific heat of 2D superconducting films through the superconductor to insulator transition (SIT) is a very important experimental direction though rather challenging. The main difficulty is measuring the specific heat contribution of an ultrathin superconducting film, this naturally requires a sensor having a high sensitivity.

In this paper, we describe a unique technique that enables the measurement of superconducting layers starting from quasi-2D films and extending towards the 3D limit. It is based on utilizing recent experimental developments of highly sensitive specific heat measurements.[25,26] Up to date a specific heat measurement on single ultra-thin superconducting layers has never been performed. The only related experiments were specific heat measurements on multi-layered[27] or thick layers of superconductors.[28,29] In this work, we demonstrate the operation of a heat capacity experiment of ultra-thin layers of superconducting Pb successively evaporated *in situ* at low temperature directly on the thermal sensor. These may be granular when directly evaporated on the silicon membrane or continuous when using an adhesion sub-layer of germanium or antimony. The experimental set-up allows the first measurement of superconducting ultrathin films with properties spanning the superconducting to insulator transition.

EXPERIMENTAL

A new apparatus has been designed and built that allows the concomitant measurement *in situ* of heat capacity and electrical resistivity of quench condensed superconducting thin films. The system has been tested by evaporating pure Pb (99.99%) on a sensor that is regulated at a temperature of 8 K. The measurement of the heat capacity is based on a membrane sensor, a technique of nanocalorimetry used at low temperature by various group either on SiN or Si suspended device.[30–33] The fabrication of the calorimetric sensor based on a membrane has been described in Refs. 25 and 31; here we highlight its principal particularities. The active part of the setup is composed of a thin silicon membrane (5 μm thick) on which a NbN thermometer and a Cu heater have been fabricated using regular clean room process permitting thermal measurements.[34] Extra electrodes were added onto the membrane allowing simultaneous electrical characterizations of the evaporated thin films by depositing gold leads with a thin titanium underlayer through a mechanical mask.

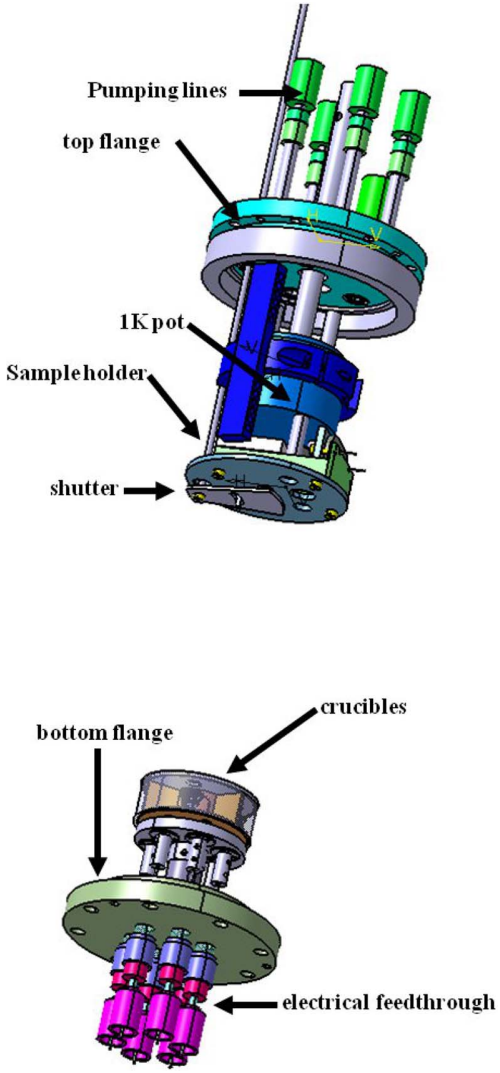

FIG. 1. Schematic view of the evaporation chamber. The bottom part contains three crucibles which are used for thermal evaporation of various materials (Pb in this work). The calorimetric sensor (membrane) is located in the upper part as well as the temperature-regulated stage. A shutter is used to start and stop evaporation on the membrane; a 5 MHz quartz crystal is used to monitor the film thickness. The temperature can be regulated from 1.5 K to 15 K.

The membrane is mounted in the probe face down and fixed on the sample holder (see Fig. 1). Electrical contacts are made using regular wire microbonding. The evaporation system is located at the bottom of the probe. It is constituted by three thermal evaporation baskets made of tungsten wires as sketched in Figs. 1 and 2(a). Each basket contains a load (here Pb) that has been pre-melted thus achieving wetting in the basket prior to cooling down.[16,35,36] The majority of radiation emanating from the baskets during evaporation is screened by a stainless steel shield. The electrical feedthroughs are composed of copper wires that go through a copper container filled with helium tight stycast resist brazed on the stainless steel flange. Film evaporation is performed by applying a current of 8 amps and a voltage of approximately 1.2 V.

A shutter that can be opened or closed from the top part of the apparatus (at room temperature) has been mounted thus

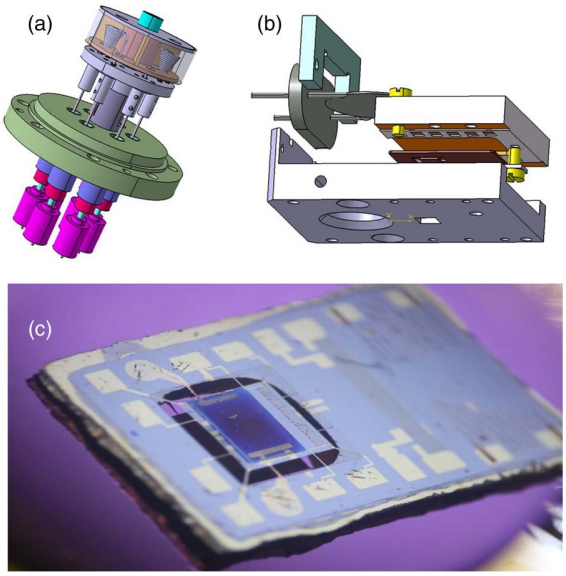

FIG. 2. (a) Detailed sketch of the bottom part of the evaporation chamber. The different baskets used for the quench condensation can be distinguished. (b) Sketch of the sample holder part were the silicon membrane is located behind the mechanical mask defining the area of deposited film. (c) A photograph of a silicon membrane after an evaporation located between the heater and the thermometer of the membrane. The electrodes used for the electrical characterization of the evaporated sample are seen on the two sides of the membrane.

enabling blocking of the evaporation on the membrane sensor at will. A quartz crystal is used to monitor the thin film evaporation. The sample holder is installed on a temperature regulated stage, connected to a 1 K pot, that is equipped with a heater and a NbN thermometer calibrated against a Cernox thermometer (see Fig. 2(b)). The evaporated materials are directed to the membrane through a mechanical mask that has been adjusted to allow deposition only on the center part of the membrane including the gold electrical leads (see Fig. 2(c)). The complete evaporation chamber is pumped and immersed in liquid helium ensuring an ultra-high cryogenic vacuum in the measurement chamber.

Before any material deposition, the heat capacity versus temperature of the membrane sensor is measured in the range 1.5−15 K in order to obtain a background curve. The thin films are then sequentially evaporated on the silicon membrane at a regulated temperature of 8 K after which the heat capacity and the film resistance are measured.

Heat capacity is measured using the ac calorimetry technique,[37] performed by supplying an ac power to the heater, thus inducing a temperature oscillation of the thermally isolated membrane, thermometer, heater, and thin films deposited on top.[25,31] The temperature change on the thermometer is measured using a lock-in amplifier at twice the electrical excitation frequency (second harmonic).

The operating frequency lies in the middle of the adiabatic plateau (in this work $f \simeq 1$ kHz) where the period of the oscillation of temperature is smaller than the thermalization time to the heat bath but larger than the diffusion time in the membrane. In this frequency regime, the temperature of the complete system composed of the sensor and the sample

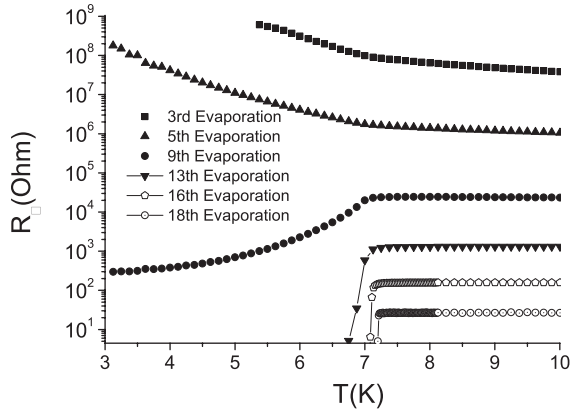

FIG. 3. Resistance per square ($R_\square$) versus temperature for several successive evaporations of Pb on the silicon membrane.

follows variations of the applied power in a quasi-adiabatic way, allowing measurements of the specific heat C_p with a resolution of $\delta C_p/C_p \lesssim 10^{-3}$. The temperature oscillation has a typical amplitude of few mK. This experimental apparatus can detect energy exchanges as small as few femtojoule at the lowest temperature of 1.4 K allowing the measurement of ultra-thin films.

RESULTS AND DISCUSSION

Fig. 3 shows the measurement of the resistance versus temperature of the Pb quench condensed thin films for a few selected evaporation stages. A transition from an insulating to a superconducting state is observed as a function of thickness. The resistive measurement of the first evaporation (few nanometer thick) is not shown; the resistance being greater than GΩ and immeasurable within the given equipment. It is important to notice that a kink is observed in the R(T) measurements close to the superconducting critical temperature of bulk Pb $T_C \sim 7.2$ K.

In Fig. 4, we show the corresponding measurements of heat capacity for the same layers. It is demonstrating that successive measurements of C_p are possible *in situ* allowing the study of the phase transition as a function of thickness. For our granular Pb, careful analysis shows a feature in the $C_p - T$ curve even in the first evaporation (around 8 nm) at $T \sim T_C$. As thickness is increased this feature evolves into a heat capacity jump typical of a second order phase transition. The numerical parameters extracted from the various evaporations shown in the figures are gathered in Table I; the critical temperature is estimated from the heat capacity measurement where an anomaly can be clearly distinguished. The detailed dependence of the specific heat on thickness will be the subject of further studies.

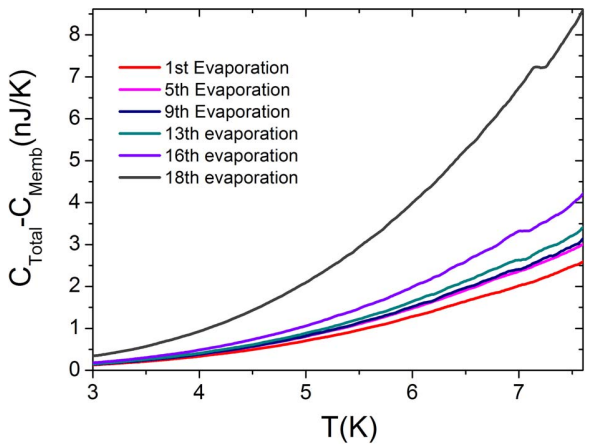

FIG. 4. Heat capacity measurement versus temperature for various successive evaporations of Pb on the silicon membrane. The specific heat jump at the transition appears at $T \sim 7.2$ K for the 18th evaporation.

TABLE I. Data obtained from the sequential evaporation (♯ indicates the evaporation number). C_p (nJ/K) is the heat capacity measured at 7.3 K, T_c is the estimated critical temperature, $R_\square$ (Ω) is the resistance per square of the film, m_{Pb}(μg) is the estimated mass of Pb evaporated, and t(nm) is the estimated Pb thickness.

♯	C_p (nJ/K)	T_c	$R_\square$ (Ω)	m_{Pb} (μg)	t (nm)
1	2.29	6.71	NA	0.42	8.9
5	2.67	6.78	1.5×10^6	0.48	10.3
9	2.85	6.9	4.7×10^4	0.51	10.9
13	3.0	6.95	1383	0.54	11.5
16	3.71	7.05	168	0.66	14.15
18	7.51	7.19	26.7	1.37	29.0

CONCLUSIONS

We have developed an innovative equipment setup that allows the measurement of heat capacity of quench condensed thin films. It can be used for the study of Bi, Sn, In, Pb, or other materials that can be quench-condensed. The main advantage resides in the possibility of performing the C_p and resistance measurements successively by increasing the thickness of the films *in situ* without heating the system. Granular or ultrathin films can be measured using this experiment especially for the study of heat capacity signature of phase transition in very low dimensional superconducting systems.

ACKNOWLEDGMENTS

We thank Pierre Brosse-Maron for his advices and support for the mounting of the equipment, the Pole Capteur Thermométrique et Calorimétrie and Nanofab for the conception of the membrane sensor. We acknowledge fruitful help and discussions with P. Gandit, J. Richard, J.-L. Garden, J.-J. Morales-Chavez, A. F. Lopeandia, and J. Rodriguez-Viejo. The authors acknowledge the financial support from the european project MicroKelvin.

[1]S. L. Sondhi, S. M. Girvin, J. P. Carini, and D. Shahar, Rev. Mod. Phys. **69**, 315 (1997).
[2]A. Larkin and A. Andreevich Varlamov, *Theory of Fluctuations in Superconductors* (Oxford Science Publications, 2007).
[3]J. M. Kosterlitz and D. J. Thouless, J. Phys. C **6**, 1181 (1973).
[4]M. Strongin, R. Thompson, O. Kammerer, and J. Crow, Phys. Rev. B **1**, 1078 (1970).
[5]R. C. Dynes, J. P. Garno, G. B. Hertel, and T. P. Orlando, Phys. Rev. Lett. **53**, 2437 (1984).

[6]R. C. Dynes, A. E. White, J. M. Graybeal, and J. P. Garno, Phys. Rev. Lett. **57**, 2195 (1986).
[7]D. B. Haviland, Y. Liu, and A. M. Goldman, Phys. Rev. Lett. **62**, 2180 (1989).
[8]A. Yazdani and A. Kapitulnik, Phys. Rev. Lett. **74**, 3037 (1995).
[9]A. M. Goldman and N. Markovic, Phys. Today **51**(11), 39 (1998).
[10]M. A. Paalanen, A. F. Hebard, and R. R. Ruel, Phys. Rev. Lett. **69**, 1604 (1992).
[11]V. F. Gantmakher, M. V. Golubkov, V. T. Dolgopolov, G. E. Tsydynzhapov, and A. Shashkin, JETP Lett. **68**, 363 (1998).
[12]N. Hadacek, M. Sanquer, and J. C. Villegier, Phys. Rev. B **69**, 024505 (2004).
[13]G. Sambandamurthy, L. W. Engel, A. Johansson, and D. Shahar, Phys. Rev. Lett. **92**, 107005 (2004); G. Sambandamurthy, L. W. Engel, A. Johansson, E. Peled, and D. Shahar, *ibid.* **94**, 017003 (2005).
[14]M. Steiner and A. Kapitulnik, Physica C **422**, 16 (2005).
[15]T. I. Baturina, J. Bentner, C. Strunk, M. R. Baklanov, and A. Satta, Physica B **359–361**, 500 (2005); T. I. Baturina, C. Strunk, M. R. Baklanov, and A. Satta, Phys. Rev. Lett. **98**, 127003 (2007).
[16]O. Bourgeois, A. Frydman, and R. C. Dynes, Phys. Rev. Lett. **88**, 186403 (2002).
[17]J. M. Valles, Jr., R. C. Dynes, and J. P. Garno, Phys. Rev. Lett. **69**, 3567 (1992).
[18]B. Sacepe, C. Chapelier, T. I. Baturina, V. M. Vinokur, M. R. Baklanov, and M. Sanquer, Phys. Rev. Lett. **101**, 157006 (2008).
[19]B. Sacepe, T. Dubouchet, C. Chapelier, M. Sanquer, M. Ovadia, D. Shahar, M. Feigel'man, and L. Ioffe, Nat. Phys. **7**, 239 (2011).
[20]M. Mondal, A. Kamlapure, M. Chand, G. Saraswat, S. Kumar, J. Jesudasan, L. Benfatto, V. Tripathi, and P. Raychaudhuri, Phys. Rev. Lett. **106**, 047001 (2011).
[21]D. Sherman, G. Kopnov, D. Shahar, and A. Frydman, Phys. Rev. Lett. **108**, 177006 (2012).
[22]W. Liu, M. Kim, G. Sambandamurthy, and N. P. Armitage, Phys. Rev. B **84**, 024511 (2011).
[23]M. Mondal, A. Kamlapure, S. C. Ganguli, J. Jesudasan, V. Bagwe, L. Benfatto, and P. Raychaudhuri, Sci. Rep. **3**, 1357 (2013).
[24]D. Sherman, B. Gorshunov, S. Poran, N. trivedi, E. Farber, M. Dressel, and A. Frydman, Phys. Rev. B **89**, 035149 (2014).
[25]O. Bourgeois, S. E. Skipetrov, F. Ong, and J. Chaussy, Phys. Rev. Lett. **94**, 057007 (2005).
[26]F. R. Ong and O. Bourgeois, Europhys. Lett. **79**, 67003 (2007).
[27]J. S. Urbach, W. R. White, M. R. Beasley, and A. Kapitulnik, Phys. Rev. Lett. **69**, 2407 (1992).
[28]G. D. Zally and J. M. Mochel, Phys. Rev. Lett. **27**, 1710 (1971).
[29]T. Worthington, P. Lindenfeld, and G. Deutscher, Phys. Rev. Lett. **41**, 316 (1978).
[30]D. W. Denlinger, E. N. Abarra, K. Allen, P. W. Rooney, M. T. Messer, S. K. Watson, and F. Hellman, Rev. Sci. Instrum. **65**, 946 (1994).
[31]F. Fominaya, T. Fournier, P. Gandit, and J. Chaussy, Rev. Sci. Instrum. **68**, 4191 (1997).
[32]B. L. Zink, B. Revaz, R. Sappey, and F. Hellman, Rev. Sci. Instrum. **73**, 1841 (2002).
[33]J.-L. Garden, H. Guillou, A. F. Lopeandia, J. Richard, J.-S. Heron, G. M. Souche, F. R. Ong, B. Vianay, and O. Bourgeois, Thermochim. Acta **492**, 16 (2009).
[34]O. Bourgeois, E. André, C. Macovei, and J. Chaussy, Rev. Sci. Instrum. **77**, 126108 (2006).
[35]J. P. Garno, Rev. Sci. Instrum. **49**, 1218 (1978).
[36]O. Bourgeois and R. C. Dynes, Phys. Rev. B **65**, 144503 (2002).
[37]F. Sullivan and G. Seidel, Phys. Rev. **173**, 679 (1968).

זה, במה שנקרא "גרנולריות מושרה". בעזרת שימוש במדידות מגנטיות מקומיות אנו יכולים למדוד שאריות של מוליכות-על בטמפרטורות הגבוהות עד פי 2 מהטמפרטורה הקריטית אשר נמדדת בניסויי תובלה. עדות זו מצטרפת לניסויים אשר בוצעו בעבר אשר רמזו על קיומה של מוליכות-על מעל הטמפרטורה הקריטית.

התוצאות שלנו תומכות בהיפותזה לפיה הסימנים למוליכות-על מעל הטמפרטורה הקריטית נובעים מאי-ההומוגניות של מוליכות העל, והעובדה שחלקים מהחומר מוליך-על למרות העדר מוליכות-על גלובלית.

בנוסף אנו יכולים לחקור את המבנה של הגרנולריות המושרית. אנחנו מראים כי עומק החדירה של מוליך-העל גבוה מאוד ברוב הדגם, משמע מוליכות-העל חלשה. עם זאת, באזורים מסוימים של הדגם עומק החדירה קטן משמעותית. עובדה זו מראה בבירור את אי-הומוגניות של מוליכות העל בדגם.

נוסף על זאת, התוצאות שלנו מצביעות על הדדיות בין לוקליזצית אלקטרונים והגרנולריות המושרית. אנו מראים כי מוליכות העל מתקיימת באזורים בהם ריכוז האלקטרונים גבוה, בעקבות לוקליזצית אנדרסון.

הניסוי המדווח השלישי מבוסס על אפקט הקרבה, אשר מבוצע כגירסא חדשה של מדידות תובלה. אנו מוסיפים שכבה מתכתית דקה על אינדיום אוקסיד אמורפי. אנחנו מוצאים כי השכבה המתכתית יכולה להעלות את הטמפרטורה הקריטית של המערכת מוליכת-העל בעזרת אפקט הקרבה, או להוריד אותה בעזרת אפקט הקרבה ההפוך. ההפרדה בין שני המקרים היא לפי אי-הסדר של המערכת לפני הוספת הזהב.

בנוסף אנו מראים שני מקרים של שכבות מבודדות. מבודדים בעלי אי-סדר גבוה אדישים להוספת השכבה המתכתית. מבודד אשר נמצא קרוב למעבר – ניתן לדחוף אותו למצב המוליך-על.

את אוסף האפקטים הללו אנו מסבירים בעזרת אפקט הקרבה ואפקט הקרבה ההפוך, והאופן בו שניהם משפיעים על מוליכות-העל בשל מוליך-על אשר מפגין גרנולריות חשמלית.

למרות העובדה כי מוליכי-על לא-מסודרים נחקרו רבות במסגרת פיזיקת המצב המוצק מזה מספר עשורים, אנו עדיין רחוקים מלהבין אותם בשלמותם. אנו מאמינים כי עבודה זו תאפשר לנו לקחת צעד אחד קדימה אל תאוריה כוללת שתסביר את המכניזמים אשר עובדים במערכות אלו, ולהעמיק את הבנתנו במוליכי-על בכלל.

תקציר

"איך אי-סדר משפיע על מוליכות-על" היא שאלה אשר מתמידה בפיזיקת המצב המוצק מזה עשרות שנים. למרות עולם עשיר של תיאוריות וניסויים מעשיים, תשובה החלטית עדיין לא נמצאה.

הוכח בעבר באמצעות מגוון ניסויים שהשריית אי-סדר גבוה מספיק על מערכת מוליכת-על, מוליכות-העל פוסקת מלהיות והמערכת הלא-מסודרת הופכת למבודד חשמלי. השינוי הזה ממוליך-על למבודד ממוקם הוא סימן למעבר פאזה קוואנטי, מעבר המתרחש בטמפרטורה אפס בין שני מצבי יסוד קוואנטים, אשר נשלט בידי פרמטר שאינו תרמי. בעצם היותו מעבר פאזה קוואנטי, המעבר בין מוליך-על למבודד מושך תשומת לב רבה בפיזיקת המצב המוצק.

דיסרטציה זו מכוונת לחקירת העולם של מוליכי-על לא מסודרים והמעבר ממוליך-על למבודד במספר שיטות ייחודיות. אנו מקווים להוסיף מידע מכריע שיוביל לפיתוח תיאוריה שלמה אשר תסביר את מהותם של מוליכי-העל הלא-מסודרים.

השיטה השכיחה ביותר לאפיון מוליכי-על לא-מסודרים בניסויים עד כה היא בניסויי תובלה. שיטה זאת רגישה לחוסר-ההומוגניות הייחודי לכל דגם ולמסלולי פרקולציה דרכו. למעשה ניסוי כזה עשוי להתעלם מרוב הדגם, אם רשת הפרקולציה היא דלילה. על-מנת להתגבר על מגבלה זו, שתיים משלוש השיטות שאנחנו מציעים בעבודה זו אינן רגישות כלל לשיקולי פרקולציה.

הניסוי הראשון אותו אנו מבצעים מתגבר על הבעיה בזאת שהוא מודד גודל גלובלי: קיבול החום. אנו מבצעים מדידה תרמו-דינמית זו על שכבות גרנולריות דקות של עופרת ובדיל, שתיהן מערכות אשר עוברות את המעבר ממוליך-על למבודד. מהתוצאות שלנו אנו מסיקים כי אפילו בשלב הלא-מסודר ביותר, כאשר התנגדות הדגם בלתי-מדידה וגבוהה ממספר מיליארדי אוהם, מוליכות-על קיימת בדגם. זוהי הפעם הראשונה בה אישור ריגורוזי שכזה למוליכות-על במבודד נראה, ומישבת את הדיון לגבי אופיו של המבודד הגרנולרי – האם הוא מורכב מזוגות קופר או מאלקטרונים ממוקמים.

בנוסף, הקפיצה בחום הסגולי אשר מכמתת את מעבר-הפאזה מסדר-שני מהמצב הנורמלי למצב המוליך-על, מציגה שיא בעובי הקריטי. אנחנו מראים כי זאת בעקבות הקרבה למעבר הפאזה הקוואנטי. אנחנו מחשבים את הערך של האקספוננט הקריטי של קיבול החום כפונקציה של מרחק ממעבר הפאזה.

ניסוי זה הוא ראשון מסוגו, עם מערכת ניסוי אשר מאפשרת למדוד קיבול חום של דגמים בעלי מאסה נמוכה ביותר. קיבול החום מעולם לא נמדד במערכת שעוברת את המעבר ממוליך-על למבודד, ואנו מאמינים כי התוצאות אותן אנו מספקים הכרחיות להבנת המעבר הנ"ל ומעברים קוואנטים אחרים.

ניסוי נוסף עליו אנו מדווחים בעבודה זו הוא מדידות מגנטיות מקומיות, אשר מבוצעות על-ידי מיקרוסקופית כוח מגנטי. אנו מבצעים את הניסוי על שכבות אמורפיות של אינדיום אוקסיד. שכבות אלו מיוצרות כשכבות אחידות, אך מספר אינדיקציות נראו בעבר לכך שמוליכות העל שבורה לאיים בחומר

עבודה זו בוצעה תחת הנחייתו של

פרופסור אביעד פרידמן

המחלקה לפיזיקה, אוניברסיטת בר אילן

גרנולריות ומוליכי על לא מסודרים

חיבור לשם קבלת התואר "דוקטור לפילוסופיה"

מאת:

שחף פורן

המחלקה לפיזיקה

הוגש לסנט של אוניברסיטת בר-אילן

רמת גן אדר תשע"ה